August 2022

Nonreciprocal Surface Waves on Gyrotropic Interfaces

Alexander Martin Holmes
University of Wisconsin-Milwaukee

NONRECIPROCAL SURFACE WAVES ON GYROTROPIC INTERFACES

by

Alexander M. Holmes

A Dissertation Submitted in

Partial Fulfillment of the

Requirements for the Degree of

Doctor of Philosophy

in Engineering

at

The University of Wisconsin-Milwaukee

August 2022

ABSTRACT

NONRECIPROCAL SURFACE WAVES ON GYROTROPIC INTERFACES

by

Alexander M. Holmes

The University of Wisconsin-Milwaukee, 2022
Under the Supervision of Professor George W. Hanson

In this dissertation, the properties of highly nonreciprocal (unidirectional) surface waves guided along the interface between free-space and various 2D and 3D gyrotropic continua are investigated using analytic, numerical, and experimental methods. From a classical electromagnetics perspective, nonreciprocity in the dispersion of surface wave modes supported by the interface is achieved by breaking both time-reversal and space-inversion symmetries in the collective response of the waveguide, which consists of the two interfaced materials. More recently, however, a connection to momentum space topology via the bulk-edge correspondence principle has been made for gyrotropic continua, providing additional insights into the underlying physics that governs the unique propagation characteristics of these unidirectional modes. Building on the previous work done in the areas of nonreciprocal electromagnetics and topological photonics, we (1) develop a new analytic formalism to model excitations of the surface wave modes using a near field current source, (2) investigate a nontraditional way of achieving a gyrotropic response in a 2D continuum, and (3) demonstrate experimentally, for the first time, the unidirectional nature of a recently theorized topologically protected, unidirectional surface wave mode.

To my wife, Jessica, for all her love and support throughout this endeavor.

TABLE OF CONTENTS

LIST OF FIGURES

Chapter 1

Introduction

1.1 Motivation and background

At the interface between two media, it may be possible to couple electromagnetic radiation from a near field source into the natural surface wave modes supported by the structure. For this to occur, certain conditions on the material response of each medium must be met in order for the mode to exist. For example, in the case where the source medium is an electrical insulator (i.e., a dielectric such as air), the interfaced medium must sufficiently screen the radiation (i.e., the skin depth of the interfaced medium must be sufficiently small) produced by the source in order for the structure to support a well confined surface wave mode, which is ideal in most cases. Electrical conductors such as solid state plasmas, including metals and semi-conductors with high doping levels, typically screen electromagnetic radiation sufficiently at infrared frequencies and below, where intra-band transitions that occur continuously in the conduction band dominate the response at a microscopic level. A screening of the radiation occurs as a result of the electric field produced by the source canceling with the re-radiated electric field of the electron as it transitions from a state of higher energy to one of lower energy in the conduction band. Surface waves that are guided at a dielectric-plasma interface are referred to as surface plasmon polaritons (SPPs) because such a surface wave involves both the oscillation of electronic charge in the plasma (surface plasmon) and the electromagnetic field in the dielectric (polariton) [1, 2].

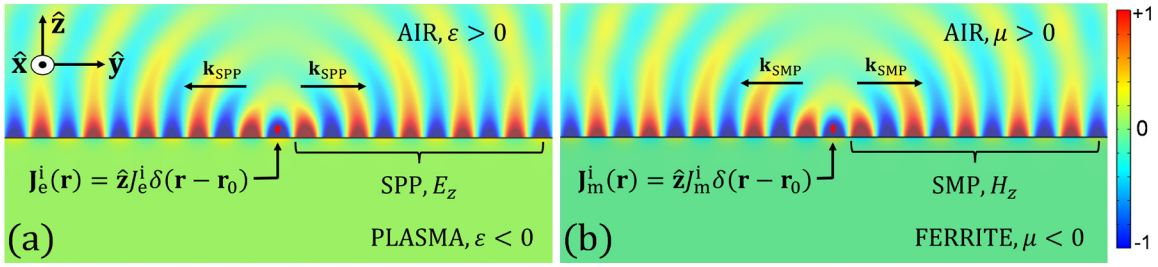

Figure 1-1: A qualitative look at the normalized field profile in the y-z plane of (a) a reciprocal (bidirectional) SPP excited by a localized impressed near-field electric current density $\mathbf{J}_{\mathrm{e}}^{\mathrm{i}}(\mathbf{r}) = \hat{\mathbf{z}} J_{\mathrm{e}}^{\mathrm{i}} \delta(\mathbf{r} - \mathbf{r}_0)$ and (b) a bidirectional SMP excited by a localized near-field magnetic current density $\mathbf{J}_{\mathrm{m}}^{\mathrm{i}}(\mathbf{r}) = \hat{\mathbf{z}} J_{\mathrm{m}}^{\mathrm{i}} \delta(\mathbf{r} - \mathbf{r}_0)$, where $J_{\mathrm{e,m}}^{\mathrm{i}}$ are amplitude coefficients and $\delta(\mathbf{r} - \mathbf{r}_0)$ denotes the Dirac-delta distribution function. In both cases, the source resides in the air region, as indicated by the solid red circles, where the permittivity $\varepsilon > 0$ and permeability $\mu > 0$ support the propagation of bulk radiation emitted by the source. Near the interface, bulk radiation couples into the bidirectional SPP and SMP modes supported by the structure that propagate outward, away from the source, with wavevector $\mathbf{k}_{\mathrm{SPP}}$ and $\mathbf{k}_{\mathrm{SMP}}$ respectively. The normal component of the surface wave fields (i.e., E_z and H_z in the case of SPPs and SMPs respectively) are evanescent with respect to z and propagate parallel to the interface, in the x-y plane. In each case, the field generally attenuates much faster into the interfaced medium (i.e., on this side of the interface, the surface wave is more tightly confined to the interface).

Similarly, surface magnon polaritons (SMPs) are another form of surface wave that arise from the coupling of EM radiation to the magnetic dipole polarization of antiferro- and ferri-magnetic insulators [3]. SMPs are analogous to SPPs in the sense that they represent an oscillation of the magnetic component of the materials re-radiated EM field rather than its electric component. Both SPPs and SMPs offer the ability to concentrate electromagnetic energy into small volumes, below that of a photon in free space [1, 3–7], effectively breaking the diffraction limit, which makes them ideal to achieve low-loss confinement of electromagnetic energy.

At a macroscopic level, the effective permittivity/permeability experienced by a well confined SPP/SMP along the direction of propagation must be negative [8]. To achieve this, the total associated electric/magnetic susceptibility (accounting for polarization and conduction), contained within the permittivity/permeability of the interfaced medium must be inductive/capacitive. As a result, confined SPPs/SMPs have a dominant transverse-magnetic/electric component in nature, where transverse is defined with respect to the propagation direction. That is, the magnetic/electric polarization of SPPs/SMPs is transverse (i.e., perpendicular) to the propagation direction and interface normal, while the

electric/magnetic polarization generally has a component normal to the interface and along the propagation direction. For isotropic materials, well confined SPPs/SMPs are purely transverse-magnetic/electric, however, for anisotropic materials, the SPPs/SMPs are hybrid, and commonly characterized as quasi-transverse-magnetic/electric, since they still generally contain a dominant transverse-magnetic/electric polarization component. In addition, it should be noted that the majority of electromagnetic energy stored in a transverse-magnetic/electric surface wave resides in the electric/magnetic field [3, 9–11].

Figure 1-1 gives a qualitative look at field pattern of (a) a reciprocal (bidirectional in the y-z plane) SPP and (b) a bidirectional SMP field profile (normal, $\hat{\mathbf{z}}$ component), confined to the interface between air and (a) a plasma characterized by an effective negative permittivity and (b) a ferrite characterized by an effective negative permeability experienced by the surface wave along the direction of propagation (i.e., $\pm\hat{\mathbf{y}}$). Being confined to the interface, the electric/magnetic field attenuates away from the interface on each side. In the case of SPPs, the wave is excited by a localized near field electric current density modeled by $\mathbf{J}_e^i = \hat{\mathbf{z}} J_e^i \delta(\mathbf{r} - \mathbf{r}_0)$, while in the case of SMPs, an effective magnetic current density modeled by $\mathbf{J}_m^i = \hat{\mathbf{z}} J_m^i \delta(\mathbf{r} - \mathbf{r}_0)$ may be considered; parameters J_e^i and J_m^i are arbitrary source amplitudes having units of $[\mathrm{A} \cdot \mathrm{m}]$ and $[\mathrm{V} \cdot \mathrm{m}]$ respectively, $\mathbf{r}$ is a general spatial coordinate, $\mathbf{r}_0$ is the source coordinate, and $\delta(\mathbf{r} - \mathbf{r}_0)$ is the Dirac delta distribution function having units of $\left[\mathrm{m}^{-3}\right]$. In both cases, the source is polarized along the interface normal $\hat{\mathbf{z}}$ in order to match the dominant radiated electric/magnetic field polarization with that of the (quasi-) transverse-magnetic/electric SPP/SMP mode into which the radiation couples. Both SPPs and SMPs propagate bidirectionally away from the source (on both sides) with wavevector $\mathbf{k}_{\mathrm{SPP}}$ and $\mathbf{k}_{\mathrm{SMP}}$ respectively.

When the interfaced medium is also anisotropic, the surface wave modes generally depend on both the magnitude and direction of their momentum, in addition to the operating frequency of the source. In the following, we consider the scenario in which an isotropic dielectric (e.g., air) containing the source, is interfaced with a variety of 2D and 3D gyrotropic media, a subclass of anisotropic media having broken time-reversal (TR) symmetry in their

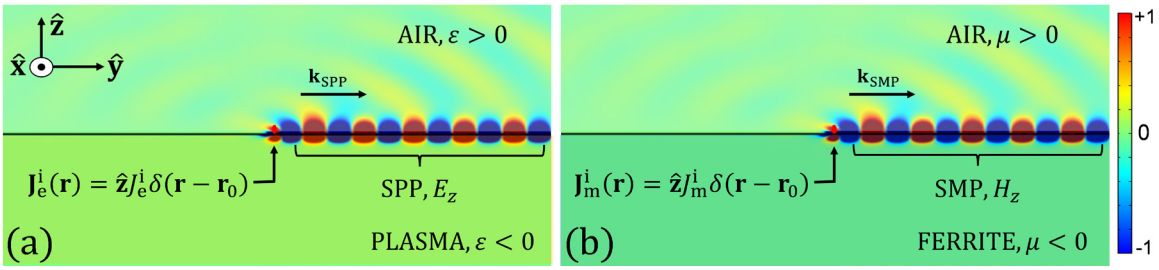

Figure 1-2: A qualitative look at the normalized field profile in the y-z plane of (a) a highly nonreciprocal (unidirectional) SPP excited by a localized impressed near-field electric current density $\mathbf{J}_{\mathrm{e}}^{\mathrm{i}}(\mathbf{r}) = \hat{\mathbf{z}} J_{\mathrm{e}}^{\mathrm{i}} \delta(\mathbf{r} - \mathbf{r}_0)$ and (b) a unidirectional SMP excited by a localized near-field magnetic current density $\mathbf{J}_{\mathrm{m}}^{\mathrm{i}}(\mathbf{r}) = \hat{\mathbf{z}} J_{\mathrm{m}}^{\mathrm{i}} \delta(\mathbf{r} - \mathbf{r}_0)$, where $J_{\mathrm{e,m}}^{\mathrm{i}}$ are amplitude coefficients and $\delta(\mathbf{r} - \mathbf{r}_0)$ denotes the Dirac-delta distribution function. In both cases, the source resides in the air region, as indicated by the solid red circles, where the permittivity $\varepsilon > 0$ and permeability $\mu > 0$ support the propagation of bulk radiation emitted by the source. Near the interface, bulk radiation couples into the unidirectional bulk radiation couples into the bidirectional SPP and SMP modes supported by the structure that propagate outward, away from the source, with wavevector $\mathbf{k}_{\mathrm{SPP}}$ and $\mathbf{k}_{\mathrm{SMP}}$ respectively. The normal component of the surface wave fields (i.e., E_z and H_z in the case of SPPs and SMPs respectively) are evanescent with respect to z and propagate parallel to the interface, in the x-y plane. In each case, the field generally attenuates much faster into the interfaced medium (i.e., on this side of the interface, the surface wave is more tightly confined to the interface).

material response. Interestingly, it has long been theorized and experimentally verified in many cases that unidirectional surface wave modes may be realized when space-inversion symmetry is also broken in the system by introducing the interface (or edge) in a plane parallel to the axis along which TR symmetry is broken [12]. These unidirectional surface wave modes propagate in the topologically nontrivial bulk bandgap of the interfaced medium, and, as a result are immune to diffraction into the bulk. However, diffraction into the dielectric region is still possible if it lacks a common bulk bandgap (e.g., air). In addition, the unidirectional nature of the surface wave modes grants them immunity to back-scattering since there exists no backward mode for the radiation to couple into. As such, they are forced to propagate over discontinuities that arise in the material interface, which makes them promising for nonreciprocal device applications [13–22].

Figure 1-2 gives a qualitative look at the normalized field pattern of (a) a highly nonreciprocal (unidirectional) SPP and (b) a unidirectional SMP (normal, $\hat{\mathbf{z}}$ component), confined to the interface between air and (a) a gyrotropic plasma characterized by an effective negative permittivity and (b) a ferrite characterized by an effective negative permeability experienced by the surface wave along the propagation direction (i.e., $+\hat{\mathbf{y}}$). Both SPPs

and SMPs behave similar to the bidirectional case in Fig. 1-1, however, only propagate in one direction (i.e., unidirectionally) away from the source with wavevector $\mathbf{k}_{\mathrm{SPP}}$ and $\mathbf{k}_{\mathrm{SMP}}$ respectively.

Acquiring a reliable model for the material response of the interfaced medium is crucial to the study and prediction of surface wave properties including confinement, propagation length, and wavelength. Here, we employ both well studied and new models for the response, derived from classical, semi-classical and non-classical (microscopic/quantum) physics. Once the material response is obtained, the wave equation, derived from Maxwell's equations, governing the propagation of electromagnetic radiation are solved in the absence of sources on either side of the interface to obtain the dispersion and general field profile of bulk modes that propagate freely in each medium. Applying the appropriate boundary and radiation conditions on the bulk mode fields at the interface and infinity, the dispersion relation for the surface wave modes is recovered which may be solved for the momentum and frequency associated with each mode. In addition, application of the boundary conditions at the interface lead to the recovery of the reflection and transmission tensor coefficients used in the Green's function to define the scattered field profile of the surface wave.

Our motivation for the research presented in this dissertation is two-fold. First, we continue to study the interesting topological and unidirectional properties of surface waves on three-dimensional (3D) gyrotropic continua such as plasmas and microwave ferrites biased with an external, static magnetic field. Application of the external magnetic field is what breaks TR symmetry in these materials, and has been the traditional way of achieving a gyrotropic response. However, a recent demand for achieving the same gyrotropic response without an external field has motivated the second portion of the research presented in this dissertation, which we organize as follows. In Chap. 2, the unique properties of unidirectional SPPs supported by the interface between air and a gyrotropic plasma, are investigated [23]. In Chap. 3, the properties of reciprocal bulk and nonreciprocal edge SPPs on a variety of atomically thin gyrotropic plasmas embedded in air are investigated, and a nontraditional way of breaking TR symmetry (i.e., without an external magnetic bias

field) in the material response of new 2D heterostructure is proposed [24, 25]. In Chap. 4, unidirectional SMP modes supported by the interface between air and a gyrotropic YIG ferrite are studied theoretically, and the topological nature of the modes is reviewed and demonstrated experimentally for the first time [26]. To set the stage for Chaps. 2-4, the remainder of this chapter is dedicated to a review of the time-harmonic Maxwell's equations, the wave equation, and other fundamental topics in electromagnetics that are relevant to our discussion.

1.2 Maxwell's equations

In the linear response approximation (LRA) [27], a time harmonic impressed current source, operating at frequency f, maintains time harmonic response currents and fields. Assuming the time harmonic convention $\exp(+j\omega t)$, Maxwell's equations governing the relationship between the source current and response in the phasor domain (i.e., the partial time derivatives ∂_t simply become $+j\omega$ where $\omega = 2\pi f$ is the radial frequency and j denotes the imaginary unit) are given generally by

$$\nabla \times \mathbf{H}(\mathbf{r},\omega) = j\omega\varepsilon_0 \mathbf{E}(\mathbf{r},\omega) + \mathbf{J}_e(\mathbf{r},\omega) \ , \tag{1.1}$$

$$\nabla \times \mathbf{E}(\mathbf{r},\omega) = -j\omega\mu_0 \mathbf{H}(\mathbf{r},\omega) - \mathbf{J}_m(\mathbf{r},\omega) \ , \tag{1.2}$$

where $\mathbf{E}$ and $\mathbf{H}$ are the electric and magnetic phasor fields, and

$$\mathbf{J}_\nu = \sum_{\upsilon\in\{i,p,c\}} \mathbf{J}_\nu^\upsilon \ : \ \nu \in \{e,m\} \tag{1.3}$$

is the total electric ($\nu \equiv e$) and magnetic ($\nu \equiv m$) current densities that contain the impressed ($\upsilon \equiv i$) and response current densities due to polarization ($\upsilon \equiv p$) and conduction ($\upsilon \equiv c$); parameters ε_0 and μ_0 denote the permittivity and permeability of freespace. Each current density $\mathbf{J}_\nu^\upsilon$ is related to the corresponding charge density ϱ_ν^υ via the continuity

equation

$$\nabla \cdot \mathbf{J}_\nu^v + j\omega \varrho_\nu^v = 0 \ . \tag{1.4}$$

The differential operators $\nabla\cdot$ and $\nabla\times$ denote the divergence and curl differential operators.

1.2.1 Material response tensors

In the linear response approximation, the response currents are proportional to the fields

$$\mathbf{J}_e^p = j\omega \left(\bar{\chi}_{ee} \cdot \varepsilon_0 \mathbf{E} + \bar{\chi}_{em} \cdot \mathbf{H} \right) \ , \tag{1.5}$$

$$\mathbf{J}_m^p = j\omega \left(\bar{\chi}_{mm} \cdot \mu_0 \mathbf{H} + \bar{\chi}_{me} \cdot \mathbf{E} \right) \ , \tag{1.6}$$

$$\mathbf{J}_e^c = \bar{\sigma}_{ee} \cdot \mathbf{E} + \bar{\sigma}_{em} \cdot \mathbf{H} \ , \tag{1.7}$$

$$\mathbf{J}_m^c = \bar{\sigma}_{mm} \cdot \mathbf{H} + \bar{\sigma}_{me} \cdot \mathbf{E} \ , \tag{1.8}$$

where $\bar{\chi}_{\nu\nu'}$ and $\bar{\sigma}_{\nu\nu'}$ for $\nu, \nu' \in \{e, m\}$ are susceptibility and conductivity tensors that couple the electric and magnetic fields to the response currents. Often, it is convenient to define the auxiliary fields (i.e., the electric displacement $\mathbf{D}$ and the magnetic flux density $\mathbf{B}$)

$$\mathbf{D} = \bar{\varepsilon} \cdot \varepsilon_0 \mathbf{E} + \bar{\xi} \cdot \mathbf{H} \ , \tag{1.9}$$

$$\mathbf{B} = \bar{\mu} \cdot \mu_0 \mathbf{H} + \bar{\zeta} \cdot \mathbf{E} \ , \tag{1.10}$$

where

$$\bar{\varepsilon} = \bar{\mathbf{I}} + \bar{\chi}_{ee} - j\omega^{-1} \varepsilon_0^{-1} \bar{\sigma}_{ee} \ , \tag{1.11}$$

$$\bar{\mu} = \bar{\mathbf{I}} + \bar{\chi}_{mm} - j\omega^{-1} \mu_0^{-1} \bar{\sigma}_{mm} \ , \tag{1.12}$$

$$\bar{\xi} = \bar{\chi}_{em} - j\omega^{-1} \bar{\sigma}_{em} \ , \tag{1.13}$$

$$\bar{\zeta} = \bar{\chi}_{me} - j\omega^{-1} \bar{\sigma}_{me} \ , \tag{1.14}$$

are the relative permittivity $\bar{\varepsilon}$ and relative permeability $\bar{\mu}$, and magneto-electric coupling tensors $\bar{\xi}$ and $\bar{\zeta}$.

1.2.2 Reciprocity

A medium is reciprocal if the material response tensors $\{\bar{\varepsilon}, \bar{\mu}, \bar{\xi}, \bar{\zeta}\}$ satisfy

$$\bar{\varepsilon} = \bar{\varepsilon}^{\mathrm{T}} , \tag{1.15}$$

$$\bar{\mu} = \bar{\mu}^{\mathrm{T}} , \tag{1.16}$$

$$\bar{\xi} = -\bar{\zeta}^{\mathrm{T}} . \tag{1.17}$$

where $(\cdot)^{\mathrm{T}}$ indicates transpose. Consequently, isotropic media and anisotropic media with symmetric permittivity and permeability tensors are reciprocal. Examples of nonreciprocal media include gyrotropic plasmas and ferrites since they possesses permittivity and permeability tensors respectively that violate Eqs. (1.15)-(1.16).

1.2.3 Duality

In terms of the auxiliary fields $\mathbf{D}$ and $\mathbf{B}$, Maxwell's equations (1.1)-(1.2) become

$$\nabla \times \mathbf{H} = j\omega\mathbf{D} + \mathbf{J}_e^i , \tag{1.18}$$

$$\nabla \times \mathbf{E} = -j\omega\mathbf{B} - \mathbf{J}_m^i . \tag{1.19}$$

where it should be stressed that $\mathbf{J}_m^i$ is a fictitious (non physical) impressed magnetic current density due to the in-existence of magnetic monopoles in nature. The justification for adding this term to Maxwell's equations is two fold. First, a small current loop may be characterized by its magnetic dipole moment, oriented perpendicular to the plane of the loop. The associated fields of the current loop can be solved in exactly the same manner as in the electric dipole case by replacing the electric current density of the loop $\mathbf{J}_e^i$ with an equivalent magnetic dipole current $\mathbf{J}_m^i$. Second, when Eqs. (1.18)-(1.19) are applied to a finite region of space, the bounding surfaces of the region can be viewed as supporting surface electric currents due to discontinuities in the tangential magnetic field in the same way that they support surface magnetic currents due to discontinuities in the tangential

electric field.

By adding $\mathbf{J}_m^i$ to the right side of Eq. (1.19), Maxwell's equations become duals of each other. That is, if we make the replacements

$$\begin{aligned}&\left\{\mathbf{E},\mathbf{H},\mathbf{D},\mathbf{B},\bar{\varepsilon},\bar{\mu},\bar{\xi},\bar{\zeta},\varrho_e,\varrho_m,\mathbf{J}_e,\mathbf{J}_m\right\}\\&\rightarrow\left\{\mathbf{H},-\mathbf{E},\mathbf{B},-\mathbf{D},\bar{\mu},\bar{\varepsilon},-\bar{\zeta},-\bar{\xi},\varrho_m,-\varrho_e,\mathbf{J}_m,-\mathbf{J}_e\right\}\ .\end{aligned}\tag{1.20}$$

then Eq. (1.18) becomes Eq. (1.19) and vice versa. It should also be noted at these replacements are not unique. This is known as the Duality principle in electromagnetics. Electromagnetic duality is relevant to our discussion because it explains the similarity between SPPs and SMPs. That is, once a model is established for the near-field excitation of SPPs via an electric current density, the same model can be used for SMPs by making the above replacements.

1.3 The wave equation

The wave equations for $\mathbf{E}$ and $\mathbf{H}$ are obtained from Eqs. (1.9)-(1.10) by introducing a new dyadic differential operator $\bar{\nabla}=\nabla\times\bar{\mathbf{I}}$, which when dotted with a vector field $\mathbf{V}$ gives the curl (i.e., $\bar{\nabla}\cdot\mathbf{V}=\nabla\times\bar{\mathbf{I}}\cdot\mathbf{V}=\nabla\times\mathbf{V}$ where $\bar{\mathbf{I}}$ denotes the unit dyadic). With this notation, Maxwell's equations simplify to

$$\left(\bar{\nabla}-j\omega\bar{\xi}\right)\cdot\mathbf{H}=j\omega\varepsilon_0\bar{\varepsilon}\cdot\mathbf{E}+\mathbf{J}_e^i\ ,\tag{1.21}$$

$$\left(\bar{\nabla}+j\omega\bar{\zeta}\right)\cdot\mathbf{E}=-j\omega\mu_0\bar{\mu}\cdot\mathbf{H}-\mathbf{J}_m^i\ .\tag{1.22}$$

from which we obtain

$$j\omega\varepsilon_0\mathbf{E}=\bar{\varepsilon}^{-1}\cdot\left(\bar{\nabla}-j\omega\bar{\xi}\right)\cdot\mathbf{H}-\bar{\varepsilon}^{-1}\cdot\mathbf{J}_e^i\ ,\tag{1.23}$$

$$j\omega\mu_0\mathbf{H}=-\bar{\mu}^{-1}\cdot\left(\bar{\nabla}+j\omega\bar{\zeta}\right)\cdot\mathbf{E}-\bar{\mu}^{-1}\cdot\mathbf{J}_m^i\ .\tag{1.24}$$

Substituting Eq. (1.24) into Eq. (1.21) and Eq. (1.23) into Eq. (1.22) respectively, the wave equations for general bianisotropic media characterized by the set of material response tensors $\left\{\bar{\varepsilon}, \bar{\mu}, \bar{\xi}, \bar{\zeta}\right\}$ are recovered [cite RC]

$$\left[\left(\bar{\nabla} - j\omega\bar{\xi}\right) \cdot \bar{\mu}^{-1} \cdot \left(\bar{\nabla} + j\omega\bar{\zeta}\right) - k_0^2\bar{\varepsilon}\right] \cdot \mathbf{E} = -\left(\bar{\nabla} - j\omega\bar{\xi}\right) \cdot \bar{\mu}^{-1} \cdot \mathbf{J}_m^i - j\omega\mu_0\mathbf{J}_e^i \ , \tag{1.25}$$

$$\left[\left(\bar{\nabla} + j\omega\bar{\zeta}\right) \cdot \bar{\varepsilon}^{-1} \cdot \left(\bar{\nabla} - j\omega\bar{\xi}\right) - k_0^2\bar{\mu}\right] \cdot \mathbf{H} = \left(\bar{\nabla} + j\omega\bar{\zeta}\right) \cdot \bar{\varepsilon}^{-1} \cdot \mathbf{J}_e^i - j\omega\varepsilon_0\mathbf{J}_m^i \ . \tag{1.26}$$

where $k_0 = \omega\sqrt{\varepsilon_0\mu_0}$ is the freespace wavenumber. However, it should be noted that Eqs. (1.25)-(1.26) remain valid only in the case where the determinant of $\bar{\varepsilon}$ and $\bar{\mu}$ is nonzero.

1.3.1 The wave equation for homogenous anisotropic media

The constitutive relations for anisotropic media are given by Eqs. (1.9)-(1.10) when $\bar{\xi} = \bar{\mathbf{0}}$ and $\bar{\zeta} = \bar{\mathbf{0}}$. Here, we consider the two cases of electrically and magnetically anisotropic media, relevant to our discussion. Electrically anisotropic media are characterized by a nontrivial relative permittivity tensor $\bar{\varepsilon}$ and a scalar relative permeability μ, while magnetically anisotropic media are characterized by an nontrivial relative permeability tensor $\bar{\mu}$ and a scalar relative permittivity ε. For electrically and magnetically anisotropic media, it is mathematically convenient to solve the wave equations that govern the electric and magnetic fields respectively. That is, we solve Eq. (1.25) when studying electrically anisotropic media and Eq. (1.26) when studying magnetically anisotropic media. In these two cases, the wave equations simplify to

$$\bar{\nabla} \cdot \bar{\nabla} \cdot \mathbf{E} - k_0^2\mu\bar{\varepsilon} \cdot \mathbf{E} = -\bar{\nabla} \cdot \mathbf{J}_m^i - j\omega\mu_0\mu\mathbf{J}_e^i \ , \tag{1.27}$$

$$\bar{\nabla} \cdot \bar{\nabla} \cdot \mathbf{H} - k_0^2\bar{\mu} \cdot \mathbf{H} = \bar{\nabla} \cdot \mathbf{J}_e^i - j\omega\varepsilon_0\varepsilon\mathbf{J}_m^i \ . \tag{1.28}$$

or, equivalently, using the vector identity $\bar{\nabla}\cdot\bar{\nabla}\cdot\mathbf{V}=\nabla\times\nabla\times\mathbf{V}=\nabla\nabla\cdot\mathbf{V}-\nabla^2\mathbf{V}$,

$$\left(k_0^2\bar{\varepsilon}+\nabla^2\bar{\mathbf{I}}-\nabla\nabla\right)\cdot\mathbf{E}=\bar{\nabla}\cdot\mathbf{J}_m^i+j\omega\mu_0\mu\mathbf{J}_e^i\ , \tag{1.29}$$

$$\left(k_0^2\bar{\mu}+\nabla^2\bar{\mathbf{I}}-\nabla\nabla\right)\cdot\mathbf{H}=-\bar{\nabla}\cdot\mathbf{J}_e^i+j\omega\varepsilon_0\varepsilon\mathbf{J}_m^i\ . \tag{1.30}$$

1.3.2 The wave equation for homogenous isotropic media

The constitutive relations for homogeneous isotropic media in the absence of spatial dispersion are given by Eqs. (1.9)-(1.10) when $\bar{\xi}=\bar{\mathbf{0}}$, $\bar{\zeta}=\bar{\mathbf{0}}$, $\bar{\varepsilon}=\bar{\mathbf{I}}\varepsilon$ and $\bar{\mu}=\bar{\mathbf{I}}\mu$. In this case, the wave equations simplify to

$$\bar{\nabla}\cdot\bar{\nabla}\cdot\mathbf{E}-k^2\mathbf{E}=-\bar{\nabla}\cdot\mathbf{J}_m^i-j\omega\mu_0\mu\mathbf{J}_e^i\ , \tag{1.31}$$

$$\bar{\nabla}\cdot\bar{\nabla}\cdot\mathbf{H}-k^2\mathbf{H}=\bar{\nabla}\cdot\mathbf{J}_e^i-j\omega\varepsilon_0\varepsilon\mathbf{J}_m^i\ . \tag{1.32}$$

where $k=k_0\sqrt{\mu\varepsilon}$. Using the vector identity $\bar{\nabla}\cdot\bar{\nabla}\cdot\mathbf{V}=\nabla\times\nabla\times\mathbf{V}=\nabla\nabla\cdot\mathbf{V}-\nabla^2\mathbf{V}$, the above relations simplify to

$$\nabla^2\mathbf{E}+k^2\mathbf{E}=\nabla\nabla\cdot\mathbf{E}+j\omega\mu_0\mu\mathbf{J}_e^i+\bar{\nabla}\cdot\mathbf{J}_m^i\ , \tag{1.33}$$

$$\nabla^2\mathbf{H}+k^2\mathbf{H}=\nabla\nabla\cdot\mathbf{H}+j\omega\varepsilon_0\varepsilon\mathbf{J}_m^i-\bar{\nabla}\cdot\mathbf{J}_e^i\ . \tag{1.34}$$

From Eqs. (1.23)-(1.24), we have

$$\nabla\cdot\mathbf{E}=j\omega^{-1}\varepsilon_0^{-1}\varepsilon^{-1}\nabla\cdot\mathbf{J}_e^i\ , \tag{1.35}$$

$$\nabla\cdot\mathbf{H}=j\omega^{-1}\mu_0^{-1}\mu^{-1}\nabla\cdot\mathbf{J}_m^i\ . \tag{1.36}$$

Then,

$$\nabla^2\mathbf{E}+k^2\mathbf{E}=j\omega^{-1}\varepsilon_0^{-1}\varepsilon^{-1}\left(\bar{\mathbf{I}}k^2+\nabla\nabla\right)\cdot\mathbf{J}_e^i+\bar{\nabla}\cdot\mathbf{J}_m^i\ , \tag{1.37}$$

$$\nabla^2\mathbf{H}+k^2\mathbf{H}=j\omega^{-1}\mu_0^{-1}\mu^{-1}\left(\bar{\mathbf{I}}k^2+\nabla\nabla\right)\cdot\mathbf{J}_m^i-\bar{\nabla}\cdot\mathbf{J}_e^i\ , \tag{1.38}$$

which are straightforward to solve using Hertzian vector potentials and Green's functions. In later chapters, to obtain the dispersion of SPP and SMP modes supported by the interface between freespace and electrically (magnetically) gyrotropic media, (1.37) and (1.29) are solved for the electric fields in the regions above and below the interface ((1.38) and (**??**) are solved for the magnetic fields in the regions above and below the interface).

1.3.3 Hertzian vector potentials

To solve Eqs. (1.37)-(1.38), it is convenient to use Hertzian potentials. In the LRA, superposition applies, and therefore, we may consider the electric $\mathbf{E}_\nu$ and magnetic $\mathbf{H}_\nu$ fields maintained by the impressed electric $\mathbf{J}_e^i$ and magnetic $\mathbf{J}_m^i$ current sources individually, and add their contributions in the end. In the absence of magnetic sources (i.e., $\mathbf{J}_m^i \equiv \mathbf{0}$), Eqs. (1.18) and (1.19) reduce to

$$\nabla \times \mathbf{H}_e = j\omega\varepsilon_0\varepsilon\mathbf{E}_e + \mathbf{J}_e^i \ , \tag{1.39}$$

$$\nabla \times \mathbf{E}_e = -j\omega\mu_0\mu\mathbf{H}_e \ . \tag{1.40}$$

By virtue of the vector identity $\nabla \cdot (\nabla \times \mathbf{V}) = 0$, we may then write $\mathbf{H}_e = j\omega\varepsilon_0\varepsilon\,(\nabla \times \mathbf{\Pi}_e)$, where $\mathbf{\Pi}_e$ stands for the electric Hertzian vector potential. Integrating both sides of Eq. (1.40), it follows that $\mathbf{E}_e = k^2\mathbf{\Pi}_e + \nabla\varphi_e$ where φ_e is an arbitrary electric scalar potential. From Eq. (1.39), the wave equation for $\mathbf{\Pi}_e$ is obtained as

$$\left(\nabla^2 + k^2\right)\mathbf{\Pi}_e = \nabla\left(\nabla \cdot \mathbf{\Pi}_e - \varphi_e\right) + j\omega^{-1}\varepsilon_0^{-1}\varepsilon^{-1}\mathbf{J}_e^i \ . \tag{1.41}$$

The vector field $\mathbf{\Pi}_e$ is uniquely defined if its curl and divergence are uniquely defined. In the Lorenz gauge where $\varphi_e \equiv \nabla \cdot \mathbf{\Pi}_e$, Eq. (1.40) simplifies to

$$\left(\nabla^2 + k^2\right)\mathbf{\Pi}_e = j\omega^{-1}\varepsilon_0^{-1}\varepsilon^{-1}\mathbf{J}_e^i \ , \tag{1.42}$$

thus making $\mathbf{\Pi}_\mathrm{e}$ co-linear with $\mathbf{J}_e^i$.

In the absence of electric sources (i.e., $\mathbf{J}_e^i \equiv \mathbf{0}$), Eqs. (1.18) and (1.19) reduce to

$$\nabla \times \mathbf{H}_m = j\omega\varepsilon_0\varepsilon\mathbf{E}_m \ , \tag{1.43}$$

$$\nabla \times \mathbf{E}_m = -j\omega\mu_0\mu\mathbf{H}_m - \mathbf{J}_m^i \ , \tag{1.44}$$

where we define $\mathbf{E}_m = -j\omega\mu_0\mu\left(\nabla \times \mathbf{\Pi}_m\right)$ where $\mathbf{\Pi}_m$ stands for the magnetic Hertzian vector potential. From Eq. (1.43), it follows that $\mathbf{H}_m = k^2\mathbf{\Pi}_m + \nabla\varphi_m$ where φ_m is an arbitrary magnetic scalar potential. In the Lorenz gauge where $\varphi_m \equiv \nabla \cdot \mathbf{\Pi}_m$, the wave equation for $\mathbf{\Pi}_m$ is obtained as

$$\left(\nabla^2 + k^2\right)\mathbf{\Pi}_m = j\omega^{-1}\mu_0^{-1}\mu^{-1}\mathbf{J}_m^i \ . \tag{1.45}$$

Adding the field contributions maintained by electric and magnetic sources, we find

$$\begin{aligned}\mathbf{E} &= \mathbf{E}_e + \mathbf{E}_m \\ &= \left(k^2\bar{\mathbf{I}} + \nabla\nabla\right)\cdot\mathbf{\Pi}_e - j\omega\mu_0\mu\left(\nabla \times \mathbf{\Pi}_m\right) \ , \end{aligned} \tag{1.46}$$

$$\begin{aligned}\mathbf{H} &= \mathbf{H}_m + \mathbf{H}_e \\ &= \left(k^2\bar{\mathbf{I}} + \nabla\nabla\right)\cdot\mathbf{\Pi}_m + j\omega\varepsilon_0\varepsilon\left(\nabla \times \mathbf{\Pi}_e\right) \ , \end{aligned} \tag{1.47}$$

for which the general solution is often expressed as

$$\mathbf{\Pi}_e = -j\omega^{-1}\varepsilon_0^{-1}\varepsilon^{-1}\int_V g_0\left(\mathbf{r},\mathbf{r}'\right)\mathbf{J}_e^i\left(\mathbf{r}'\right)dV' \tag{1.48}$$

$$\mathbf{\Pi}_m = -j\omega^{-1}\mu_0^{-1}\mu^{-1}\int_V g_0\left(\mathbf{r},\mathbf{r}'\right)\mathbf{J}_m^i\left(\mathbf{r}'\right)dV' \tag{1.49}$$

where V is the source volume, and $g_0\left(\mathbf{r},\mathbf{r}'\right) = e^{-jkR}/4\pi R$ with $R = |\mathbf{r}-\mathbf{r}'|$ is the scalar greens function that satisfies

$$\left(\nabla^2 + k^2\right)g_0\left(\mathbf{r},\mathbf{r}'\right) = -\delta\left(\mathbf{r}-\mathbf{r}'\right) \ . \tag{1.50}$$

1.4 Dyadic Green's functions for isotropic media

Now, consider an impressed electric current source $\mathbf{J}_e^i(\mathbf{r})$ in an infinite universe filled with an isotropic, homogenous medium characterized by relative permeability μ and relative permittivity ε. The electric field maintained by such a source $\mathbf{E}_e(\mathbf{r})$ is defined in terms of the scalar greens function $g_0(\mathbf{r},\mathbf{r}')$ according to Eq. (1.48), $\mathbf{E}_e \equiv \mathbf{E}_e^{(1)} + \mathbf{E}_e^{(2)}$, where

$$j\omega\varepsilon_0\varepsilon\mathbf{E}_e^{(1)} = k^2 \int_V g_0\left(\mathbf{r},\mathbf{r}'\right)\mathbf{J}\left(\mathbf{r}'\right)dV' \ , \tag{1.51}$$

$$j\omega\varepsilon_0\varepsilon\mathbf{E}_e^{(2)} = \nabla\nabla\cdot\int_V g_0\left(\mathbf{r},\mathbf{r}'\right)\mathbf{J}\left(\mathbf{r}'\right)dV' \ . \tag{1.52}$$

Expanding the differential operator ∇ in a set of Cartesian basis vectors $\{\hat{\mathbf{x}}_1,\hat{\mathbf{x}}_2,\hat{\mathbf{x}}_3\}$, we have

$$\nabla\nabla = \sum_{i=1}^{3}\frac{\partial}{\partial x_i}\hat{\mathbf{x}}_i\sum_{j=1}^{3}\frac{\partial}{\partial x_j}\hat{\mathbf{x}}_j = \sum_{i,j}\frac{\partial^2}{\partial x_i\partial x_j}\hat{\mathbf{x}}_i\hat{\mathbf{x}}_j \ , \tag{1.53}$$

from which it follows that

$$j\omega\varepsilon_0\varepsilon\mathbf{E}_e^{(2)} = \sum_{i,j}\hat{\mathbf{x}}_i\hat{\mathbf{x}}_j\cdot\frac{\partial^2}{\partial x_i\partial x_j}\int_V g_0\left(\mathbf{r},\mathbf{r}'\right)\mathbf{J}_e^i\left(\mathbf{r}'\right)dV' \ . \tag{1.54}$$

Employing the second derivative formula [28]

$$\begin{aligned}\frac{\partial^2}{\partial x_i\partial x_j}\int_V g_0\left(\mathbf{r},\mathbf{r}'\right)\mathbf{J}_e^i\left(\mathbf{r}'\right)dV' = -\mathbf{J}_e^i(\mathbf{r})\int_S\frac{\partial}{\partial x_i}g_0\left(\mathbf{r},\mathbf{r}'\right)\hat{\mathbf{x}}_j\cdot\hat{\mathbf{n}}dS' \\ + \lim_{\delta\to 0}\int_{V-V_\delta}\left[\mathbf{J}_e^i\left(\mathbf{r}'\right)-\mathbf{J}_e^i(\mathbf{r})\right]\frac{\partial^2}{\partial x_j'\partial x_i'}g_0\left(\mathbf{r},\mathbf{r}'\right)dV' \ ,\end{aligned} \tag{1.55}$$

leads to

$$\begin{aligned}j\omega\varepsilon_0\varepsilon\mathbf{E}_e^{(2)} = -\int_S\nabla g_0\left(\mathbf{r},\mathbf{r}'\right)\mathbf{J}_e^i(\mathbf{r})\cdot\hat{\mathbf{n}}dS' \\ + \lim_{\delta\to 0}\int_{V-V_\delta}\left[\mathbf{J}_e^i\left(\mathbf{r}'\right)-\mathbf{J}_e^i(\mathbf{r})\right]\cdot\nabla'\nabla' g_0\left(\mathbf{r},\mathbf{r}'\right)dV' \ .\end{aligned} \tag{1.56}$$

Noting that $\nabla' g_0(\mathbf{r},\mathbf{r}') = -\nabla g_0(\mathbf{r},\mathbf{r}')$, we obtain

$$\begin{aligned} j\omega\varepsilon_0\varepsilon\mathbf{E}_e^{(2)} &= \lim_{\delta\to 0}\int_{V-V_\delta} \nabla\nabla g_0\left(\mathbf{r},\mathbf{r}'\right)\cdot\mathbf{J}_e^i\left(\mathbf{r}'\right)dV' \\ &\quad - \mathbf{J}_e^i(\mathbf{r})\cdot\left[\lim_{\delta\to 0}\int_{V-V_\delta}\nabla'\nabla' g_0\left(\mathbf{r},\mathbf{r}'\right)dV' - \int_S \hat{\mathbf{n}}\nabla' g_0\left(\mathbf{r},\mathbf{r}'\right)dS'\right] . \end{aligned} \tag{1.57}$$

where

$$\begin{aligned} \lim_{\delta\to 0}\int_{V-V_\delta}\nabla'\nabla' g_0\left(\mathbf{r},\mathbf{r}'\right)dV' &= \lim_{\delta\to 0}\int_{S-S_\delta}\hat{\mathbf{n}}\nabla' g\left(\mathbf{r},\mathbf{r}'\right)dS' \\ &= \lim_{\delta\to 0}\left[\int_S \hat{\mathbf{n}}\nabla' g\left(\mathbf{r},\mathbf{r}'\right)dS' - \int_{S_\delta}\hat{\mathbf{n}}\nabla' g\left(\mathbf{r},\mathbf{r}'\right)dS'\right] . \end{aligned} \tag{1.58}$$

Therefore,

$$\begin{aligned} j\omega\varepsilon_0\varepsilon\mathbf{E}_e^{(2)} &= \lim_{\delta\to 0}\int_{V-V_\delta}\nabla\nabla g_0\left(\mathbf{r},\mathbf{r}'\right)\cdot\mathbf{J}_e^i\left(\mathbf{r}'\right)dV' - \int_{S_\delta}\nabla g\left(\mathbf{r},\mathbf{r}'\right)\hat{\mathbf{n}}dS'\cdot\mathbf{J}_e^i(\mathbf{r}) \\ &\equiv \lim_{\delta\to 0}\int_{V-V_\delta}\nabla\nabla g_0\left(\mathbf{r},\mathbf{r}'\right)\cdot\mathbf{J}_e^i\left(\mathbf{r}'\right)dV' - \bar{\mathbf{L}}(\mathbf{r})\cdot\mathbf{J}_e^i(\mathbf{r}) , \end{aligned} \tag{1.59}$$

where

$$\bar{\mathbf{L}}(\mathbf{r}) \equiv \int_{S_\delta}\nabla g\left(\mathbf{r},\mathbf{r}'\right)\hat{\mathbf{n}}dS' \tag{1.60}$$

is the depolarizing dyadic which depends solely on the shape of the current source [29]. In total, we write

$$j\omega\varepsilon_0\varepsilon\mathbf{E}_e = \lim_{\delta\to 0}\int_{V-V_\delta}\bar{\mathbf{G}}_{ee}\left(\mathbf{r},\mathbf{r}'\right)\cdot\mathbf{J}_e^i\left(\mathbf{r}'\right)dV' , \tag{1.61}$$

where

$$\bar{\mathbf{G}}_{ee}\left(\mathbf{r},\mathbf{r}'\right) = \bar{\mathbf{G}}_0\left(\mathbf{r},\mathbf{r}'\right) - \bar{\mathbf{L}}\left(\mathbf{r}'\right)\delta\left(\mathbf{r}-\mathbf{r}'\right) \tag{1.62}$$

with

$$\bar{\mathbf{G}}_0\left(\mathbf{r},\mathbf{r}'\right) \equiv \left(k^2\bar{\mathbf{I}} + \nabla\nabla\right) g_0\left(\mathbf{r},\mathbf{r}'\right) , \tag{1.63}$$

$$\bar{\mathbf{L}}\left(\mathbf{r}'\right) \equiv \int_{S_\delta}\nabla' g\left(\mathbf{r}',\mathbf{r}''\right)\hat{\mathbf{n}}dS'' . \tag{1.64}$$

Performing the gradient operations on $g_0(\mathbf{r},\mathbf{r}') = e^{-jkR}/4\pi R$, it can be shown that

$$\nabla\nabla g(\mathbf{r},\mathbf{r}') = R^{-2} g(\mathbf{r},\mathbf{r}') \left\{ \left(3 + 3jkR - k^2R^2\right) \hat{\mathbf{R}}\hat{\mathbf{R}} - (1 + jkR)\,\bar{\mathbf{I}} \right\} \tag{1.65}$$

leading to

$$\bar{\mathbf{G}}_0(\mathbf{r},\mathbf{r}') = R^{-2} g(\mathbf{r},\mathbf{r}') \left[\left(3 + 3jkR - k^2R^2\right) \hat{\mathbf{R}}\hat{\mathbf{R}} + \left(k^2R^2 - jkR - 1\right) \bar{\mathbf{I}} \right] \ . \tag{1.66}$$

1.4.1 The spatial Fourier transform domain

For problems concerning laterally infinite layered media, it is convenient to work in the Spatial Fourier transform domain with respect to $\rho = \bar{\mathbf{I}}_{\parallel} \cdot \mathbf{r}$ (i.e., the vector component of $\mathbf{r}$ that is tangential to the interface between two media) where $\bar{\mathbf{I}}_{\parallel} = \bar{\mathbf{I}} - \hat{\mathbf{z}}\hat{\mathbf{z}}$, with $\bar{\mathbf{I}}$ denoting the unit dyadic and $\hat{\mathbf{z}}$ taken to be the interface normal respectively. Defining the Fourier transform pair $\mathbf{f}(\rho, z) \longleftrightarrow \mathbf{F}(\mathbf{q}, z)$ where

$$\mathbf{f}(\rho, z) = \frac{1}{4\pi^2} \int \mathbf{F}(\mathbf{q}, z)\, e^{-j\mathbf{q}\cdot\rho} d\mathbf{q} \ , \tag{1.67}$$

$$\mathbf{F}(\mathbf{q}, z) = \frac{1}{4\pi^2} \int \mathbf{f}(\rho, z)\, e^{+j\mathbf{q}\cdot\rho} d\rho \ , \tag{1.68}$$

and noting that $\nabla = \nabla_\rho + \hat{\mathbf{z}}\partial_z \longleftrightarrow -j\mathbf{q} + \hat{\mathbf{z}}\partial_z$, Eq. (1.61) transforms as

$$j\omega\varepsilon_0\varepsilon \mathbf{E}_e(\mathbf{q}, z) = \lim_{\delta\to 0} \int_{V - V_\delta} \bar{\mathbf{G}}_{ee}(\mathbf{q}, z, \mathbf{r}') \cdot \mathbf{J}_e^i(\mathbf{r}')\, dV' \ , \tag{1.69}$$

where

$$\bar{\mathbf{G}}_{ee}(\mathbf{q}, z, \mathbf{r}') = \left[\bar{\mathbf{G}}_0(\mathbf{q}, z, z') - \bar{\mathbf{L}}(\mathbf{r}')\, \delta(z - z')\right] e^{j\mathbf{q}\cdot\mathbf{r}'} \ , \tag{1.70}$$

with

$$\bar{\mathbf{G}}_0(\mathbf{q}, z, z') = \left(k^2\bar{\mathbf{I}} - \mathbf{q}\mathbf{q} - j\mathbf{q}\hat{\mathbf{z}}\partial_z + \hat{\mathbf{z}}\hat{\mathbf{z}}\partial_z^2 - j\hat{\mathbf{z}}\mathbf{q}\partial_z\right) g_0(\mathbf{q}, z, z') \tag{1.71}$$

and

$$g_0(\mathbf{q}, z, z') = \frac{e^{-jk_z|z-z'|}}{2jk_z} \ : \ k_z = \sqrt{k^2 - q^2} \tag{1.72}$$

Evaluating the derivatives, we have

$$\partial_z g_0\left(\mathbf{q}, z, z'\right) = -jk_z \mathrm{sgn}\left\{z - z'\right\} g_0\left(\mathbf{q}, z, z'\right) \ , \tag{1.73}$$

$$\partial_z^2 g_0\left(\mathbf{q}, z, z'\right) = -k_z^2 g_0\left(\mathbf{q}, z, z'\right) \ , \tag{1.74}$$

leading to

$$\begin{aligned}
\bar{\mathbf{G}}_0\left(\mathbf{q}, z, z'\right) &= \left(\bar{\mathbf{I}}_{\|} + j\partial_z^{-1}\hat{\mathbf{z}}\mathbf{q}\right) \cdot \bar{\mathbf{I}}_{\|} \cdot \left(k^2 \bar{\mathbf{I}}_{\|} - \mathbf{q}\mathbf{q} - j\mathbf{q}\hat{\mathbf{z}}\partial_z\right) g_0\left(\mathbf{q}, z, z'\right) \\
&= \left(\bar{\mathbf{I}}_{\|} - k_z^{-1}\mathrm{sgn}\left\{z - z'\right\}\hat{\mathbf{z}}\mathbf{q}\right) \cdot \bar{\mathbf{I}}_{\|} \cdot \left(k^2 \bar{\mathbf{I}}_{\|} - \mathbf{q}\mathbf{q} - k_z \mathrm{sgn}\left\{z - z'\right\}\mathbf{q}\hat{\mathbf{z}}\right) g_0\left(\mathbf{q}, z, z'\right) \\
&\equiv \bar{\mathbf{C}}\left(\mathbf{q}\right) g_0\left(\mathbf{q}, z, z'\right) \ ,
\end{aligned} \tag{1.75}$$

where

$$\bar{\mathbf{C}}\left(\mathbf{q}\right) = \left(\bar{\mathbf{I}}_{\|} - k_z^{-1}\mathrm{sgn}\left\{z - z'\right\}\hat{\mathbf{z}}\mathbf{q}\right) \cdot \bar{\mathbf{I}}_{\|} \cdot \left(k^2 \bar{\mathbf{I}}_{\|} - \mathbf{q}\mathbf{q} - k_z \mathrm{sgn}\left\{z - z'\right\}\mathbf{q}\hat{\mathbf{z}}\right) \ . \tag{1.76}$$

In Chap. 2, the scattered fields in the spatial Fourier transform domain for a finite thickness gyrotropic plasma slab are presented in a similar form by defining tensors $\bar{\mathbf{C}}^r\left(\mathbf{q}\right)$ and $\bar{\mathbf{C}}^t\left(\mathbf{q}\right)$ for the reflected and transmitted fields respectively.

1.5 Boundary conditions at a material interface

Boundary conditions on the fields at an interface Σ between two media are

$$\hat{\mathbf{z}} \times \left(\mathbf{H}_1 - \mathbf{H}_2\right)|_{\Sigma} = \mathbf{J}_{es} \ , \tag{1.77}$$

$$\hat{\mathbf{z}} \times \left(\mathbf{E}_1 - \mathbf{E}_2\right)|_{\Sigma} = -\mathbf{J}_{ms} \ , \tag{1.78}$$

$$\hat{\mathbf{z}} \cdot \left(\mathbf{D}_1 - \mathbf{D}_2\right)|_{\Sigma} = \rho_{es} \ , \tag{1.79}$$

$$\hat{\mathbf{z}} \cdot \left(\mathbf{B}_1 - \mathbf{B}_2\right)|_{\Sigma} = \rho_{ms} \ , \tag{1.80}$$

where $\mathbf{J}_{es}$ ($\mathbf{J}_{ms}$) and ρ_{es} (ρ_{ms}) are electric (magnetic) surface currents and charges on the boundary, $\{\mathbf{E}_1, \mathbf{H}_1, \mathbf{D}_1, \mathbf{B}_1\}$ are the fields infinitely close to the boundary on the side into which $\hat{\mathbf{z}}$, the interface normal, is directed, and $\{\mathbf{E}_2, \mathbf{H}_2, \mathbf{D}_2, \mathbf{B}_2\}$ are the fields infinitely close to the boundary on the opposite side. The tangential boundary conditions (1.77)-(1.78) are derived from the curl equations, whereas the normal boundary conditions (1.79)-(1.80) are derived from the divergence equations (i.e., the divergence of the curl equations).

1.5.1 Electrostatic boundary conditions

For electrostatic problems, the field quantities $\{\mathbf{H}, \mathbf{B}, \mathbf{J}_{es}, \mathbf{J}_{ms}\}$ are zero (or approximately zero in quasi-statics), and the only relevant boundary conditions are (1.78) and (1.79). Writing $\mathbf{E} = -\nabla\Phi$, where Φ is the electrostatic potential, and assuming simple, isotropic dielectrics characterized by scalar permittivities and permeabilities in the absence of spatial dispersion, the boundary conditions in terms of the electrostatic potential are

$$\hat{\mathbf{z}} \times (\nabla\Phi_1 - \nabla\Phi_2)|_\Sigma = \mathbf{0} \ , \tag{1.81}$$

$$\hat{\mathbf{z}} \cdot (\varepsilon_1\nabla\Phi_1 - \varepsilon_2\nabla\Phi_2)|_\Sigma = \rho_{es} \ , \tag{1.82}$$

which simplify to

$$(\Phi_1 - \Phi_2)|_\Sigma = C \ , \tag{1.83}$$

$$(\varepsilon_1\partial_z\Phi_1 - \varepsilon_2\partial_z\Phi_2)|_\Sigma = \rho_{es} \ , \tag{1.84}$$

where C is a constant. The potential should be continuous since $\mathbf{E} = -\nabla\Phi$, implying that if Φ is discontinuous, the electric field is infinitely large at the boundary, which is non-physical. Therefore $C = 0$.

Chapter 2

Surface plasmon polaritons on a plasma slab, biased with an external magnetic field

2.1 Introduction

The properties of surface plasmon polaritons in different biased plasma configurations have been widely studied [30–34]; see [35] for a comprehensive review. These basic configurations include (1) the external magnetic bias is perpendicular to the interface, and, correspondingly, the SPP propagation vector, (2) the magnetic bias is parallel to the interface, but perpendicular to the propagation vector, called the Voigt configuration, and (3) the magnetic bias is parallel to the interface and also parallel to the propagation vector, known as the Faraday configuration [33]. In [36], the well-known Voigt configuration is re-examined, and it is shown that the SPPs have topological properties, making a connection with the current work in photonic topological insulators, previously investigated for periodic media [37, 38].

Nonreciprocal topological surface waves have several important features; namely, they are unidirectional, and they operate in the bulk bandgap of a topologically nontrivial material [37–39]. Being strongly nonreciprocal, upon encountering a discontinuity, they are

immune to back-scattering, and because they operate in the bulk bandgap, they do not radiate into the bulk. As such, they are forced to pass over the discontinuity, and the lack of scattering or diffraction makes them interesting from a wave-propagation aspect, and promising for device applications [13–15]. Topological SPPs may be characterized by an integer invariant (e.g., the Chern number), which cannot change except when the underlying momentum-space topology of the bulk bands is changed [40–44]. Thus, another view of the reflection- and diffraction-free aspect of topological SPPs is that they are governed by bulk material properties, so that they are not sensitive to surface features, and can only change qualitatively when the bulk topology changes. A change in topology arises when a bandgap is closed or opened, which occurs for the biased plasma when the bias field is reversed in direction.

The continuum plasma case of Voigt topological SPPs identified in [36] is studied in [40, 43, 45, 46]. SPPs in the Voigt configuration cross the bulk bandgap, and exist above the plasma frequency. In [47, 48], it is observed that SPPs exist below the bandgap, propagating at various angles with respect to the bias direction. Those works are focused on the quantum force on a decaying atom, and in [49] the excitation of these modes is considered using circular-polarized dipole sources. In this chapter, we summarize the findings of [23], which investigates these below-the-gap SPPs in more detail. These SPPs are similar to topological SPPs in the sense that they are unidirectional, operate in a bulk bandgap (and so are diffraction-free), and only change their properties qualitatively when the topology of momentum space is changed. Moreover, and unlike the previously-studied topological SPPs, they form narrow beam-like patterns, similar to the case of hyperbolic media [50, 51]. However, it seems difficult or perhaps impossible to assign a topological integer-invariant to describe these SPPs as they propagate in different directions at different frequencies within the gap, and so, strictly-speaking, these SPPs are not topological. Nevertheless, it is shown that they still exhibit unidirectional propagation and inherent robustness to discontinuities.

The chapter is organized as follows. In Sec. 2.2, the material response for a plasma biased with an external magnetic field is summarized. In Sec. 2.3, a bulk bandgap common

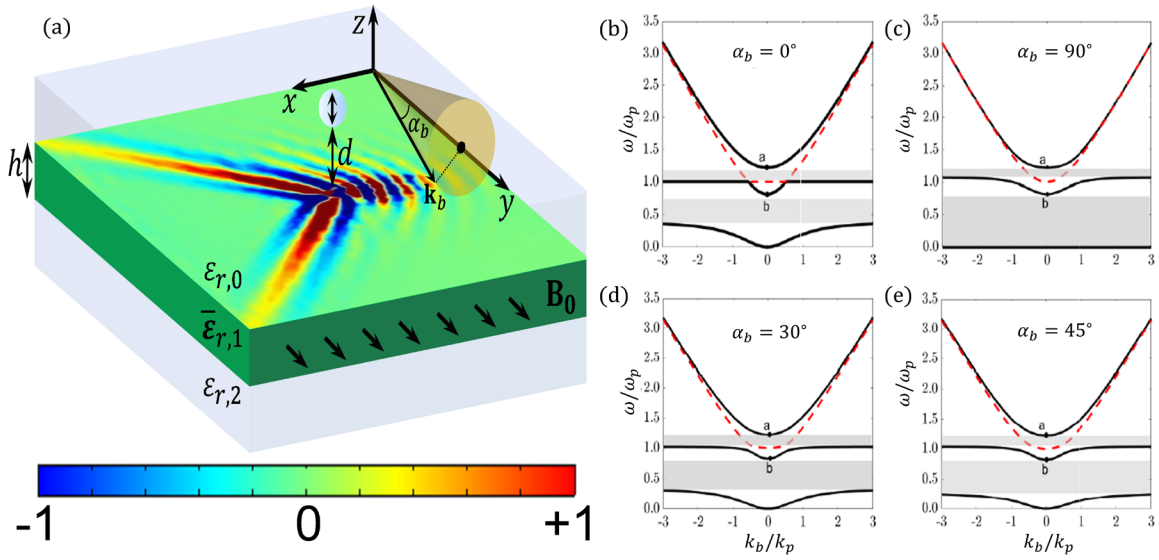

Figure 2-1: (a) A plasma slab of finite thickness h, biased with an external magnetic bias field $\mathbf{B}_0 = B_0\hat{\mathbf{y}}$. A time-harmonic electric dipole current source linearly polarized perpendicular to the interface (i.e., along $\hat{\mathbf{z}}$ is suspended a distance d above the slab and operates at frequency ω. With such a source, operating in the hyperbolic regime, it is possible to excite the (normalized) nonreciprocal SPP field pattern shown. The wave vector $\mathbf{k}_b$ associated with bulk modes that propagate freely within the slab makes an angle α_b with respect to the bias. (b)-(e) Dispersion of bulk modes for several angles of propagation in the range of 0 to 90°, where $k_p = \omega_p/c$. The shaded regions highlight the spectral location of bandgaps in the dispersion. The dashed red trace is associated with the ordinary (bias-independent) mode, while the solid black traces are associated with the extraordinary (bias-dependent) mode. Points labeled a and b on the dispersion diagrams are stationary with respect to the propagation angle.

to all propagation directions of the plasma bulk modes, within which the SPPs propagate, is identified and discussed. In Sec. 2.4, the nonreciprocal dispersion of the SPPs in different frequency regimes and the concept of group velocity is described. In Sec. 2.5, the scattered field excited by a point dipole positioned a distance above the upper interface is obtained for a finite-thickness biased plasma slab and the Poynting vector for the SPPs associated with power flow is recovered. In addition, the back-scattering immune properties of the surface wave propagating at the magnetized plasma-air interface in the presence of a defect in the lower bandgap (hyperbolic) frequency regime is investigated.

2.2 Material response of a biased plasma

The geometry of interest, depicted in Fig. 2-1(a), is a finite-thickness plasma slab of thickness h, immersed in air characterized by relative permittivity $\varepsilon_{r,0} = \varepsilon_{r,2} = 1$ and relative

permeability $\mu_{r,0} = \mu_{r,2} = 1$. The plasma is biased with an external static magnetic bias field $\mathbf{B}_0 = \hat{\mathbf{y}} B_0$. Assuming time harmonic variation $e^{-i\omega t}$, where ω denotes the operating frequency, the biased plasma is characterized by the anisotropic, dispersive relative permittivity tensor,

$$\bar{\varepsilon}_{r,1} \equiv \bar{\varepsilon} = \varepsilon_t \left(\bar{\mathbf{I}} - \hat{\mathbf{y}}\hat{\mathbf{y}} \right) + i\varepsilon_g \left(\hat{\mathbf{y}} \times \bar{\mathbf{I}} \right) + \varepsilon_a \hat{\mathbf{y}}\hat{\mathbf{y}} \ , \tag{2.1}$$

where the permittivity elements $\{\varepsilon_t, \varepsilon_a, \varepsilon_g\}$ are [52]

$$\varepsilon_t = 1 + \frac{\omega_p^2 \left(\omega + i\Gamma\right)}{\omega \left[\omega_c^2 - \left(\omega + i\Gamma\right)^2\right]} \ , \tag{2.2}$$

$$\varepsilon_a = 1 - \frac{\omega_p^2}{\omega \left(\omega + i\Gamma\right)} \ , \tag{2.3}$$

$$\varepsilon_g = \frac{\omega_c \omega_p^2}{\omega \left[\omega_c^2 - \left(\omega + i\Gamma\right)^2\right]} \ , \tag{2.4}$$

where $\omega_p = \sqrt{N q_e^2 / m^* \varepsilon_0}$, $\omega_c = -q_e B_0 / m^*$, and $\Gamma = 1/\tau$ are, respectively, the plasma, cyclotron, and collision frequencies defined in terms of the free electron density N, electron charge $q_e = -e$, effective electron mass m^*, and relaxation time between collisions τ. This permitivity model may correspond to a solid state plasma such as InSb [52]. It should also be noted that the model is local, and therefore does not account for spatial dispersion; as studied in [53, 54], a nonlocal model may lead to the presence of a backward propagating SPP modes. However, the effect of non-locality is evident only for very large wavenumbers, and the backward waves vanish when considering realistic levels of loss [49], and so non-locality is ignored here. Unless otherwise noted, we use $\omega_p/2\pi = 20$ THz, $\Gamma = 0.015\omega_p$ and $\omega_c/\omega_p = 0.4$ to evaluate the permittivity elements in Eq. (2.2). The cyclotron frequency ω_c corresponds to $B_0 = 6.3$ T and $m^* = 0.022 m_e$ where m_e is the electron mass [52].

2.3 Dispersion of bulk modes in a biased plasma

The propagation characteristics of bulk modes in anisotropic media generally depend on the direction of propagation. Therefore, in a anisotropic medium exhibiting bulk band-gaps,

the gaps may also be sensitive to propagation direction. In this section, the dispersion of bulk modes propagating through a biased plasma is studied in order to identify a bulk bandgap that is common to all propagation directions. We begin assuming a plane wave with wavevector $\mathbf{k}_b$, which makes an angle α_b with respect to the bias direction (i.e., $\hat{\mathbf{y}}$) as shown in Fig. 2-1(a). In the absence of impressed sources, a plane wave solution to the wave equation (1.29) of the form $\mathbf{E} = \mathbf{E}_0 e^{i\mathbf{k}_b \cdot \mathbf{r}}$ is recovered for which non-trivial solutions for the amplitude $\mathbf{E}_0$ are obtained when [55]

$$\left| k_0^2 \bar{\varepsilon} - k_b^2 \bar{\mathbf{I}} + \mathbf{k}_b \mathbf{k}_b \right| = 0 \ . \tag{2.5}$$

Writing $\mathbf{k}_b = \mathbf{k}_t + \hat{\mathbf{y}} k_y$ such that $|\mathbf{k}_t| = k_b \sin\alpha_b$ and $k_y = k_b \cos\alpha_b$, evaluation of the determinant leads to the dispersion relation for the bulk modes,

$$\begin{aligned} 0 = & \left[\left(\varepsilon_t^2 - \varepsilon_g^2 + \varepsilon_a \varepsilon_t \right) \sin^2\alpha_b + 2\varepsilon_a \varepsilon_t \cos^2\alpha_b \right] k_0^2 k_b^2 \\ & - \left(\varepsilon_t \sin^2\alpha_b + \varepsilon_a \cos^2\alpha_b \right) k_b^4 - \varepsilon_a \left(\varepsilon_t^2 - \varepsilon_g^2 \right) k_0^4 \ . \end{aligned} \tag{2.6}$$

The dispersion of the bulk modes for different propagation angles are shown in Figs. 2-1(b)-(e). Figures 2-1(b) and 2-1(c) show the dispersion of bulk modes that propagate parallel ($\alpha_b = 0°$) and perpendicular ($\alpha_b = 90°$) to the magnetic bias, respectively. When propagation is perpendicular to the bias, the plane wave decouples into transverse-electric (TE) and -magnetic (TM) modes, where transverse is defined with respect to the propagation direction. On the other hand, when propagation is parallel to the bias, the plane wave decouples into left- and right-handed circularly polarized (RHCP/LHCP) waves [55]. For all other propagation directions, the waves are hybrid. Figures 2-1(d) and 2-1(e) show the dispersion for two propagation angles in the range, $0° < \alpha_b < 90°$.

The points of modal degeneracy that occur for $\alpha_b = 0$ correspond to Weyl points that arise from crossings between longitudinal plasma modes and transverse helical modes [56]. Although the flat dashed red section in Fig. 2-1(b) may appear to naturally belong to the flat solid black dispersion line, the situation admits two viewpoints. For $\alpha_b = 0$, in the

lossless case, one could view the horizontal black line as continuing through the red dashed section, since this represents one polarization, whereas the parabolic sections represent a different polarization. That is, there is an eigenvalue degeneracy, but not an eigenfunction degeneracy. However, analytic continuation for small non-zero angles indicates that the parabolic red dashed section continues to the nearly-flat red dashed section, which is evident in Fig. 2-1(d). As a result, the eigenfunctions and in this case, the eigenvalues cannot be globally defined as smooth analytical functions in k-space.

Two bandgaps form between the other three branches (solid black) as indicated by the shaded regions of Fig. 2-1(b)-(e). The size of the bandgaps depend on the propagation direction as well as the magnetic bias field strength. The upper bandgap is smallest when $\alpha_b = 90°$. Conversely, the lower band-gap is smallest when $\alpha_b = 0°$. As such, we take the smallest upper (lower) band-gap to represent the upper (lower) bandgap common for all propagation angles, $0° < \alpha_b < 90°$. Points labeled a and b on the dispersion diagrams are independent of the propagation angle. The common bandgap and its impact on surface waves is considered further in the following section.

2.4 Dispersion of SPP modes

A surface wave that propagates along the interface at an angle ϕ with respect to $\hat{\mathbf{x}}$, has wavevector $\mathbf{q} = \hat{\mathbf{x}}k_x + \hat{\mathbf{y}}k_y$ where $k_x = q\cos\phi$, $k_y = q\sin\phi$ and $q = |\mathbf{q}| = \sqrt{k_x^2 + k_y^2}$. From the bulk dispersion relation defined in Eq. (2.6), we obtain the solutions $\hat{\mathbf{k}}_{b,j}^{\pm} = \mathbf{q} \pm \hat{\mathbf{z}} i\gamma_j$ for $j \in \{1, 2\}$, where

$$\gamma_1 = \sqrt{k_x^2 + \frac{1}{2}\left(\kappa - \sqrt{\kappa^2 - \upsilon}\right)}\,, \tag{2.7}$$

$$\gamma_2 = \sqrt{k_x^2 + \frac{1}{2}\left(\kappa + \sqrt{\kappa^2 - \upsilon}\right)}\,, \tag{2.8}$$

with

$$\kappa = \left\{ \left(\varepsilon_t + \varepsilon_a\right) k_y^2 - \left[\varepsilon_t \left(\varepsilon_t + \varepsilon_a\right) - \varepsilon_g^2\right] k_0^2 \right\} / \varepsilon_t \ , \tag{2.9}$$

$$\upsilon = \left\{ 4\varepsilon_a \left[\left(\varepsilon_t + \varepsilon_g\right) k_0^2 - k_y^2\right] \left[\left(\varepsilon_t - \varepsilon_g\right) k_0^2 - k_y^2\right] \right\} / \varepsilon_t \ . \tag{2.10}$$

In the surrounding dielectric regions, the solutions are $\hat{\mathbf{k}}^{\pm} = \mathbf{q} \pm \hat{\mathbf{z}} i\gamma_0$ where $\gamma_0 = \sqrt{q^2 - k_0^2}$. The dispersion relation for the SPP is obtained by enforcing continuity in the tangential electric and magnetic fields associated with bulk modes in each region at the interface [47], leading to the 4×4 system of homogeneous equations,

$$\begin{pmatrix} \beta_1^- & \beta_2^- & k_y & i\gamma_0 k_x \\ k_y\theta_1 & k_y\theta_2 & -k_x & i\gamma_0 k_y \\ k_y\phi_1^- & k_y\phi_2^- & i\gamma_0 k_x & -k_0^2 k_y \\ -\delta_1 k_{t,1}^2 & -\delta_2 k_{t,2}^2 & i\gamma_0 k_y & k_0^2 k_x \end{pmatrix} \begin{pmatrix} A_1 \\ A_2 \\ B_1 \\ B_2 \end{pmatrix} = \mathbf{0} \ , \tag{2.11}$$

where $\beta_j^{\pm}$, $\phi_j^{\pm}$, δ_j, and θ_j for $j \in \{1, 2\}$ are defined in Eq. (A.75) of the appendix. Non-trivial solutions for the coefficients $\{A_1, A_2, B_1, B_2\}$ are obtained when the determinant of the prefactor matrix on the left hand side of Eq. (2.11) vanishes. Evaluation of the determinant and dividing through by a factor of $-iq^2 k_y / \varpi_1 \varpi_2 \xi_1 \xi_2 \neq 0$, where ϖ_j and ξ_j are also defined in Eq. (A.75) of the appendix, leads to the SPP dispersion relation

$$\begin{aligned} 0 = &\left(k_y^2 - \gamma_0^2\right) Q_A - k_x Q_B^- + k_x k_y^2 Q_C^- \\ &- \left(k_x^2 - \gamma_0^2\right) Q_D^- + \gamma_0 \left(Q_E^- - \chi^-\right) \ , \end{aligned} \tag{2.12}$$

where the quantities Q_A, Q_B^-, Q_C^-, Q_D^-, Q_E^- and χ^- are defined in Eqs. (A.67)-(A.71) and (A.74) of the appendix. For the well-studied case of propagation perpendicular to the bias ($k_y = 0$) the SPP dispersion relation is found to be [35, 36]

$$\sqrt{k_x^2 - k_0^2} + \frac{\sqrt{k_x^2 - k_0^2 \varepsilon_{eff}}}{\varepsilon_{eff}} = \frac{\varepsilon_g k_x}{\varepsilon_t \varepsilon_{eff}} \ , \tag{2.13}$$

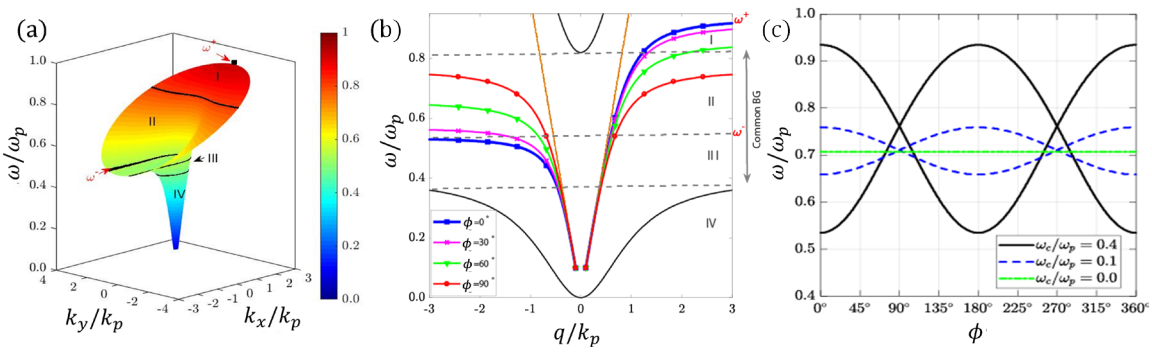

Figure 2-2: (a) Dispersion surface of SPPs that are guided along the plasma-air interface, obtained by solving Eq. (2.12) via numerical root search. The solid black lines denote contours of constant frequency (i.e., equi-frequency contours) in each of the four regions, denoted I, II, III, and IV, of the dispersion surface. Frequencies $\omega^{\pm}$ satisfy the SPP resonance condition (i.e., $q \to \infty$) for $\phi = 0$ (i.e., SPP propagation is perpendicular to the bias) defined in Eq. (2.18). (b) Dispersion contours in the ω-q plane for a variety of propagation angles ϕ. For $q \gtrless 0$, ϕ is made with respect to the $\pm\hat{\mathbf{x}}$ directions. In addition, the dispersion of bulk modes propagating parallel to the bias (i.e., $\alpha_b = 0$) is shown, where the corresponding bandgap is common to all propagation angles α_b. For contrast, the bulk dispersion light in the interfaced medium (i.e., vacuum) is indicated by the solid orange lines. (c) Solutions to the quasi-static SPP dispersion relation, Eq. (2.16), for a finite thickness slab of thickness $h = 0.25\lambda_p$ and wavenumber $q = 10k_p \gg 1/h$. For a given operation frequency, a maximum of four beams is possible in the SPP beam pattern, two of which are associated with the upper interface while the other two are associated with the lower interface. The cyclotron frequency, being proportional to the magnetic bias, ranges from 0 to $0.4\omega_p$.

where $\varepsilon_{eff} = \left(\varepsilon_t^2 - \varepsilon_g^2\right)/\varepsilon_t$ is the effective Voigt permittivity. However, for $k_y \neq 0$, the general dispersion equation, Eq. (2.12), must be used.

An SPP guided along the interface generally possesses two wavevector components, k_x and k_y. Therefore, a three-dimensional surface is needed to fully describe the SPP dispersion. Fig. 2-2(a) shows a 3D perspective view of the dispersion surface, while Fig. 2-2(b) shows traces of the SPP dispersion in the q-ω plane for several angles of propagation ϕ. In Fig. 2-2(b), SPPs propagating with different propagation angles ϕ are shown to cross the common bulk bandgap associated with $\alpha_b = 0°$. For a select propagation angle ϕ, the SPP resonant frequency ω_{SPP} is recovered in the limit $q \to \infty$, and may be derived using quasi-static (large q) approximation. The maximum and minimum resonance frequencies ω^+ and ω^-, associated with $\phi = 0$ and $\phi = 180°$ respectively, are labeled in Figs. 2-2(a) and 2-2(b). In addition, the spectral region $0 < \omega < \omega_p$ is subdivided into four frequency regions, each corresponding to different propagation behavior. In regions I and IV, there is no common bulk bandgap, whereas in Regions II and III, there exists a common bulk

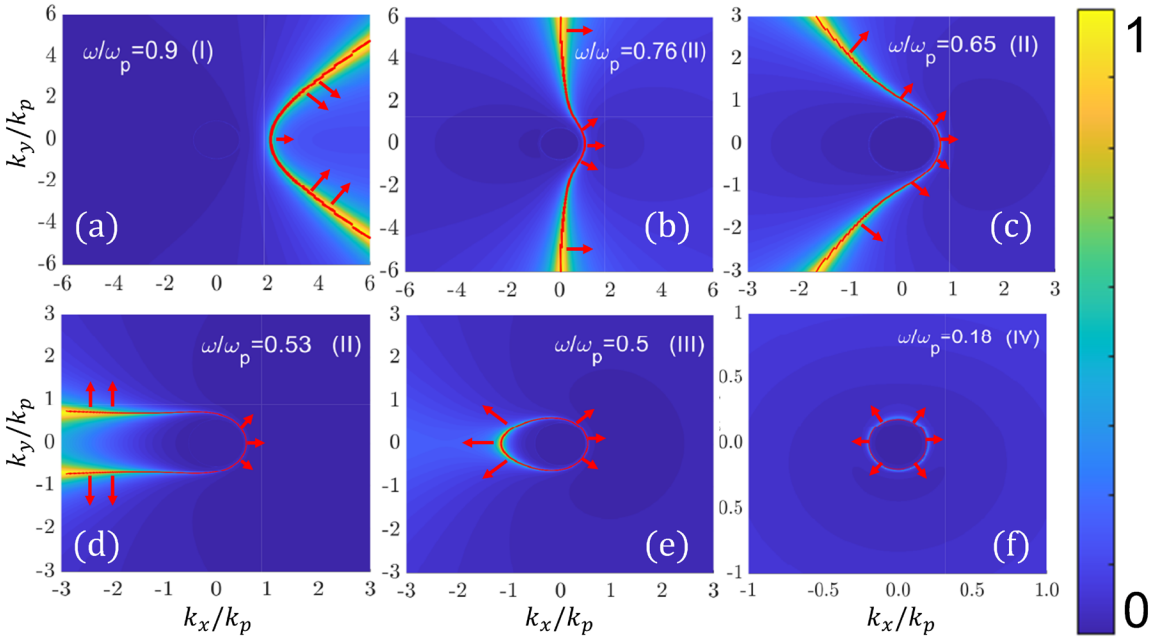

Figure 2-3: Density maps of the SPP dispersion relation defined in Eq. (2.12) in the k_x-k_y plane, and equi-frequency contours (red solid lines) extracted numerically from the dispersion surface shown in Fig. 2-2(a) for operating frequencies in each of the four regions I, II, III, and IV. Each of the selected operating frequencies are normalized with respect to the plasma frequency ω_p. Red arrows that point perpendicular to each contour indicate the direction of group velocity, representing the directional flow of electromagnetic energy in the lossless case.

bandgap. In region III propagation is nonreciprocal, but far from unidirectional. In region IV, propagation is weakly nonreciprocal to reciprocal. In regions II and III, propagation is unidirectional (i.e., there exists no backward mode) for select propagation angles. Because SPP propagation is unidirectional and exists within the common bulk bandgap in region II, region II is of particular interest. Further analysis of the equi-frequency contours in region II also suggests that the dispersion is hyperbolic, with the resultant field pattern consisting of two narrow beams, symmetric with respect to $\hat{\mathbf{x}}$ [23, 47–49], along which the energy propagates.

Figure 2-3 shows several equi-frequency contours in the x-y plane of the dispersion surface at several different frequencies as indicated by the solid red lines. Beneath each contour, a density map of the dispersion relation at each of the selected operating frequencies

is also shown. The phase and group velocities of the SPP are given by $\mathbf{v}_p = \hat{\mathbf{q}}\omega/q$ and

$$\mathbf{v}_g = \nabla_{\mathbf{q}}\omega\left(\mathbf{q}\right) = \hat{\mathbf{x}}\frac{\partial\omega}{\partial k_x} + \hat{\mathbf{y}}\frac{\partial\omega}{\partial k_y}\ , \tag{2.14}$$

respectively, meaning that the group velocity, representing the directional flow of electromagnetic energy in the lossless case, is orthogonal to the equi-frequency contours. The group velocity vectors are shown in Fig. 2-3 by red arrows. According to Fig. 2-3(f), the contours at operating frequencies in region IV are circular, such that energy flows isotropically. The resulting field pattern is therefore omni-directional. As frequency increases, the semi-major axis (i.e., the one oriented along $\hat{\mathbf{x}}$) of the contour becomes elongated as seen in Fig. 2-3(e) such that the energy propagation is anisotropic and nonreciprocal. For $\omega = 0.53\omega_p$, the contour enters the hyperbolic regime (i.e., spectral regions I and II) with the arms of each contour widening as frequency increases, as shown in Fig. 2-3(a)-(d). For frequencies that increase beyond $0.76\omega_p$ in region I, the contour arms change direction from the left halfplane to the right. The hyperbolic contours result in narrow SPP beams that form in the field pattern with the group velocity vectors pointing along the beam directions. Near the SPP resonance (i.e., $q \to \infty$) the group velocity is a small fraction of the speed of light in vacuum, less than $0.05c$, where c is the speed of light in vacuum.

2.4.1 The quasi-static limit

Further insight into the properties of SPPs excited on the surface of a biased plasma slab is gained via the quasi-static approximation which is valid when the SPPs have short wavelengths relative to freespace, or equivalently, have a large momentum relative to the freespace wavenumber (i.e., $q \gg k_0$). In the quasi-static approximation, the electric field is defined in terms of the scalar electro-static potential Φ, such that $\mathbf{E} \approx -\nabla\Phi$, assuming the associated magnetic field $\mathbf{H}$ is negligible. Solving Gauss' law in the regions above and below the slab, and enforcing boundary conditions on the tangential components of the electric field at each interface, the electric potential for a slab like the one shown in Fig. 2-1 is

obtained as $\phi_{\mathbf{q}} = CF(z)\, e^{i\mathbf{q}\cdot\mathbf{r}}$ where C is an arbitrary coefficient and

$$F = \begin{cases} e^{-qz} & z > 0 \\ \cosh\tilde{q}z + iA\sinh\tilde{q}z & -h < z < 0, \\ (\cosh\tilde{q}h - iA\sinh\tilde{q}h)\, e^{q(z+h)} & z < -h \end{cases} , \tag{2.15}$$

where $\tilde{q} = \sqrt{k_x^2 + \varepsilon_a k_y^2/\varepsilon_t}$ and A is a complicated function of the material response (omitted since it is not needed in the following). Enforcing continuity of the normal components of electric displacement vector $\mathbf{D}$ at the two interfaces leads to the quasi-static SPP dispersion relation

$$\varepsilon_g^2 k_x^2 - \varepsilon_t^2 \tilde{q}^2 - q^2 = 2\varepsilon_t q\tilde{q}\coth\tilde{q}h \ . \tag{2.16}$$

In the thick slab limit (i.e., $h \to \infty$), the dispersion relation reduces to that derived for a single interface [47],

$$q + k_x\varepsilon_g + \tilde{q}\varepsilon_t = 0 \ . \tag{2.17}$$

Substituting the permittivity model defined in Eqs. (2.1)-(2.2) into Eq. (2.17), the solutions ω_{SPP} are obtained as [47]

$$\omega_{\mathrm{SPP}} = \frac{1}{2}\left[\omega_c\cos\phi + \sqrt{2\omega_p^2 + \omega_c^2\left(1+\sin^2\phi\right)}\right] \ . \tag{2.18}$$

Figure 2-2(c) shows numerical solutions to the quasi-static SPP dispersion relation, Eq. (2.16), for a magnetized plasma slab with a thickness of $h = 0.25\lambda_p$, and for several values of cyclotron frequency, corresponding to the SPP resonant frequency ω_{SPP} in the quasi-static limit. For a given ω value, there are four values of ϕ, two of which correspond to forward beams at the upper interface while the other two correspond to backward beams at the lower interface. This suggests that four beams may be present in the scattered field profile for operating frequencies that fall within the SPP resonant range $\omega^- < \omega_{\mathrm{SPP}} < \omega^+$. For example, consider an operating frequency of $\omega = 0.65\omega_p$ and cyclotron frequency $\omega_c = 0.4\omega_p$. From the quasi static dispersion, we find that the in-plane wavevector, and hence, phase

velocity, of the SPP makes an angle $\phi \in \{58°, 122°, 238°, 302°\}$ with respect to $\hat{\mathbf{x}}$. The group velocity (i.e. the direction of energy propagation as indicated by the direction of the beams in the lossless limit) of the SPP is perpendicular to the phase velocity and therefore, makes an angle $\phi \pm 90° \in \{148°, 32°, 328°, 212°\}$ with respect to $\hat{\mathbf{x}}$. Furthermore, in the presence of a magnetic bias, the SPP resonance depends on the direction of the SPP modes, however, it is independent of the slab thickness for large values of q. As the magnetic bias tends toward zero (i.e., $\omega_c \to 0$), the SPP resonance becomes a constant flat curve, indicating that the SPP resonance is direction independent, with $\omega_{\text{SPP}} \to \omega_p/\sqrt{2} \simeq 0.7\omega_p$.

2.5 SPP field profile

In this section, we extend the analysis provided in [47] for a single interface to a finite-thickness slab. We present a closed-form solution for the scattered fields due to an electric point source with arbitrary polarization as a 2D inverse Fourier transform (Sommerfeld) integral in the dielectric regions above and below the slab, which we take to be air. In addition, we provide the Sommerfeld integrand in quotient form for each case, which leads to the identification of the SPP dispersion relation when setting the denominator to zero.

The procedure to derive the scattered fields follows from [47, 57]. The incident field excited by an impressed electric dipole current source $\mathbf{J}_e^i = \mathbf{J}_0 \delta(\mathbf{r} - \mathbf{r}_0)$ suspended a distance d above the upper interface, is given by

$$\mathbf{E}(\mathbf{r}) = \left(\nabla\nabla + \bar{\mathbf{I}} k_0^2\right) \cdot \pi(\mathbf{r}) \ , \tag{2.19}$$

where

$$\pi(\mathbf{r}) = g(\mathbf{r}, \mathbf{r}_0) \frac{\mathbf{J}_0}{-i\omega\varepsilon_0} \ , \tag{2.20}$$

denotes the associated principal Hertzian vector potential, defined in terms of the scalar Green's function

$$g(\mathbf{r}, \mathbf{r}_0) = e^{ik_0|\mathbf{r}-\mathbf{r}_0|}/4\pi|\mathbf{r} - \mathbf{r}_0| \ , \tag{2.21}$$

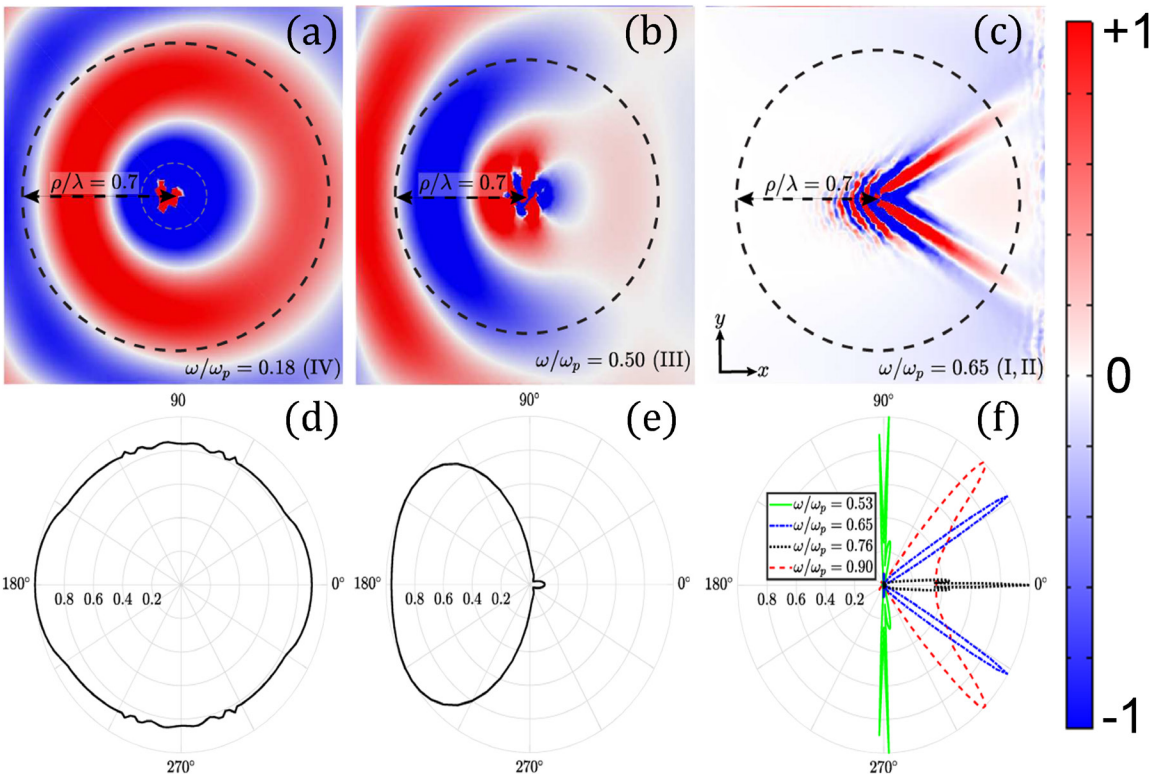

Figure 2-4: (a)-(c) COMSOL generated $\hat{\mathbf{z}}$-component of the normalized reflected electric field near the upper interface of a sufficiently thick slab, excited by an electric dipole current source linearly polarized along $\hat{\mathbf{z}}$. The dashed circles of radius $\rho = 0.7\lambda$ indicate the spatial contour for which the $\hat{\mathbf{z}}$-component of the normalized reflected electric field defined by the 2D inverse Fourier transform integral in Eq. (2.24) is evaluated. (d)-(f) Polar patterns of $|E_z^r|$, evaluated for $(\rho, z, \varphi) = (0.7\lambda, 0.016\lambda_p, 0 < \varphi < 2\pi)$, and $\Gamma = 0.015\omega_p$, at operating frequencies that correspond to panels (a)-(c) respectively. In addition to the operating frequency considered in panel (c), panel (f) shows results for several other operating frequencies in the hyperbolic regime. $\lambda = 2\pi c/\omega$ denotes the free space wavelength and $\lambda_p = 2\pi c/\omega_p$.

where $\mathbf{r}_0$ denotes the source point. The scattered (i.e., reflected, and transmitted) electric fields for a biased-plasma slab of finite thickness are then written generally as 2D inverse Fourier transform (Sommerfeld) integrals

$$\mathbf{E}^r(\mathbf{r}) = \frac{1}{4\pi^2}\int d\mathbf{q} e^{i\mathbf{q}\cdot(\mathbf{r}-\mathbf{r}_0)}\frac{e^{-\gamma_0(d+z)}}{2\gamma_0}\bar{\mathbf{C}}^r(\mathbf{q})\cdot\frac{\mathbf{J}_0}{-i\omega\varepsilon_0}\,, \tag{2.22}$$

$$\mathbf{E}^t(\mathbf{r}) = \frac{1}{4\pi^2}\int d\mathbf{q} e^{i\mathbf{q}\cdot(\mathbf{r}-\mathbf{r}_0)}\frac{e^{-\gamma_0(d-z)}}{2\gamma_0}\bar{\mathbf{C}}^t(\mathbf{q})\cdot\frac{\mathbf{J}_0}{-i\omega\varepsilon_0}\,, \tag{2.23}$$

where $\bar{\mathbf{C}}^r(\mathbf{q})$ and $\bar{\mathbf{C}}^t(\mathbf{q})$ are tensors, similar to the one defined for the principal (incident) field in Eq. (1.76), defined in terms of the reflection and transmission tensor coefficients for the biased-plasma slab, derived in Sec. A.1 of the appendix. From the associated scattered

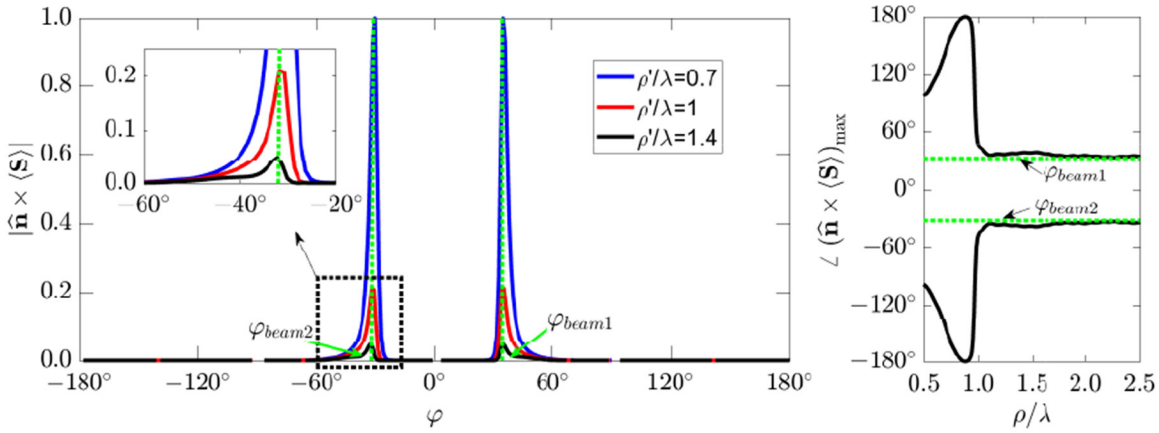

Figure 2-5: (a) magnitude of the time-averaged SPP Poynting vector (i.e., the Poynting vector component parallel to the interface) for observation points of constant radial displacement from the source and height above the interface, $(\rho, z, \varphi) = (\rho', 0.016\lambda_p, -\pi < \varphi < \pi)$, where each value of ρ' is provided in the legend. (b) In-plane angular coordinate of the Poynting vector maximum verses radial displacement from source where $\widehat{\mathbf{n}} = \widehat{\mathbf{z}}$ denotes the interface normal. The horizontal dashed lines highlight the angular coordinate of the group velocity. As expected the Poynting vector is aligned with the group velocity in the far field (i.e., for $\rho/\lambda > 1$). The operating and loss rate frequencies are $\omega = 0.65\omega_p$ and $\Gamma = 0.015\omega_p$, respectively.

magnetic Fourier components $\omega\mu_0\mathbf{H}(\mathbf{q}, z) = \mathbf{k}_0 \times \mathbf{E}(\mathbf{q}, z)$ where $\mathbf{k}_0 = \mathbf{q} + \hat{\mathbf{z}} i\gamma_0$, the time averaged Poynting vector is obtained as $\langle \mathbf{S} \rangle = \mathrm{Re}(\mathbf{E} \times \mathbf{H}^*)/2$. In the numerical examples to follow, we consider the $\hat{\mathbf{z}}$-component of the scattered electric field due to a linear polarized current source with $\mathbf{J}_0 = \hat{\mathbf{z}} J_0$, placed at a height d above a symmetric slab of thickness h for which $\mathbf{r}_0 = (0, 0, d)$. In this case, the $\hat{\mathbf{z}}$-component of the scattered field simplifies to

$$E_z^r(\mathbf{r}) = \frac{1}{4\pi^2} \int d\mathbf{q} e^{i\mathbf{q}\cdot\mathbf{r}} \frac{e^{-\gamma_0(d+z)}}{2\gamma_0} C_{zz}^r(\mathbf{q}) \frac{J_0}{-i\omega\varepsilon_0} , \tag{2.24}$$

$$E_z^t(\mathbf{r}) = \frac{1}{4\pi^2} \int d\mathbf{q} e^{i\mathbf{q}\cdot\mathbf{r}} \frac{e^{-\gamma_0(d-z)}}{2\gamma_0} C_{zz}^t(\mathbf{q}) \frac{J_0}{-i\omega\varepsilon_0} . \tag{2.25}$$

For a linearly polarized dipole current source with amplitude $J_0 = 1\mathrm{A}\cdot\mathrm{m}$ located at the upper interface (i.e., $d = 0$), Fig. 2-4(a),(b),(c) shows the scattered field profile generated using finite element method simulations in COMSOL, for observation points near the interface such that $z = 0.016\lambda_p$, while Figs. 2-4(d),(e),(f) show the normalized magnitude of $|E_z^r(\mathbf{r})|$ calculated via Eq. (2.24) at observation points $\rho = 0.7\lambda$, $z = 0.016\lambda_p$, $0 < \varphi < 2\pi$, and $h \gg \lambda_p$ for several operating frequencies that lie in the four regions of the dispersion surface shown in Fig. 2-2(a),(b). As shown in Fig. 2-4(a),(d), the expected behavior of

surface wave propagation for operating frequencies that lie in region IV of the dispersion is reciprocal and omnidirectional. Figures 2-4(b),(e) confirm that SPP propagation in region III of the spectrum is nonreciprocal, with the SPP intensity concentrated to the left half plane. As frequency increases from region IV to regions II and I of Fig. 2-2(b), the SPP becomes unidirectional and hyperbolic, forming narrow beams directed into the right half-plane. Interestingly, for frequencies that satisfy the SPP resonant condition, $\omega^- < \omega < \omega^+$ (regions I and II), Figs. 2-4(c),(f), show that narrow-beamed directional propagation is obtained, consistent with the previous discussion on equi-frequency contours. In the polar pattern of Fig. 2-4(f), at $\omega = \omega^- = 0.53\omega_p$, the field pattern forms two narrow beams that approach each other as the operating frequency increases. Eventually, the two beams join to form a single beam at $\omega = 0.76\omega_p$, corresponding to the saturation frequency of the $\phi = 90^\circ$ branch in Fig. 2-2(b), and then splits to form two beams for $0.76\omega_p < \omega < \omega^+$. Therefore, the angle of the beams with respect to the $\hat{\mathbf{x}}$ is tunable with respect to frequency and magnetic bias. In the following, we restrict our focus to SPP properties in the resonance frequency range, $\omega^- < \omega < \omega^+$ where two narrow beams form in the SPP field pattern. In particular, we assume the operating frequency $\omega = 0.65\omega_p$, for which we find two beams having angles $\varphi_{beam1,2} = \pm 32^\circ$ with respect to the $\hat{\mathbf{x}}$-axis. In these simulations and ones to follow, an extremely fine adaptive physics based tetrahedral mesh, defined in the COMSOL software, was used. At the edges of the computational domain, a perfectly matched layer (PML) was applied to mimic an open and nonreflecting infinite domain.

In the general lossy case, the group velocity is ill-defined as an energy transport velocity, and therefore, one should rigorously examine the Poynting vector. The magnitude of the Poynting vector associated with SPPs at $\omega = 0.65\omega_p$ for observation points of constant radial displacement from the source and height above the interface is shown in Fig. 2-5(a). For each radial displacement there are two peak values which occur at the angular position $\varphi_{beam1,2}$ of the narrow beams. To find the angular direction of maximum radiation power flow, the angle of the Poynting vector for points located along the beams is extracted and plotted with respect to radial displacement from the source in Fig. 2-5(b). As shown, the

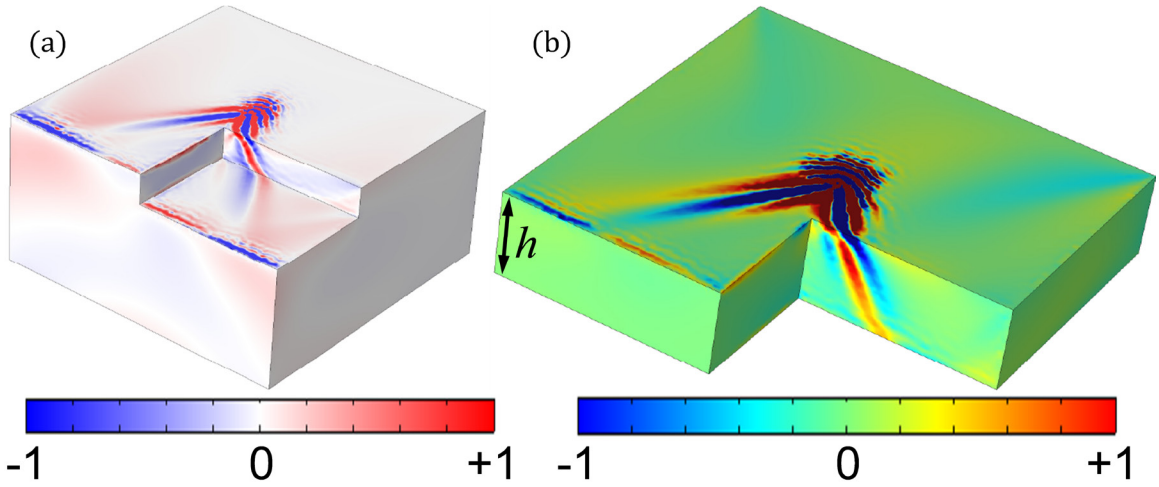

Figure 2-6: COMSOL generated normalized reflected field distribution near the interface of (a) a half-space biased plasma in the presence of a step discontinuity, and (b) a slab of thickness $h = 0.12\lambda_p$. The unidirectional nature of the SPP makes it immune to reflection when encountering the discontinuity.

Poynting vector angle converges to the beam angles in the far-field of the source. That is, the Poynting vector and predicted group velocity point in the same direction, confirming that loss does not significantly impact the direction of energy transport.

SPPs that fall within the resonant range are robust to the presence of discontinuities. To have an indication of the inherent robustness of these SPPs, a discontinuity in the form of a hole/block is constructed in an attempt to impede the SPP. A unidirectional SPP that crosses a band gap in reciprocal space is also immune to the effects of diffraction into the plasma. To illustrate this, Fig. 2-6(a) shows the electric field due to an electric point source near the vacuum-plasma interface. The SPP passes through the discontinuity without reflection or diffraction into the plasma. Similar to the single-interface configuration, SPPs propagating on the plasma slab are also robust to discontinuities. As shown in Fig. 2-6(b), upon encountering the plasma edge, SPPs pass onto the lower interface without reflection or diffraction into the plasma.

For a finite thickness slab, we consider the excitation of SPPs at the upper ($z = 0$) and lower ($z = -h$) interfaces due to a linearly polarized (along $\hat{\mathbf{z}}$) dipole point source positioned at the upper interface ($d = 0$). Figure 2-7(e)-(g) shows how the beams at the upper interface evolve with slab thickness for a set observation point $(\rho, z, \varphi) = (0.5\lambda, 0.03\lambda, 0 < \varphi < 2\pi)$

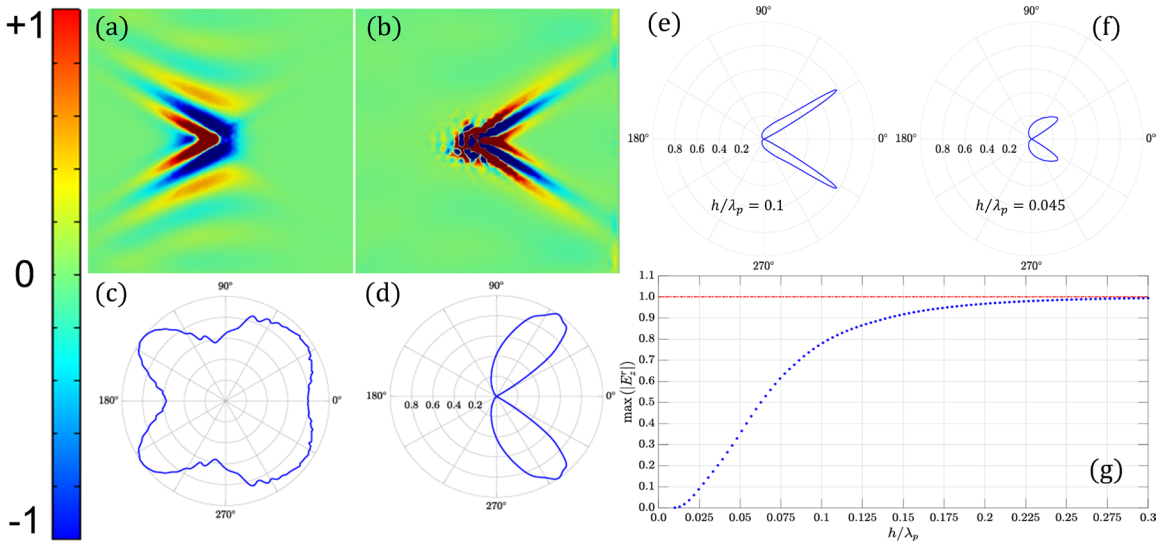

Figure 2-7: (a),(b) COMSOL generated normalized SPP field profile ($\hat{\mathbf{z}}$-component) excited at the (a) lower and (b) upper interfaces of a thin slab of thickness $h = 0.04\lambda_p$ by a vertical dipole source located at the upper interface. (c),(d) Magnitude of the scattered electric field ($\hat{\mathbf{z}}$-component) at the (c) lower and (d) upper interfaces obtained via the evaluation of the Sommerfeld integral in Eqs. (2.24) and (2.25) respectively, where the in-plane displacement from the source is $\rho = 0.5\lambda$. (e),(f) SPP field profile excited at the upper interface shown for two values of thickness, $h = 0.1\lambda_p$ and $h = 0.045\lambda_p$. (g) Maximum of $|E_z^r|$ plotted verses slab thickness. For a sufficiently thick slab $h > 0.3\lambda_p$, $\max(|E_z^r|)$ is maximized. The results shown in (e)-(g) are normalized with respect to 5×10^{14}V/m, obtained for a thick slab in the limit $h \to \infty$, assuming the amplitude of the electric current source is $J_0 = 1$ A $\cdot$ m.

and thickness values that fall within the range $0 < h < 0.3\lambda_p$. The frequency of operation is set within the common bulk bandgap of the plasma, $\omega = 0.65\omega_p$, and the collision frequency is set to $\Gamma = 0.015\omega_p$. The values of thickness considered in Fig. 2-7(e),(f) are $h = 0.1\lambda_p$ and $h = 0.045\lambda_p$ respectfully. Each pattern is normalized with respect to the beam maximum obtained for a thick slab, $|E_z^r|_{\max} = 5 \times 10^{14}$ V/m, in the limit $h \to \infty$, assuming the magnitude of the electric current source is $J_0 = 1\text{A} \cdot \text{m}$. In Fig. 2-7(e) it is shown that the beam maximum grows logistically with thickness and asymptotically approaches the thick slab limit.

When the slab becomes thin enough, it is also possible that a source on the upper interface excites SPPs on the lower interface where the two lower-surface SPP beams are in the opposite direction of the SPP beams on the top interface. Figure 2-7(a),(b) shows the scattered electric field profile at the lower ($z = -h$) and upper ($z = 0$) interfaces respectively, obtained using the finite element method in COMSOL, while Fig. 2-7(c),(d)

shows the magnitude of the transmitted and reflected fields obtained by evaluating the Sommerfeld integrals, defined in Eqs. (2.24) and (2.25), for a small distance below and above the slab. For a thin slab, two forward beams form at the upper interface while two backward beams form at the lower interface.

2.6 Summary

In this chapter, we investigated the behavior of SPPs propagating at the interface between air and gyrotropic plasma for both single-interface and finite-thickness biased-plasma slab configurations. We identified a bulk bandgap, common to all propagation angles, and chose the operating frequency to lie within the common band gap, wherein omni-directional, bidirectional, and narrow directional SPP beam patterns were observed. Operating in the bandgap gives the SPP interesting properties that protect it from backscatter and diffraction in the presence of a discontinuity. The direction of the SPP beams are tunable with operation frequency and also the external magnetic bias field. The scattered fields excited by a near field point source and a quasi-static approximation to the dispersion were also obtained analytically for a finite-thickness slab.

Chapter 3

Magneto-optics and chiral plasmonics with two-dimensional materials

---

Figure 3-1 shows the (a) top and (b) side views of a nonreciprocal quasi-2D CrI_3-graphene heterostructure at the atomic level. Further details are provided in Sec. 3.4.

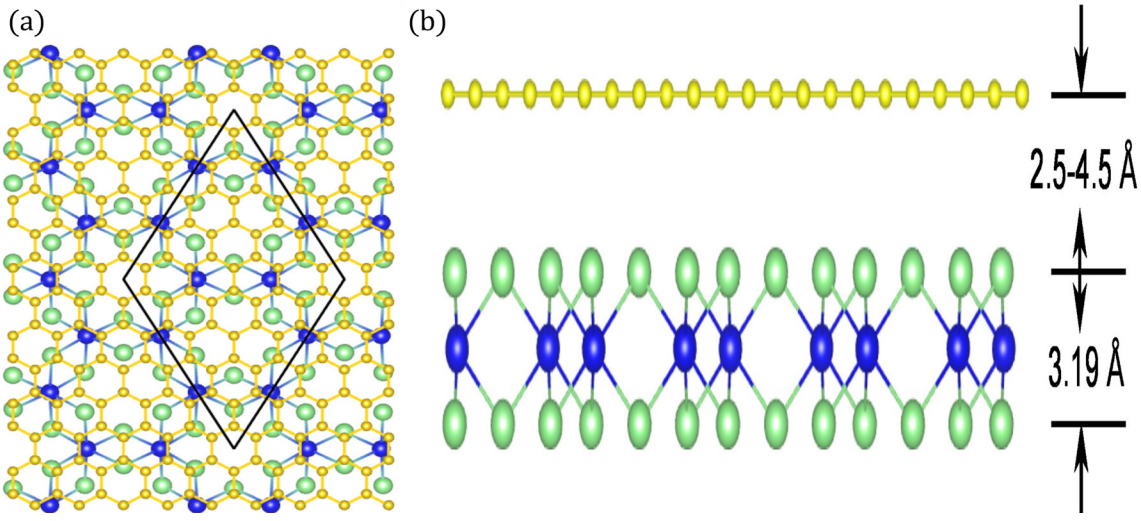

Figure 3-1: (a) Top and (b) side views of a quasi-2D CrI_3-graphene heterostructure at the atomic level (Carbon, C: yellow, Chromium, Cr: blue, Iodine, I: green), with the commensurate supercell outlined in black. The interatomic separation between the graphene (upper) and CrI_3 (lower) layers is varied between 2.5 and 4.5 Å.

3.1 Introduction

Since the discovery of graphene [58,59] and other two-dimensional materials such as the transition metal dichalchogenides (TMDs) [60], transition metal oxides (TMOs) [61–63], boron nitride (BN) [64–66], black phosphorous (BP) [67–71], borophene [72], and α-MoO_3 [73], plasmonics research has continued to grow as many of these materials have useful conductive properties, making it possible for them to support robust SPPs with large confinement and propagation length. In addition, the study of quasi-2D van der Waals heterostructures consisting of two or more of these materials in parallel, is of growing popularity [25, 74–79]. In contrast to artificial metasurfaces [80–83], where design parameters such as the unit cell and periodicity govern behavior, interactions at the atomic level are the driving factor behind the unique optical and electronic properties of natural 2D/quasi-2D materials.

For both artificial and natural materials, a tensor response function can arise. Of particular interest are materials and metasurfaces with anisotropic qualities due to asymmetry (i.e., time-reversal and/or translational) which are especially attractive in applications sensitive to polarization and/or the propagation direction. Translational asymmetry is found naturally in the crystal lattice of black phosphorous and in patterned isotropic materials [84–86]. Time reversal symmetry is broken in gapped Dirac materials pumped with an AC plane wave [87] and in materials biased with an external magnetic field [23, 88–90].

The novel properties of SPPs guided at the surface of two-dimensional materials are heavily dependent on the conductivity. In addition to low loss, a strong SPP response is obtained when the diagonal elements of the conductivity tensor are an order of magnitude larger than the conductance quantum [91] $G_0 = 2e^2/h$ where e and h denote the fundamental charge unit and Planck's constant respectively. For isotropic materials, the capacitive/inductive nature of the conductivity is determined very simply by the sign of the imaginary part, and governs the propagation of transverse-electric/magnetic (TE/TM) SPP modes [92, 93] where transverse is defined with respect to the propagation direction. In the time convention $\exp(-i\omega t)$, a capacitive/inductive local, dispersive conductivity has $\mathrm{Im}\{\sigma(\omega)\} \lesseqgtr 0$ and $\mathrm{Re}\{\sigma(\omega)\} > 0$ with the real part accounting for loss. For anisotropic

materials, the SPP modes are hybrid, generally having some combination of TE and TM polarizations. These hybrid modes are commonly referred to as quasi-TE/TM (QTE/QTM) depending on which polarization is dominant, and likewise experience a capacitive/inductive response that, in addition to frequency ω, depends on the propagation direction [24].

The chapter is organized as follows. In Sec. 3.2, the material response tensor of an arbitrary two-dimensional material is presented, and a change of basis is performed which makes characterizing the response as capacitive/inductive with respect to the propagation direction straightforward. In Sec. 3.3, the dispersion of quasi-TE/TM bulk modes is recovered by solving the wave equation and enforcing boundary conditions at the interface. In Secs. 3.3.1 and 3.3.2 the dispersion and response tensor for two anisotropic 2D materials are provided which demonstrates the effectiveness of response characterization to predict the spectral location of bandgaps in the dispersion of quasi-TM SPP modes. In Sec. 3.4 the material response of a new quasi-2D van der Waals heterostructure recently described in Ref. [25] is summarized, and the properties of unidirectional SPPs guided along the edge of such a material are investigated. In Sec. A.3 of the appendix, a full derivation of the quasi-static edge SPP dispersion relation is provided.

3.2 Material response of a two-dimensional material

In the following, we consider a local, dispersive, anisotropic two-dimensional material embedded in a simple, isotropic medium characterized by permittivity ε and permeability μ, depicted in Fig. 3-2(a). Dominating the response is the surface conductivity, represented generally in the standard (Cartesian) basis as

$$\bar{\sigma}_s(\omega) = \begin{pmatrix} \sigma_{\hat{\mathbf{x}}\hat{\mathbf{x}}}(\omega) & \sigma_{\hat{\mathbf{x}}\hat{\mathbf{y}}}(\omega) \\ \sigma_{\hat{\mathbf{y}}\hat{\mathbf{x}}}(\omega) & \sigma_{\hat{\mathbf{y}}\hat{\mathbf{y}}}(\omega) \end{pmatrix}, \tag{3.1}$$

with the condition $\sigma_{\hat{\mathbf{x}}\hat{\mathbf{y}}}(\omega) = -\sigma_{\hat{\mathbf{y}}\hat{\mathbf{x}}}(\omega)$. To characterize the response, it is convenient to work in a coordinate system spanned by the set of orthonormal basis vectors $\{\hat{\mathbf{q}}, \hat{\mathbf{z}}, \hat{\mathbf{z}} \times \hat{\mathbf{q}}\}$ where $\mathbf{q}$ denotes the in-plane momentum. The representation of the surface conductivity

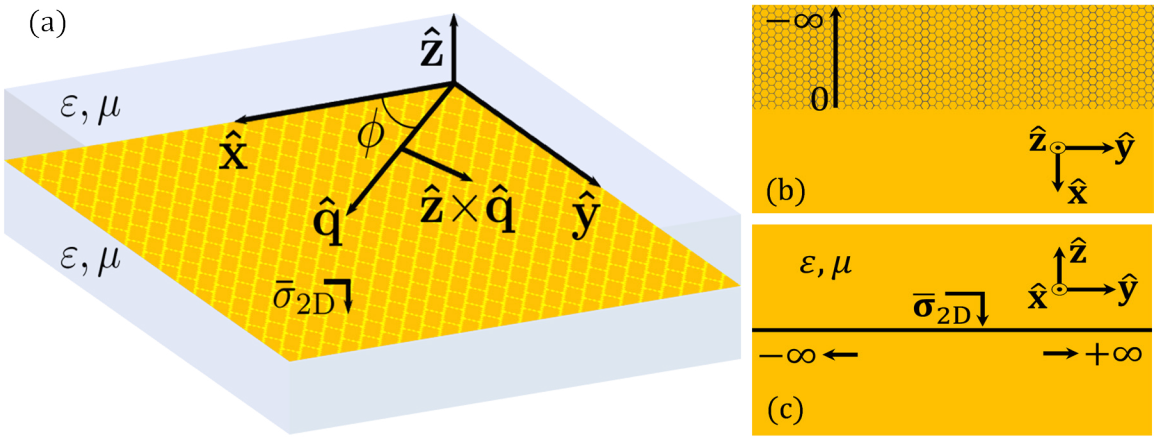

Figure 3-2: (a) Anisotropic two-dimensional material characterized by surface conductivity tensor $\bar{\sigma}_{2D}$, embedded in an isotropic medium characterized by relative permittivity ε and permeability μ. Quasi-TM SPP modes supported by the structure have a dominant magnetic field component parallel to $\hat{\mathbf{z}} \times \hat{\mathbf{q}}$, and propagate along the surface in the $\hat{\mathbf{q}}$ direction. The angle $\hat{\mathbf{q}}$ makes with $\hat{\mathbf{x}}$ is denoted ϕ. (b)-(c) Perspective views of the 2D material shown in (a) where an edge is introduced into the structure at $x = 0$, rendering the structure infinite along $\hat{\mathbf{y}}$ and semi-infinite along $\hat{\mathbf{x}}$.

in this frame is

$$\bar{\sigma}\left(\omega, \phi\right) = \mathbf{U}^{-1}\left(\phi\right) \cdot \bar{\sigma}_{s}\left(\omega\right) \cdot \mathbf{U}\left(\phi\right) \ , \tag{3.2}$$

where

$$\mathbf{U}\left(\phi\right) = \begin{pmatrix} \cos\left(\phi\right) & -\sin\left(\phi\right) \\ \sin\left(\phi\right) & \cos\left(\phi\right) \end{pmatrix} \ , \tag{3.3}$$

with ϕ denoting the angle of propagation (i.e., the angle $\mathbf{q}$ makes with $\hat{\mathbf{x}}$). Expanding the transformation in Eq. (3.2) results in

$$\bar{\sigma}\left(\omega, \phi\right) = \begin{pmatrix} \sigma_{\hat{\mathbf{q}}\hat{\mathbf{q}}}\left(\omega, \phi\right) & \sigma_{\hat{\mathbf{q}}(\hat{\mathbf{z}}\times\hat{\mathbf{q}})}\left(\omega, \phi\right) \\ \sigma_{(\hat{\mathbf{z}}\times\hat{\mathbf{q}})\hat{\mathbf{q}}}\left(\omega, \phi\right) & \sigma_{(\hat{\mathbf{z}}\times\hat{\mathbf{q}})(\hat{\mathbf{z}}\times\hat{\mathbf{q}})}\left(\omega, \phi\right) \end{pmatrix} \ , \tag{3.4}$$

where

$$\sigma_{\hat{\mathbf{q}}\hat{\mathbf{q}}} = \sigma_{\hat{\mathbf{x}}\hat{\mathbf{x}}}(\omega)\cos^2(\phi) + \sigma_{\hat{\mathbf{y}}\hat{\mathbf{y}}}(\omega)\sin^2(\phi) \ , \tag{3.5}$$

$$\sigma_{\hat{\mathbf{q}}(\hat{\mathbf{z}}\times\hat{\mathbf{q}})} = \sigma_{\hat{\mathbf{x}}\hat{\mathbf{y}}}(\omega) + \delta\sigma_s(\omega)\cos(\phi)\sin(\phi) \ , \tag{3.6}$$

$$\sigma_{(\hat{\mathbf{z}}\times\hat{\mathbf{q}})\hat{\mathbf{q}}} = -\sigma_{\hat{\mathbf{x}}\hat{\mathbf{y}}}(\omega) + \delta\sigma_s(\omega)\cos(\phi)\sin(\phi) \ , \tag{3.7}$$

$$\sigma_{(\hat{\mathbf{z}}\times\hat{\mathbf{q}})(\hat{\mathbf{z}}\times\hat{\mathbf{q}})} = \sigma_{\hat{\mathbf{x}}\hat{\mathbf{x}}}(\omega)\sin^2(\phi) + \sigma_{\hat{\mathbf{y}}\hat{\mathbf{y}}}(\omega)\cos^2(\phi) \ , \tag{3.8}$$

and $\delta\sigma_s = \sigma_{\hat{\mathbf{y}}\hat{\mathbf{y}}} - \sigma_{\hat{\mathbf{x}}\hat{\mathbf{x}}}$. Assuming low loss, the conductivity elements in the standard basis are of the form $\sigma_{\alpha\alpha} = i\mathrm{Im}\{\sigma_{\alpha\alpha}\} + \epsilon_{\alpha\alpha}$ and $\sigma_{\alpha\beta} = \mathrm{Re}\{\sigma_{\alpha\beta}\} + i\epsilon_{\alpha\beta}$ for $\alpha, \beta \in \{\hat{\mathbf{x}}, \hat{\mathbf{y}}\}$ $(\alpha \neq \beta)$ such that $|\mathrm{Im}(\sigma_{\alpha\alpha})| \gg |\epsilon_{\alpha\alpha}|$ and $|\mathrm{Re}(\sigma_{\alpha\beta})| \gg |\epsilon_{\alpha\beta}|$. Both $\epsilon_{\alpha\alpha}$ and $\epsilon_{\alpha\beta}$ are real valued with $\epsilon_{\alpha\alpha} > 0$ while the sign of $\epsilon_{\alpha\beta}$ is determined with respect to an arbitrary axis along which time reversal symmetry is broken.

3.3 Dispersion of bulk SPP modes

From Eqs. (1.77)-(1.78), the tangential boundary conditions on the electric $\mathbf{E}(\mathbf{q}, z)$ and magnetic fields $\mathbf{H}(\mathbf{q}, z)$ at the interface $(z = 0)$ in the spatial Fourier transform domain with respect to the spatial coordinates x and y are

$$\hat{\mathbf{z}} \times \left[\mathbf{E}\left(\mathbf{q}, 0^+\right) - \mathbf{E}\left(\mathbf{q}, 0^-\right)\right] = \mathbf{0} \ , \tag{3.9}$$

$$\hat{\mathbf{z}} \times \left[\mathbf{H}\left(\mathbf{q}, 0^+\right) - \mathbf{H}\left(\mathbf{q}, 0^-\right)\right] = \bar{\sigma} \cdot \mathbf{E}\left(\mathbf{q}, 0^+\right) \ , \tag{3.10}$$

and lead to the recovery of the SPP dispersion relation

$$\det\left(2\bar{\mathbf{Y}} - \bar{\sigma}\right) = 0 \ , \tag{3.11}$$

where $\mathbf{q}$ is preserved across the interface and $\bar{\mathbf{Y}}$ is defined in the appendix, Sec. A.2. Explicit solutions to Eq. (3.11) for the SPP wavenumber in terms of the propagation angle

exist and can be written in the form

$$q^{\pm} = k\sqrt{R^{\pm} + iI^{\pm}} \ , \tag{3.12}$$

where $k = \omega\sqrt{\varepsilon\mu}$, $R^{\pm}$ and $I^{\pm}$ denote the real and imaginary parts of the argument of the square root respectively, and the $\pm$ distinguishes between the two solutions corresponding to QTE and QTM SPP modes. The usual branch of the square root is assumed in which $\mathrm{Re}\{q^{\pm}\} > 0$, and it is important to note that $\mathrm{sgn}\left(\mathrm{Im}\left\{q^{\pm}\right\}\right)$ is equal to that of $I^{\pm}$). It can be shown that

$$R^{\pm} = 1 + \frac{2\left|\Delta^{\pm}\right|}{\eta^2\left|\sigma_{\hat{\mathbf{q}}\hat{\mathbf{q}}}\right|^2}\cos\left(2\theta + \gamma^{\pm}\right) \ , \tag{3.13}$$

$$I^{\pm} = \frac{2\left|\Delta^{\pm}\right|}{\eta^2\left|\sigma_{\hat{\mathbf{q}}\hat{\mathbf{q}}}\right|^2}\sin\left(2\theta + \gamma^{\pm}\right) \ , \tag{3.14}$$

where

$$\Delta^{\pm} = s^4 - 2s_d^2 \mp s^2\sqrt{s^4 - 4s_d^2} \ , \tag{3.15}$$

with $s^2 = 1 + \eta^2 \mathrm{det}\left(\bar{\sigma}\right)/4$, $s_d^2 = \eta^2\sigma_{\hat{\mathbf{q}}\hat{\mathbf{q}}}\sigma_{(\hat{\mathbf{z}}\times\hat{\mathbf{q}})(\hat{\mathbf{z}}\times\hat{\mathbf{q}})}/4$, and $\eta^2 = \mu/\varepsilon$. The angles $\theta, \gamma^{\pm} \in [-\pi, \pi]$ are defined as

$$\theta = \mathrm{sgn}\left(\mathrm{Im}\left\{\sigma_{\hat{\mathbf{q}}\hat{\mathbf{q}}}\right\}\right)\tan^{-1}\left(\frac{\mathrm{Re}\left\{\sigma_{\hat{\mathbf{q}}\hat{\mathbf{q}}}\right\}}{\left|\mathrm{Im}\left\{\sigma_{\hat{\mathbf{q}}\hat{\mathbf{q}}}\right\}\right|}\right) \ , \tag{3.16}$$

$$\gamma^{\pm} = \tan^{-1}\left(\frac{\mathrm{Im}\left\{\Delta^{\pm}\right\}}{\mathrm{Re}\left\{\Delta^{\pm}\right\}}\right) \ . \tag{3.17}$$

In most cases, QTE SPP modes are fast propagating with small wavenumber (i.e., $q^{+} \simeq k$). As a result, these modes tend to leak rapidly into the surrounding environment and are loosely confined to the interface. Therefore, these modes are of little importance and are not considered in the following analysis. In contrast, QTM modes tend to be slow propagating with large wavenumber (i.e., $q^{-} \gtrsim k$) and tightly confined to the interface [93]

which is ideal. It is straightforward to show, in the isotropic case, that

$$\left|\frac{\mathrm{Im}\left\{\Delta^{-}\right\}}{\mathrm{Re}\left\{\Delta^{-}\right\}}\right| < \left|\frac{\mathrm{Re}\left\{\sigma_{\hat{\mathbf{q}}\hat{\mathbf{q}}}\right\}}{\mathrm{Im}\left\{\sigma_{\hat{\mathbf{q}}\hat{\mathbf{q}}}\right\}}\right| \ , \tag{3.18}$$

and although difficult to formally prove, it is reasonable to assume Eq. (3.18) also holds in the anisotropic case, as numerical tests have confirmed. We then find

$$\left|\gamma^{-}\right| = \tan^{-1}\left|\frac{\mathrm{Im}\left\{\Delta^{-}\right\}}{\mathrm{Re}\left\{\Delta^{-}\right\}}\right| < \tan^{-1}\left|\frac{\mathrm{Re}\left\{\sigma_{\hat{\mathbf{q}}\hat{\mathbf{q}}}\right\}}{\mathrm{Im}\left\{\sigma_{\hat{\mathbf{q}}\hat{\mathbf{q}}}\right\}}\right| = |\theta| \ , \tag{3.19}$$

indicating that $2\theta + \gamma^{-}$ and 2θ share the same quadrant. As a result, one is justified in writing Eq. (3.14) in the form

$$I^{-} = \mathrm{sgn}\left(\mathrm{Im}\left\{\sigma_{\hat{\mathbf{q}}\hat{\mathbf{q}}}\right\}\right)\left[\frac{2\left|\Delta^{-}\right|}{\eta^{2}\left|\sigma_{\hat{\mathbf{q}}\hat{\mathbf{q}}}\right|^{2}}\sin\left|2\theta+\gamma^{-}\right|\right] \ , \tag{3.20}$$

where the term in brackets $[\cdot]$ is positive, making it clear that $\mathrm{sgn}\left(\mathrm{Im}\left\{\sigma_{\hat{\mathbf{q}}\hat{\mathbf{q}}}\right\}\right)$ controls the sign of I^{-} and ultimately $\mathrm{Im}\left\{q^{-}\right\}$.

Outward propagating QTM SPP modes along a particular direction in the plane of the interface are required to have $\mathrm{Im}\left\{q\right\} > 0$ in order to satisfy the Sommerfeld radiation condition. This condition is satisfied when $I^{-} > 0$ and therefore, $\mathrm{Im}\left\{\sigma_{\hat{\mathbf{q}}\hat{\mathbf{q}}}\right\} > 0$. Therefore, we characterize the conductivity as inductive according to $\mathrm{Im}\left\{\sigma_{\hat{\mathbf{q}}\hat{\mathbf{q}}}\right\} > 0$, which remains valid in the isotropic limit.

In summary, a local dispersive, anisotropic two-dimensional material supports QTM SPP modes when the effective conductivity experienced by the wave along the propagation direction $\sigma_{\hat{\mathbf{q}}\hat{\mathbf{q}}}\left(\omega,\phi\right)$ is inductive, with a positive imaginary part. In the limiting cases $\phi = 2n\pi$ and $\phi = n\pi + \pi/2$ for $n \in \{0,1,2,\dots\}$, we find $\sigma_{\hat{\mathbf{q}}\hat{\mathbf{q}}} = \sigma_{\hat{\mathbf{x}}\hat{\mathbf{x}}}$ and $\sigma_{\hat{\mathbf{q}}\hat{\mathbf{q}}} = \sigma_{\hat{\mathbf{y}}\hat{\mathbf{y}}}$ respectively; the other diagonal element is effectively immaterial in these limits. As a result, predicting the spectral location of bandgaps in the QTM SPP dispersion is straightforward. Lastly, we note that in most cases, natural 2d/quasi-2D materials are supported by a substrate of some kind. In this case, closed form solutions to the dispersion relation, Eq.

(3.11), no longer exist, and the above analysis no-longer rigorously applies as the material properties above and below the material would differ. However, as long as the substrate plays a negligible role in guiding the SPP, the above analysis is still useful.

3.3.1 Graphene in an external static magnetic field

In this example, we consider graphene biased with a perpendicular external magnetic field $\mathbf{B} = \hat{\mathbf{z}} B_0$ [T]. The conductivity tensor in the standard basis is defined in Eq. (3.1) with $\sigma_{\hat{\mathbf{x}}\hat{\mathbf{x}}} = \sigma_{\hat{\mathbf{y}}\hat{\mathbf{y}}} = \sigma_d$ and $\sigma_{\hat{\mathbf{x}}\hat{\mathbf{y}}} = -\sigma_{\hat{\mathbf{y}}\hat{\mathbf{x}}} = \sigma_o$, where $\sigma_{d,o} = \sigma_{d,o}^{\text{intra}} + \sigma_{d,o}^{\text{inter}}$. The intra- and inter-band contributions are written as a discrete summation over Landau levels [94]

$$\sigma_d^{\text{inter/intra}} = \frac{\hbar\tilde{\omega}}{i} \frac{e^2 E_1^2}{2\pi\hbar} \sum_{n=0}^{\infty} \frac{1}{M_n^{\pm}} \frac{N_{n+1}^{-} \pm N_n^{-}}{M_n^{\pm} M_n^{\pm} - \hbar^2\tilde{\omega}^2} \ , \tag{3.21}$$

$$\sigma_o^{\text{inter/intra}} = \text{sgn}\left(B_0\right) \frac{e^2 E_1^2}{2\pi\hbar} \sum_{n=0}^{\infty} \frac{N_{n+1}^{+} - N_n^{+}}{M_n^{\pm} M_n^{\pm} - \hbar^2\tilde{\omega}^2} \ , \tag{3.22}$$

where $N_n^{\pm} = n_F\left(-E_n\right) \pm n_F\left(E_n\right)$ and $M_n^{\pm} = E_{n+1} \pm E_n$ with $\tilde{\omega} = \omega + 2i\Gamma$, $E_n = v_F\sqrt{2\hbar n \left|eB_0\right|}$, and $n_F\left(E\right) = \left\{\exp\left[\left(E - \mu_c\right)/k_B T\right] + 1\right\}^{-1}$ is the Fermi-Dirac distribution function. Parameters $\{\omega, \Gamma, \mu_c, v_F, e, T, \hbar, k_B\}$ denote the excitation frequency, scattering rate, chemical potential, Fermi velocity $\simeq 10^6$ m/s, fundamental charge, temperature, Planck's reduced constant, and Boltzmann constant respectively. One additional parameter worth introducing is the magnetic length $l_B = \sqrt{\hbar/\left|eB_0\right|}$. This quantity places a bound on q in the sense that for $q > 1/l_B$ a non-local model for the conductivity is required [88]. It should also be noted that for relatively large magnetic field values (i.e., $B_0 > 0.1$ T), the infinite sums in Eqs. (3.21)-(3.22) converge rather quickly, making it sufficient to include only a few terms. This yields the correct result for frequencies up to the first few landau levels, however, additional terms are necessary at higher frequencies to obtain the correct resonance behavior.

The QTM dispersion and associated equi-frequency dispersion contours are shown in Figs. 3-3(a) and 3-3(b) respectively, while the imaginary part of $\sigma_{\hat{\mathbf{q}}\hat{\mathbf{q}}}$ is shown in Fig. 3-3(c). Isotropy in the diagonal elements results in isotropic equi-frequency contours as the

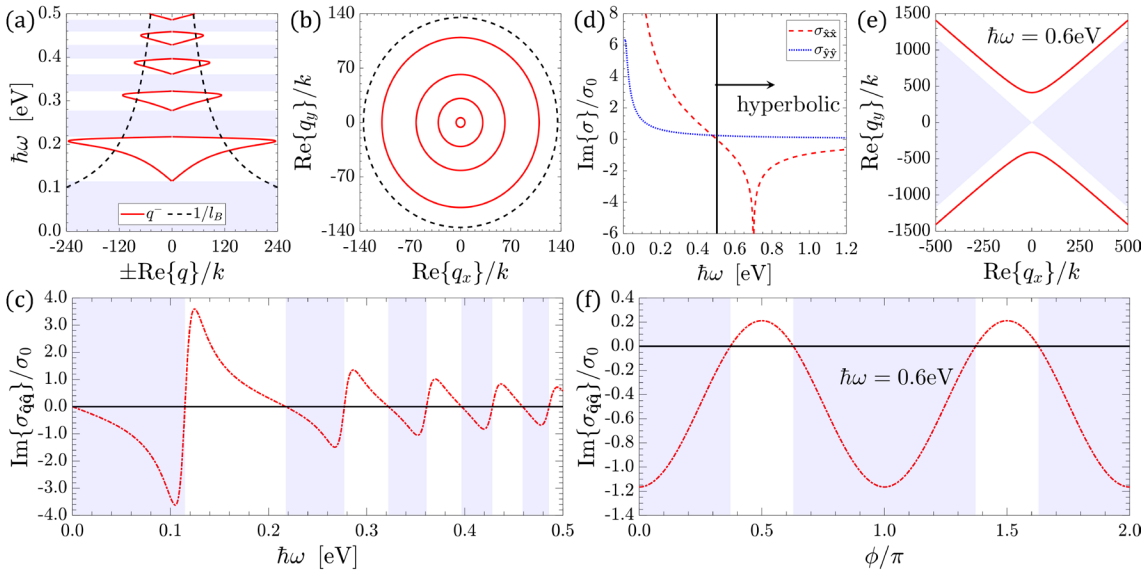

Figure 3-3: (a) Quasi-TM SPP dispersion (solid red) with bandgaps shaded. For $\mathrm{Re}\{q\}/k$ that falls within the dashed black lines corresponding to $\mathrm{Re}\{q\} = 1/l_B$, a local model for the conductivity tensor is valid. (b) Isotropic equi-frequency contours increasing with radius for the respective energies $\{0.12, 0.14, 0.16, 0.18\}$ eV. (c) Behavior of $\mathrm{Im}\{\sigma_{\hat{\mathbf{q}}\hat{\mathbf{q}}}\}$ shows how the spectral regions in which the sign is negative correspond to the shaded bandgap regions in (a). Material parameters used in the conductivity model described in Eqs. (3.21)-(3.22) are $\hbar\Gamma = 0.005$eV, $\mu_c = 0.3E_1 \simeq 0.03$eV, $B_0 = 10$T, and $T = 40$K. (d) Conductivity tensor elements represented in the standard basis for a black phosphorous thin film. The hyperbolic regime in which $\mathrm{Im}\{\sigma_{xx}\}\mathrm{Im}\{\sigma_{yy}\} < 0$ is located to the right of the vertical black line. (e) The hyperbolic equi-frequency dispersion contour for $\hbar\omega = 0.2$eV. Bandgaps in the equi-frequency contours (shaded) are determined by $\mathrm{Im}\{\sigma_{qq}\} < 0$ shown in (f). Material parameters used in the conductivity model described in Eq. (3.23) are $\hbar\Gamma = 0.005$eV, $n = 5 \times 10^{13}\mathrm{cm}^{-2}$, $m_x^* = 0.15m_0$, $m_y^* = 1.2m_0$, $\hbar\omega_x = 0.7$eV, and $\sigma_x = 3.5\sigma_0$, where m_0 denotes the free electron rest mass and $\sigma_0 = e^2/4\hbar$.

dependence on ϕ drops out of $\sigma_{\hat{\mathbf{q}}\hat{\mathbf{q}}}$. Bandgaps that occur in the dispersion clearly correspond to $\mathrm{Im}\{\sigma_{\hat{\mathbf{q}}\hat{\mathbf{q}}}\} < 0$, indicated by the blue shaded regions.

3.3.2 Hyperbolic black phosphorous

Next, we consider an approximate model for the conductivity of multilayer black phosphorous thin films [67, 68] where anisotropy arises as a consequence of the in-plane crystallographic directions having different symmetries. In the hyperbolic regime, the imaginary parts of $\sigma_{\hat{\mathbf{x}}\hat{\mathbf{x}}}$ and $\sigma_{\hat{\mathbf{y}}\hat{\mathbf{y}}}$ are of opposite sign, in which case the sign of the imaginary part of $\sigma_{\hat{\mathbf{q}}\hat{\mathbf{q}}}$ may vary depending on propagation angle and excitation frequency. In what follows, we restrict our consideration to bandgap dependence on propagation angle.

At sufficiently low frequency, intraband transitions dominate the material response and

lead to a Drude type contribution to the conductivity of the form $\sigma_{\alpha\alpha}^{\text{intra}} = i\Omega_{\alpha\alpha}/\tilde{\omega}$ for $\alpha \in \{\hat{\mathbf{x}}, \hat{\mathbf{y}}\}$, where $\tilde{\omega} = \omega + 2i\Gamma$ and $\Omega_{\alpha\alpha} = e^2 |n| / m_\alpha^*$ denotes the drude weight. The parameters $\{\omega, \Gamma, n, m_\alpha^*, e\}$ denote the excitation frequency, scattering rate, charge carrier density, fundamental charge, and effective mass respectively. At higher frequencies, inter-band transitions dominate. However, in the case of multilayer black phosphorous, interband transitions are negligible along one of the crystallographic directions which we conveniently take to be $\hat{\mathbf{y}}$. Thus, $\sigma_{\hat{\mathbf{y}}\hat{\mathbf{y}}}$ has only an intraband contribution while $\sigma_{\hat{\mathbf{x}}\hat{\mathbf{x}}}$ has both intra- and inter-band contributions. We introduce the inter-band contribution phonologically by modeling the absorption (real part) as a unit step and obtain the imaginary part from the Kramers-Kronig relations. In total, we have [95]

$$\sigma_{\hat{\mathbf{x}}\hat{\mathbf{x}}}^{\text{inter}} = \sigma_{\hat{\mathbf{x}}} \left[\Theta\left(\omega - \omega_{\hat{\mathbf{x}}}\right) + \frac{i}{\pi} \ln \left| \frac{\omega - \omega_{\hat{\mathbf{x}}}}{\omega + \omega_{\hat{\mathbf{x}}}} \right| \right] , \tag{3.23}$$

where $\omega_{\hat{\mathbf{x}}}$ denotes the onset frequency of inter-band transitions and $\sigma_{\hat{\mathbf{x}}}$ is an amplitude coefficient.

Figure 3-3(d) shows how the imaginary parts of the conductivity elements in the standard basis vary with respect to frequency. The solid black vertical line separates the elliptic and hyperbolic regimes. Parameters used in the conductivity model correspond to a 20nm thick Black Phosphorus film [68], doped with a 0.2eV chemical potential defined as the energy difference between Fermi level and first conduction subband. For $\hbar\omega = 0.6$ eV, the equi-frequency dispersion contour (EFC) is shown in Fig. 3-3(e), and the imaginary part of $\sigma_{\hat{\mathbf{q}}\hat{\mathbf{q}}}$ as propagation angle varies is shown in Fig. 3-3(f). Bandgaps in the EFC are shaded and agree with $\text{Im}\{\sigma_{\hat{\mathbf{q}}\hat{\mathbf{q}}}\} < 0$.

3.4 A CrI_3-graphene van der Waals heterostructure

Graphite consists of parallel atomic layers of carbon atoms, the layers being weakly bound together by van der Waals (vdW) forces. As such, graphite is easily cleaved to form few layer materials, or even monolayers (graphene). Since its experimental isolation in 2004

[96], graphene has been an object of considerable study for both scientific and industrial investigators. Graphene's most notable feature is its atomic hexagonal lattice, which results in linear electronic dispersion and the presence of Dirac points at the Fermi level. As a result, electrons behave as massless particles in the vicinity of the Dirac point, leading to extraordinary electrical and mechanical properties [97].

Bulk chromium triiodide, CrI_3, is also a layered vdW material that can be easily cleaved, and is relatively stable in ambient conditions [98]. Bulk CrI_3 is a ferromagnetic (FM) insulator with a relatively high Curie temperature of $T_c = 61$ K [98]. The 2D/monolayer form of CrI_3 consists of Cr^{3+} ions and I^- ions that form edge-sharing octahedra arranged in a hexagonal honeycomb lattice with an approximate thickness of 0.6 nm. Like its bulk form, monolayer CrI_3 is also a FM insulator, with an out-of-plane easy axis and somewhat reduced T_c of 45 K [99].

The controlled growth/deposition of 2D materials can lead to van der Waals heterostructures that result in exceedingly thin structures with enhanced functionality. Here, we exploit the proximity exchange between a 2D ferromagnet and graphene. In its monolayer form, CrI_3 exhibits massive local Cr magnetic moments of $3\mu_B$, which can induce large exchange splittings in adjacent layers of a heterostructure. Since 2D CrI_3 has a hexagonal structure, it is well lattice-matched with graphene. Magnetic order in CrI_3 has been studied experimentally in [100–104], and in other 2D magnets, such as $MnSe_2$ [105,106] and $CrGeTe_3$ [107,108]. In all cases, these 2D magnets have out of the plane magnetization. In some cases, magnetic effects can be controlled via electrostatic gating [103, 104], or strain [109, 110].

Enormous pseudo-magnetic fields (on the order of hundreds of Tesla) and associated pseudo-Landau levels (LLs) have been predicted in strained systems [111]. Such fields do not break time-reversal (TR) symmetry, and therefore, lead to reciprocal behavior. Importantly, the exchanged-induced fields described here do break TR. The effective Hamiltonians for both an external magnetic field and a ferro-/antiferro-magnetic system contain terms that explicitly couple to the spin that are not invariant under time reversal. In contrast, the pseudo-magnetic fields in strained graphene couple to charge only, and hence preserve

time-reversal symmetry. Exchange interactions in similar vdW heterostructures have been considered, e.g., $Cr_2Ge_2Te_6$-graphene [112], where equilibrium exchange splittings are calculated to be approximately 5 meV, and EuS-graphene [113]. A Chern insulating state can be realized in graphene in proximity to CrI_3, via the magnetic exchange field and Rashba spin-orbit coupling (SOC) [110,114]. However, to achieve this, the heterostructure needs to be compressed from its equilibrium state which increases the effective field [114].

In Ref. [25], first-principles density functional theory (DFT) calculations are used to show that the proximity exchange in graphene due to monolayer CrI_3 can result in an enormous exchange field, and the conductivity of graphene in the presence of the CrI_3 exchange field is investigated. In addition, the behavior of bulk and nonreciprocal edge surface-plasmon polaritons (SPPs) is studied in the far-infrared regime. Those results are then compared with the conductivity and SPP properties of graphene in an external magnetic field, and significant differences are found in the two cases.

The principal findings of Ref. [25] summarized in this section are: (1) the equilibrium (minimum energy) separation between the CrI_3 and graphene is approximately 3.75 Å, at which point the exchange splitting is 21 meV, corresponding to an effective exchange field of 100 T and a chemical potential of $\mu = -0.3$ eV, which self-biases the graphene. Referring to graphene's conductivity in the CrI_3-graphene heterostructure, (2) Landau levels, which are the most prominent feature of the graphene conductivity in a strong external field, are absent in the case of the exchange field. (3) In the far-infrared, the intraband conductivity is dominant, with diagonal element values that are approximately the same as isolated graphene with no applied magnetic bias and $\mu = -0.3$ eV, whereas the off-diagonal elements are similar in magnitude to those in the external bias case. (4) Because of the large diagonal conductivity response compared to having an external bias (in which case most of the Drude weight is transferred to the Landau levels), the resulting non-reciprocity due to the exchange field is considerably less than for an external magnetic field of the same strength. For smaller separation (achievable through, e.g., strain), a unidirectional edge SPP can be found.

The section is organized as follows. In Sec. 3.4.2 the exchange-field-induced graphene

conductivity is discussed, and compared with that of isolated graphene in the presence and absence of an external magnetic bias. Bulk and edge surface plasmons are then considered in Sec. 3.4.3. The edge SPPs for the exchange field are slightly non-reciprocal for the equilibrium separation, whereas for the external bias case they are highly nonreciprocal (unidirectional), tightly-confined, long-lasting, and robust to material discontinuities. In the appendix, a derivation of the edge SPP dispersion is provided. The suppressed time harmonic dependence is $e^{-i\omega t}$.

3.4.1 Electronic band structure of graphene in an exchange field

Density functional calculations for graphene on CrI_3 have been reported previously, [110], with an emphasis on the topological aspects of the compressed system. Here the focus is on the effect of the induced exchange field on the graphene electronic structure, and the implications for the calculation of optical properties discussed later in Sec. 3.4.2; detailed first-principles calculations of the optical properties of the CrI_3 itself have also been reported previously [115]. To model the graphene-CrI_3 heterostructure, we consider the commensurate supercell outlined in black in Fig. 3-4(a), which consists of 5×5 (unit cell) graphene on a free-standing $\sqrt{3} \times \sqrt{3}$ CrI_3 monolayer. The two materials are well lattice-matched, having only a $\sim$1% lattice mismatch. In addition, the following results are only very weakly dependent on the horizontal registry between the two since graphene and CrI_3 are both layered van der Waals materials. The supercell Brillouin zone of the heterostructure, which is a factor of 25 (3) times smaller than that of isolated graphene (CrI_3), is shown in Fig. 3-4(b), with the first Brillouin zone shaded yellow. The interatomic separation between graphene and CrI_3 is varied between 2.5 and 4.5 Å, as indicated in the 2D perspective view of the heterostructure, shown in Fig. 3-4(c).

Each ferromagnetically coupled Chromium (Cr) atom in the CrI_3 compound has a magnetic moment of 3 μ_B, and the moments are calculated ($\sim$0.4 meV/atom) to be orientated perpendicular to the plane. The spin-polarized k-projected [116, 117] bands of graphene around the Dirac (K) point and of CrI_3 at the calculated equilibrium separation of 3.75 Å

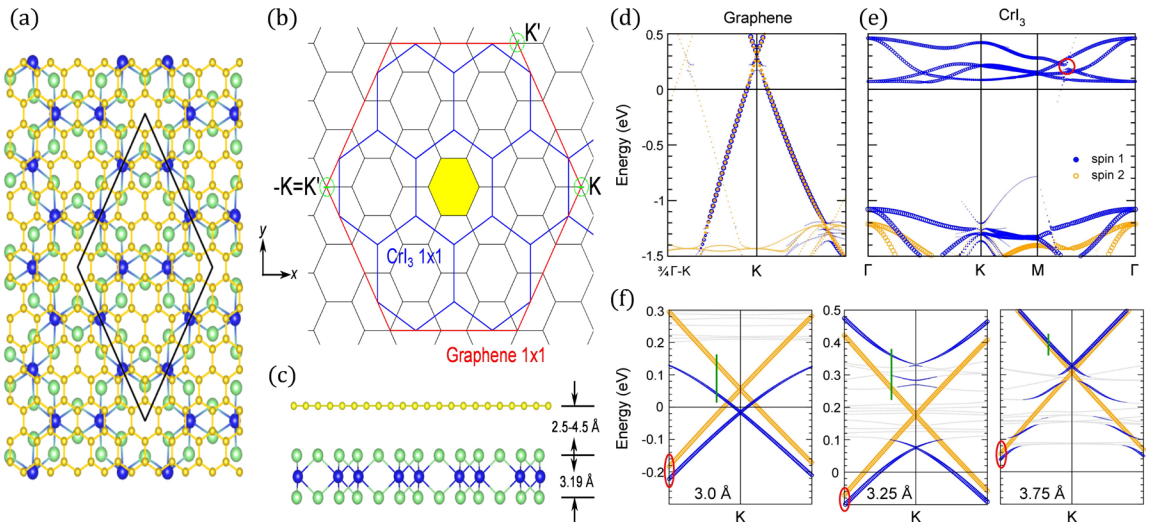

Figure 3-4: (a) Top and (c) side views of the CrI_3-graphene heterostructure at the atomic level (Carbon, C: yellow, Chromium, Cr: blue, Iodine, I: green), with the commensurate supercell outlined in black. (b) The Brillouin zones of the supercell (black; first Brillouin zone highlighted in yellow), CrI_3 (blue), and graphene (red). The green circles (and enclosed lines) denote the portion of momentum (k-) space where the graphene Dirac (K) points occur. (d)-(f) k-projected bands of the graphene-CrI_3 magnetic system. The Blue (orange) circles denote the majority (minority) electron spin states, while the size of the circles represent the relative weight of each state. (d) Graphene k-projected bands around the Dirac point ($\pm 1/4$) along Γ-K of the (1×1) Brillouin zone, and (b) CrI_3 k-projected bands along the high symmetry directions of the (1×1) structure, both for a graphene-CrI_3 separation of 3.75$\mathring{A}$. (c) Close-ups of the graphene k-projected bands within $\pm 1/40$ of K for different separations. The gray bands are ("folded" and CrI_3) bands with small weights. The green lines and red ovals show where the exchange splittings above and below the Dirac point, respectively, are measured.

are shown in Figs. 3-4(d) and (e), respectively. The range of separations discussed here may be experimentally accessible; the calculated pressures are 1.4, 3.7, and 13.5 GPa for interatomic separations of 3.25, 3.0, and 2.5 Å, respectively.

The top of the CrI_3 valence band and the lowest set of conduction bands are of majority spin (blue curves). The graphene Dirac point lies above the Fermi level (referenced at zero energy) in the conduction band of CrI_3, and opens up a gap in the CrI_3 conduction bands along Γ-M; the red circle in Fig. 3-4(b) highlights the location of the gap. The relative position of the graphene and CrI_3 bands with respect to the Fermi-level varies with interatomic separation. For separations of less than ∼3.2 Å, the graphene Dirac point is in the gap and then crosses into the CrI_3 conduction band as shown in Fig. 3-4(f). For all separations, the minority ("spin 2") graphene bands maintain their linear dispersions, even including spin-orbit interaction. The majority bands, on the other hand, interact

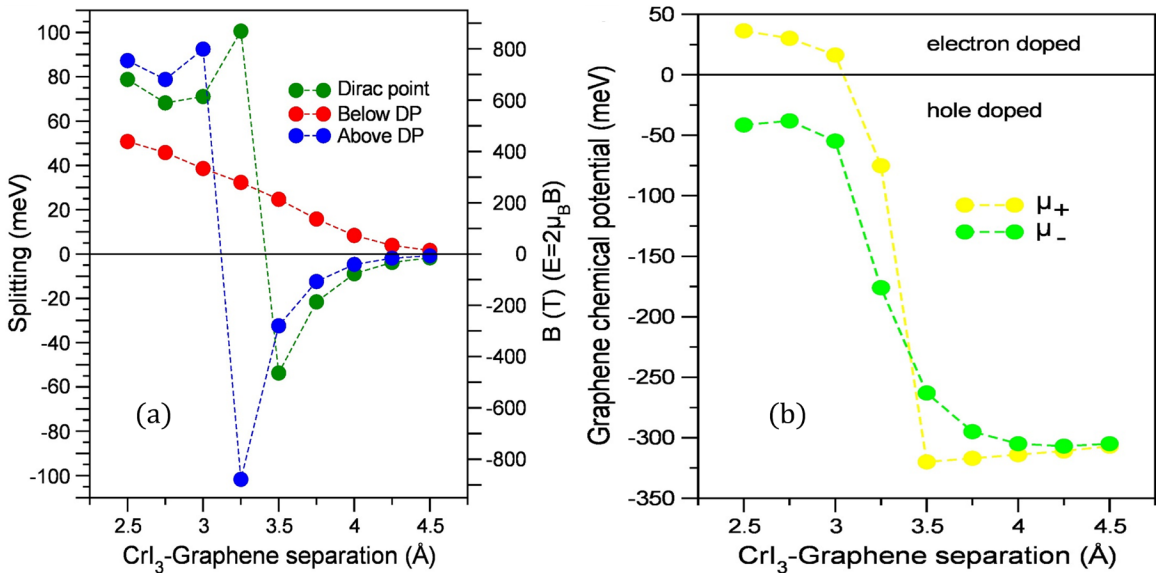

Figure 3-5: (a) Exchange (spin) splittings (meV) and effective magnetic bias field (T) experienced by the graphene spin states around K for different inter-atomic separations determined at the positions shown in Fig. 3-4(f), where above and below the Dirac point indicates the green line and red ovals respectively. (b) The chemical potentials of graphene for each spin, relative to the respective Dirac points.

and hybridize with the (majority spin) conduction band states of CrI_3, even for smaller separations where the Dirac point is in the gap. Importantly, because of the proximity of the graphene to the ferromagnetic CrI_3, there are induced exchange splittings of the graphene bands. For larger separations, the majority graphene bands that overlap the CrI_3 conduction bands are strongly modified, whereas the minority bands retain the characteristic graphene dispersions.

The calculated splittings of the Dirac point and the bands above (below), measured at the indicated positions in Fig. 3-4(f), are given in Fig. 3-5(a). These splittings are large compared to the Zeeman splittings induced by an external magnetic bias field; the effective fields are in the range of 100 T. When the Dirac point is in the gap, the exchange splittings are normal in the sense that the majority states are deeper in energy than the minority. However, the exchange splitting of the Dirac point and the bands above reverse as the Fermi level of the combined system moves into the conduction bands of CrI_3. Because of the exchange splitting and the relative positions of the bands, the graphene is effectively doped, which can be described by spin-dependent chemical potentials, $\mu_{\pm}$, as shown in Fig.

3-5(b). For smaller separations with the Dirac points in the gap, $\mu_{\pm}$ are approximately equal and of opposite sign, i.e., no net doping. The result is that for smaller separations when the Fermi level is in the gap, the position of the (minority) Dirac cone is closer to the Fermi level and determined by the size of the exchange splitting, while for larger separations, doping determines the position. For larger separations, including the equilibrium one, the graphene becomes hole doped with $\mu_{\pm} \sim -0.3$ eV.

For graphene in external magnetic bias fields and non-zero chemical potential, the intraband contributions to σ_{xx} dominate over interband ones in the far-infrared optical conductivity, and the formation of Landau levels provide an explanation of the Hall conductivity σ_{xy}. Although the *effective* fields due to the proximity-induced exchange splittings are large, these do not create Landau levels; the formations of the minibands in the majority (blue) bands seen in Fig. 3-4(f) are due to interactions and hybridization with the CrI_3 conduction bands. The Landau levels formed in graphene in the presence of external magnetic fields or strain-induced pseudomagnetic fields [118] are both more localized in energy and have their broad momentum distribution peaked around K. Similar to Landau levels, however, these minibands change the dispersion and hence will modify the optical transitions.

3.4.2 Optical conductivity

Figure 3-6(a),(b) shows the computed conductivity in the far-infrared and, for comparison, the conductivity computed (1) assuming isolated graphene in an external magnetic bias of 100T and hole doped with chemical potential $\mu = -0.3$ eV [119], (2) isolated unbiased graphene ($B = 0$ T) using the spin dependent chemical potentials $\mu^{\pm}$ plotted in Fig. 3-5(b) for separations $d \in \{2.5, 3.25, 3.75\}$ Å, and (3) the calculated CrI_3 conductivity [115], which is negligible at the considered frequencies. Figure 3-6(c) shows the off-diagonal element of conductivity verses the inter-atomic CrI_3-graphene separation, which is nondispersive (i.e., independent of frequency) in our calculation. For comparison, the off-diagonal conductivity (averaged over frequency from 0 to 5 THz) of graphene in an external bias is also shown where the effective fields "below the DP" plotted in Fig. 3-5(b) for each separation are

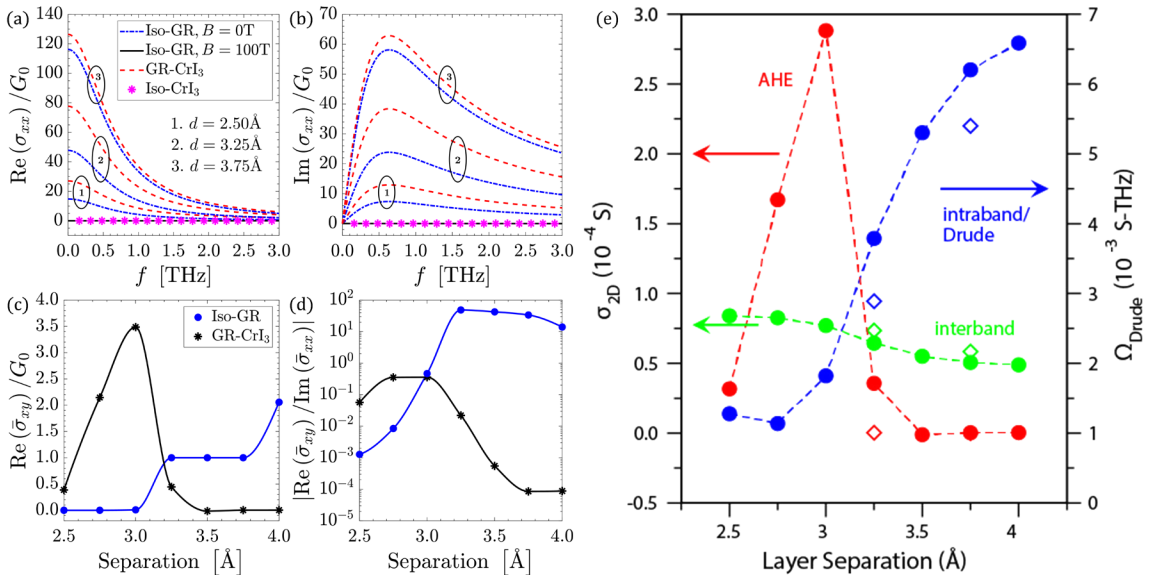

Figure 3-6: (a),(b) Two dimensional conductivity of graphene in the presence of the CrI_3 exchange field (GR-CrI_3) for inter-atomic separations $d \in \{2.5, 3.5, 3.75\}$Å. Also shown for comparison is the conductivity of isolated biased graphene (Iso-GR, $B = 100$T) computed assuming (1) $\mu_c^+ = \mu_c^- = -0.3$eV, and (2) isolated unbiased graphene ($B = 0$T) using the spin dependent chemical potentials that correspond to each of the aforementioned separations plotted in Fig. 3-5(b); in both the latter computations, $\Gamma = 2 \times 10^{12} s^{-1}$ and $T = 40$K. (c) Off-diagonal element vs. inter-atomic separation compared with isolated graphene in an external bias field where the value of effective bias "below the DP" plotted in Fig. 3-5(a) is assumed for each separation. (d) Off-diagonal element normalized by the diagonal element. In (c),(d) the overbar indicates frequency average, as explained in the text, and $G_0 = 2e^2/h$ is the conductance quantum. (e) Calculated contributions to the optical response: (blue) Drude intraband weights Ω_{Drude}, (red, green) anomalous Hall effect (AHE) $\sigma_{xy}^{\mathrm{2D}}$ and interband contributions $\sigma_{xx}^{\mathrm{2D}}$.

assumed. Figure 3-6(d) shows the off-diagonal conductivity (averaged over frequency) in the two cases (i.e., external bias and exchange field) normalized with respect to the averaged diagonal element (imaginary part) which serves as a measure of nonreciprocity in the system (i.e., the larger this ratio is, the more nonreciprocal the system is). Notably, non-reciprocity induced by the exchange field case is much weaker than for the external magnetic bias field for separations that exceed 3 Å.

The diagonal elements of the conductivity are dominated by the Drude intraband contribution $\sigma_{xx}^{\mathrm{2D-Drude}} = i\Omega/(\omega + 2i\Gamma)$ at the considered frequencies, with the Drude weights Ω plotted verses layer separation in Fig. 3-6(e), and resemble very closely the conductivity for isolated unbiased graphene, as shown in Figs. 3-6(a),(b), when accounting for the exchange-field induced spin-dependent values of chemical potential $\mu^{\pm}$. Because the Drude

weight is transferred to the Landau levels in the case of an external magnetic bias, the exchange field diagonal conductivity is several orders of magnitude larger than the equivalent external field conductivity (i.e., for the external bias case, the formation of Landau levels depresses the diagonal conductivity away from the Landau level), while forcing the off-diagonal elements to be nonzero due to cyclotron motion of the charge carriers. This results in relatively large ratios of the off-diagonal to diagonal elements for the external bias, in contrast to the exchange field case where the diagonal elements are relatively unaffected and hence the ratios are smaller as shown in Fig. 3-6(d).

Lastly, it is worth noting from Figs. 3-6(a),(b), that the CrI_3 conductivity is much smaller in magnitude than that of graphene. Since these effectively combine in parallel from an electromagnetic standpoint, we can ignore the presence of CrI_3 in the electromagnetic calculations. Further confirmation of this fact is obtained by computing the dispersion of a CrI_3-graphene layered system that includes both conductivities, as in Ref. [120].

3.4.3 Uni-directional quasi-static edge SPP modes

Assuming an out-of-plane magnetic bias, bulk SPPs on graphene have reciprocal, isotropic dispersion as shown in Fig. 3-3(a)-(b). Breaking inversion symmetry by introducing an edge, allows for plasmons with nonreciprocal dispersion [121]. Specifically, here we introduce a graphene half-space like the one depicted in Fig. 3-2(b),(c), and consider the unidirectional quasi-static SPP modes that may propagate on the edge. This is a well-studied problem [122, 123], and here we consider the exchange field and external bias cases.

Figure 3-7(a),(b) shows the bulk and edge dispersions for a graphene half-space due to the exchange fields corresponding to separations of (a) 3.0 Å, and (b) 3.75 Å. For the 3 Å separation, the right-going edge mode exists until approximately 3THz, above which the edge mode leaks into the bulk SPP (mathematically, it crosses onto an improper Riemann sheet through a branch point associated with the bulk mode wave number); the leaky mode (not shown) then approximately follows the bulk dispersion, with slightly lower wave number. In this case, the edge mode is unidirectional. However, for the equilibrium

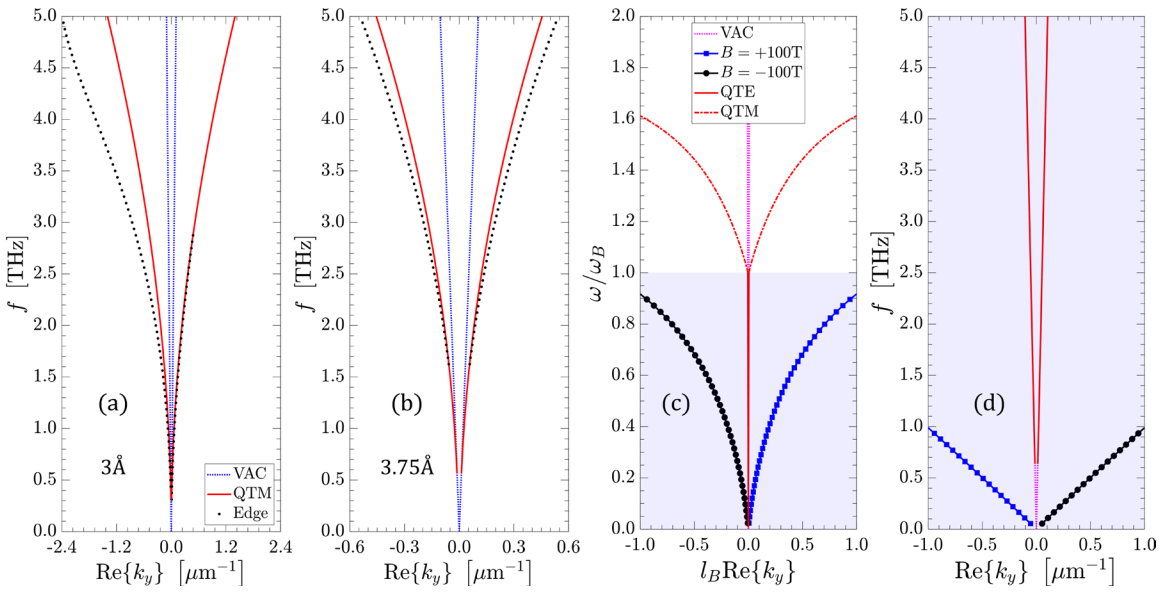

Figure 3-7: (a),(b) Bulk (solid red) and edge (dots) dispersion of quasi-TM graphene modes in an exchange field for two inter-atomic separations. (c),(d) Dispersion of bulk (dashed red) and edge (dots) quasi-TM modes and bulk quasi-TE modes (solid red) for graphene biased with an external magnetic field. The shaded region indicates the bulk bandgap, $\omega_B = 526.2 \times 10^{12}\text{s}^{-1}$ is the frequency of the first Landau level, $\mu = -0.3$eV, $T = 40$K, $\Gamma = 2 \times 10^{12}\text{s}^{-1}$, $B = 100$T, and $l_B = \sqrt{\hbar/eB} = 2.6$nm is the magnetic length. VAC indicates the dispersion of bulk modes in vacuum.

separation of 3.75 Å separation, the edge mode is essentially reciprocal.

The bulk and edge dispersions for graphene in an external magnetic bias field are shown in Fig. 3-7(c)-(d). The edge modes flip directions upon reversing the bias field. Although the results are computed assuming $B = 100$ T, due to the normalization, the dispersion is essentially independent of B for $|B| > 1$ T. For the external bias case, the Landau levels are given by

$$M_n = \sqrt{2nv_F^2 |eB|} \approx 36.3 \text{ meV} \times \sqrt{n\,|B|}\,, \tag{3.24}$$

where $v_F \simeq 10^6$ m/s is the graphene electron Fermi velocity.

For the exchange field, the bulk SPPs are not gapped as shown in Fig. 3-7(a)-(b), whereas for the external bias case, the bulk SPPs are strongly gapped as shown in Fig. 3-7(c)-(d), which is a result of the behavior of Im(σ). Since TM and quasi-TM modes require Im$\{\sigma\} > 0$ for a proper surface wave, gaps appear for Im$\{\sigma\} < 0$, which does not occur for the exchange case in the far-infrared, where the conductivity dispersion is Drude-like.

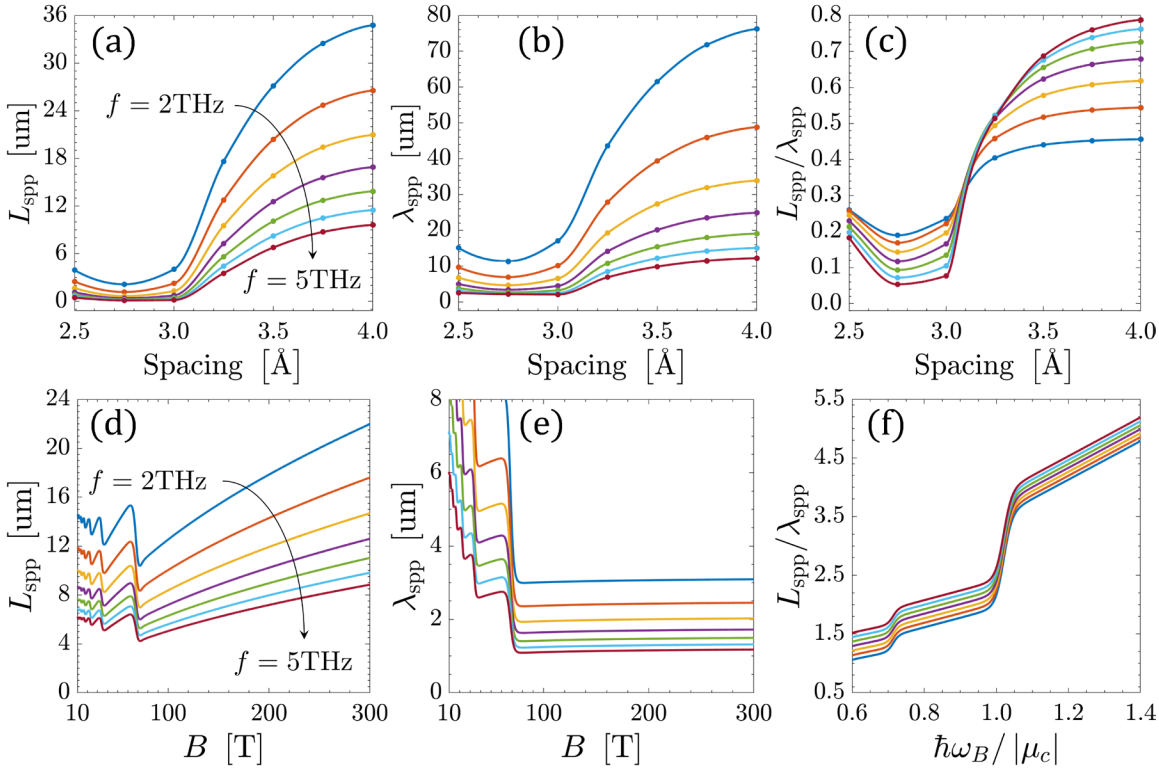

Figure 3-8: (a) Edge SPP propagation length associated with the left branch of Fig. 3-7(a), and (b) SPP wavelength on graphene in an exchange field as the inter-atomic separation varies. (d) Edge SPP propagation length and (e) SPP wavelength on graphene in an external bias, with $\mu_c = 0.05$eV, $T = 40$K, and $\Gamma = 2 \times 10^{12}\text{s}^{-1}$. In (d) and (e), the first LL occurs at $8.8\sqrt{|B|}$, well beyond the considered frequencies. (c),(f) Ratio of propagation length to wavelength for the CrI_3-graphene heterostructure and graphene biased with an external magnetic field.

In the external bias case, the formation of Landau levels causes this sign change at lower frequencies, resulting in the TM gap shown in Fig. 3-7(c).

Figure 3-8(a),(b) shows edge SPP propagation length and guided wavelength on the graphene layer as a function of inter-atomic separation. The SPP propagation length $1/2$ Im(k_y) generally increases with separation, and decreases with increasing frequency. A ratio of the propagation to wavelength is shown in Fig. 3-8(c). Because the SPP wavelength is so long, $L_{\text{SPP}}/\lambda_{\text{SPP}} \ll 1$, the SPP is not very useful. On the other hand, the corresponding edge SPP propagation length and wavelength on the graphene layer in an external field as a function of the external bias are shown in Fig. 3-8(d),(e). As the magnetic bias increases, the SPP propagation length increases, and $L_{\text{SPP}}/\lambda_{\text{SPP}} > 1$ (for large magnetic bias fields, $L_{\text{SPP}}/\lambda_{\text{SPP}} \approx$ 6-8). However, when $\hbar\omega_B/|\mu_c| < 1$, the SPP is not well

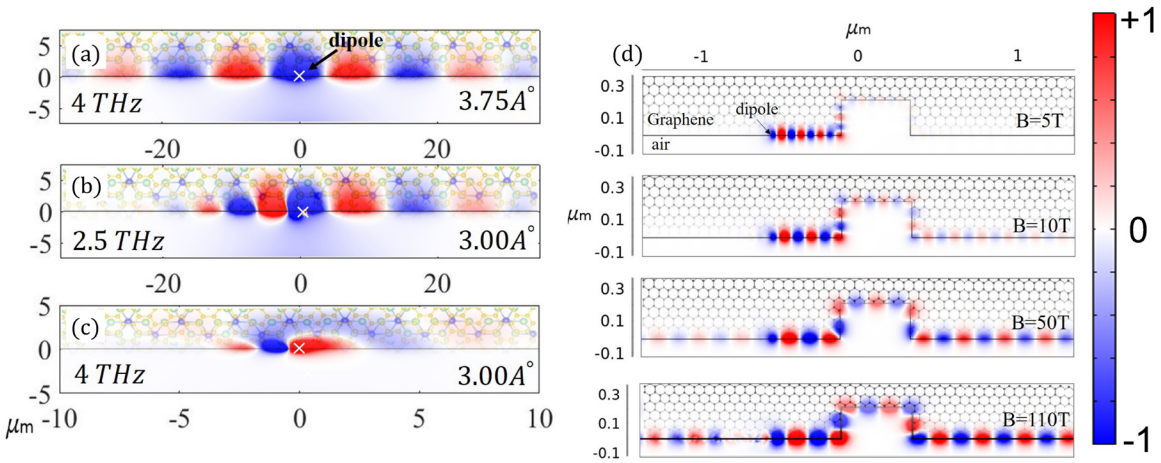

Figure 3-9: (a)-(c) Normalized field profile of an edge SPP launched by a dipole source polarized along $\hat{\mathbf{z}}$ (i.e., normal to the interface) for the exchange field magnetic bias corresponding to two CrI_3-graphene separations. (d) Normalized edge SPP field profile along the edge for several values of external magnetic bias, with $f = 13.87$THz, $\mu = 0.05$eV, $T = 40$K, and $\Gamma = 2 \times 10^{12}$ s^{-1}.

formed as shown in Fig. 3-8(f).

Figure 3-9(a)-(c) shows the edge SPP on the exchange-field biased graphene due to a dipole source in the vicinity of the graphene-vacuum edge, computed using the finite element method (FEM) in COMSOL for different operating frequencies and inter-atomic separations. In correspondence with the dispersion shown in Fig. 3-7(a)-(b), for the equilibrium separation of 3.75Å the SPP is essentially reciprocal, as it is at 2.5 THz for separation 3 Å. However, while for 3 Å and 4 THz, the SPP is unidirectional, $L_{\text{SPP}}/\lambda_{\text{SPP}}$ is small indicating that the SPP does not propagate well. In these simulations, an extremely fine adaptive physics based tetrahedral mesh, defined in the COMSOL software, was used. A surface current boundary condition, defined in terms of the surface conductivity tensor for graphene at the interface, was used. At the edges of the computational domain, a perfectly matched layer (PML) was applied to mimic an open and nonreflecting infinite domain.

In contrast to Fig. 3-9(a)-(c), Fig. 3-9(d) shows the edge SPP on externally-biased graphene due to a dipole source in the vicinity of the edge. The size of the discontinuity is on the order of λ_{SPP} (e.g., the length of the discontinuity contour in the second panel is $5\lambda_{\text{SPP}}$). As the magnetic bias increases, the SPP propagates further, in agreement with Fig. 3-8(d), while its wavelength increases. The edge SPP is clearly robust, and propagates

around the discontinuity. Although there appears to be a weak field to the left of the source, which is due to the imperfect boundary condition at the edge of the computational domain, and therefore nonphysical.

3.5 Summary

In this chapter, we used the conductivity of local, dispersive, anisotropic two-dimensional materials to predict the spectral location of bandgaps in the QTM SPP dispersion. These bandgaps were found to occur in regions of the spectrum where the imaginary part of the conductivity along the direction of propagation is negative (i.e., $\mathrm{Im}\{\sigma_{\hat{\mathbf{q}}\hat{\mathbf{q}}}\} < 0$) which remains valid in the isotropic limit. Conversely, we found that QTM SPP mode propagation is supported by inductive surfaces, which we characterized according to $\mathrm{Im}\{\sigma_{\hat{\mathbf{q}}\hat{\mathbf{q}}}\} > 0$. To demonstrate the proposed formalism, we provided two numerical examples of natural materials. In addition, we investigated exchange splitting in a monolayer chromium triiodide (CrI_3)–graphene van der Waals (vdW) heterostructure using density-functional theory where effective exchange fields of hundreds of Tesla are predicted. These enormous fields serve as the magnetic bias for the graphene layer. Graphene conductivity and SPP properties for the exchange field were considered, and compared with the external bias case. Since no Landau levels occur for the exchange field, the resulting non-reciprocity is found to be considerably weaker than for an equivalent external field bias (where strongly nonreciprocal electromagnetic edge modes that are tightly-confined, robust, and unidirectional are shown to exist).

Chapter 4

Topologically protected unidirectional surface magnon polaritons on a magnetized yttrium iron garnet

4.1 Introduction

Recently, a connection to momentum space topology has been made for plasmonic and ferrimagnetic continua biased with an external static magnetic field in the Voigt configuration [124–132], where bulk electromagnetic waves propagate in a direction perpendicular to the bias; see [8, 133–136] for comprehensive reviews. In this configuration, the field profile (i.e., polarization) of the wave may be decomposed into transverse-magnetic (TM) and -electric (TE) bulk modes, where transverse is defined with respect to the propagation direction. When the external bias is removed, these modes have the same dispersion (i.e., their wavenumbers are degenerate). However, once the bias is applied, the degeneracy is lifted, and a nontrivial bandgap forms in the TM/TE dispersion associated with plasmonic/ferrimagnetic continua over a frequency range wherein the effective permittiv-

ity/permeability experienced by the mode is negative. The nontrivial nature of the bandgap stems from the fact that time reversal (TR) symmetry in the material response is broken due to the applied bias, which results in a nonzero Berry curvature, described as a rotation in momentum space of the Berry connection, defined in terms of the material response tensor and TM/TE polarization [124, 125].

From a topological perspective, a bandgap in the dispersion of bulk modes is characterized by a topological invariant (usually normalized to be integer-valued) called the gap Chern number C_{gap}, defined in terms of the Berry curvature associated with modes that propagate below the bandgap [134]. The bandgap is classified as topologically trivial when $C_{\text{gap}} = 0$ (a trivial gap Chern number may also indicate the absence of a bandgap in the dispersion) and nontrivial when $C_{\text{gap}} \neq 0$. For biased plasmonic/ferrimagnetic continua, it has been shown that the TM/TE gap Chern number is $+1$ [21,124], therefore classifying the bandgap as nontrivial. Moreover, when interfaced with another material for which the bulk dispersion is topologically trivial, the difference between gap Chern numbers associated with each material, $\Delta C_{\text{gap}} = 1 - 0 = 1$, corresponds to the number of unidirectional surface wave modes that propagate in the nontrivial bulk bandgap. The correspondence between bulk and surface wave modes made via the gap Chern number, known as the bulk-edge correspondence principle, has been studied extensively for periodic photonic structures [137–142], and recently, the concept has been extended to continuous media [143–145].

The unidirectional nature of the surface wave modes grants them *topological protection* against reflection when encountering an abrupt change (e.g., a step) in the material interface [146–148]. And, because these modes propagate in the nontrivial bulk bandgap, they are immune to diffraction into the bulk. However, diffraction into the bulk of the interfaced trivial medium is possible if it lacks a common bandgap (e.g., air) [149]. While the aforementioned description in terms of momentum space topology is not really needed (i.e., classical terms concerning non-reciprocity and bandgaps already describe the phenomena [8,12]), the language of topology provides new insights into the underlying physics, and allows for instance, the potential engineering of photonic structures to achieve nontrivial

gap Chern numbers [138], which could be quite useful in designing nonreciprocal devices such as isolators [16–19], gyrators [20], circulators [150], and directional couplers [21, 22].

Although the existence of topologically protected surface wave modes supported by periodic photonic structures has been experimentally verified [151–155], here we verify, for the first time, the existence of a topologically protected surface magnon polariton (SMP) mode (i.e., a type of surface wave mode that arises from the coupling between the electromagnetic field and magnetic dipole polarization of a material) guided along the interface between a biased ferrimagnetic Yttrium Iron Garnet (YIG) continuum and air; see Fig. 4-1(a) for a schematic of the layered media structure under consideration. To demonstrate topological protection, we measure the S-parameters between two small loop magnetic dipole antennas that launch and receive the SMP, and show that transmission of the SMP remains largely unaffected when an abrupt change in the form of a step is present in the interface.

In Sec. 4.2, we provide a brief review of the theory already well established by the community that describes the topologically protected SMP, and provide numerical and simulated results that give qualitative and quantitative insight into the propagation characteristics. In Sec. 4.3, we provide an extensive overview of the experimental apparatus and a detailed analysis of the measurements.

4.2 Theory and simulation

4.2.1 Material response of a magnetized ferrite

Magnetic anisotropy in the material response of ceramic YIG ferrites is achieved by applying an external static (DC) magnetic bias field $\mathbf{H}_0$ which induces a DC magnetization $\mathbf{M}_0$ parallel to the bias. As a general consideration, the internal field of the YIG is reduced from the external field by a demagnetizing term which depends on the geometry and bias configuration. However, in the following analysis, we consider a thin square plate magnetized in the Voigt configuration [156], for which the demagnetizing term may be neglected [157]. The details of this contribution and its potential effect on the response are therefore omitted

(a)

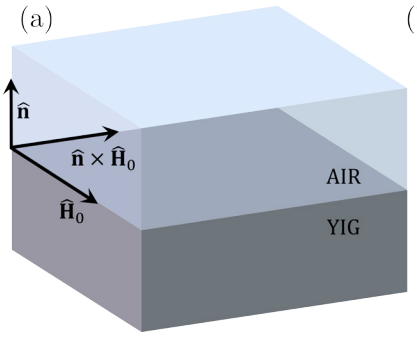

(b)

Saturation magnetization	$\mu_0 M_s$	1820 ±20% [Gs]
Effective Landé g-factor	g_{eff}	2.02
Resonance linewidth	ΔH	18 +20% [Oe]
Effective linewidth	ΔH_{eff}	3 [Oe]
Relative permittivity	ε	15 ±5%
Dielectric loss tangent	tgδ	0.0002
Linewidth frequency	f_0^*	9.3 [GHz]

Figure 4-1: (a) Schematic depicting the air-YIG interface. The external magnetic bias field $\mathbf{H}_0$ is oriented in a plane parallel to the interface. In the Voigt configuration, EM wave propagate perpendicular to the bias along $\hat{\mathbf{n}} \times \hat{\mathbf{H}}_0$ where $\hat{\mathbf{n}}$ denotes the interface normal. (b) Table of YIG response parameters provided by the manufacturer, Exxelia Temex.

for conciseness.

Working in the saturated regime of the YIG hysteresis curve, we consider biases that are well beyond the coercive field, which may be anywhere from 1 to a few Oe (i.e., ∼10 to ∼50 mT). In this regime, the DC magnetization is maximized to the point of saturation $\mathbf{M}_s$, and small signal analysis may be used to linearize Maxwell's equations governing electromagnetic wave propagation. The linear relationship between a time harmonic (AC) magnetic field $\mathbf{H}$ and resultant AC magnetization $\mathbf{M}$ such that $|\mathbf{H}| \ll |\mathbf{H}_0|$ is given by $\mathbf{H} + \mathbf{M} = \bar{\mu} \cdot \mathbf{H}$ where

$$\bar{\mu} = \mu_\perp \left(\bar{\mathbf{I}} - \hat{\mathbf{H}}_0 \hat{\mathbf{H}}_0 \right) - j\mu_\times \left(\hat{\mathbf{H}}_0 \times \bar{\mathbf{I}} \right) + \mu_\parallel \hat{\mathbf{H}}_0 \hat{\mathbf{H}}_0 \tag{4.1}$$

is the relative permeability tensor derived semi-classically from the Landau-Lifshitz-Gilbert equation [158] describing precessional motion of the total magnetization vector $\mathbf{M}_s + \mathbf{M}$. The dispersive tensor elements with respect to the radial frequency $\omega = 2\pi f$ are given by

$$\mu_\perp = 1 + \frac{\omega_s \tilde{\omega}_0}{\tilde{\omega}_0^2 - \omega^2} \ , \quad \mu_\times = \frac{\omega_s \omega}{\tilde{\omega}_0^2 - \omega^2} \ , \quad \mu_\parallel = 1 \ , \tag{4.2}$$

where $\omega_s = \mu_0 \gamma M_s$ and $\tilde{\omega}_0 = \omega_0 + j\alpha\omega$ with $\omega_0 = \mu_0 \gamma H_0$; the quantities μ_0, ω_0, and $\gamma = g_{\text{eff}} \mu_{\text{B}} / \hbar$ are respectively the permeability of freespace, Larmor precessional (resonant) frequency, and gyromagnetic ratio defined in terms of the effective Landé g-factor g_{eff}, Bohr

magneton μ_{B}, and reduced Planck constant $\hbar$. Material losses are accounted for in the loss rate α which is well defined on and off resonance at saturation [159].

Resonant cavity methods make it possible to determine α by measuring the linewidth ΔH associated with the imaginary part of $\mu_\perp$ at resonance [160]. In the saturated regime, $\alpha = \mu_0 \gamma \Delta H / 4\pi f_0^*$, where f_0^* denotes the resonant frequency at which the linewidth is measured. Off resonance, losses decrease significantly and the replacement of ΔH with ΔH_{eff} in the calculation of α is made.

Figure 4-1(b) provides a table of the necessary parameters used to calculate the relative permeability tensor elements of the YIG obtained from the specification sheet provided by the manufacturer, Exxelia Temex. In addition to those already mentioned, the table lists the relative dielectric constant ε and loss tangent tgδ.

4.2.2 Dispersion of guided electromagnetic modes

To obtain the dispersion of guided electromagnetic modes supported by a YIG slab of thickness $2h$, biased with a static uniform magnetic field $\mathbf{H}_0 = \hat{\mathbf{z}} H_0$ in the Voigt configuration and interfaced with air, we treat the slab as invariant with respect to the x-z plane and assume the propagation direction is perpendicular to the bias (i.e., the wavevector $\mathbf{k}$ is perpendicular to $\mathbf{H}_0$), in which case, the wave may be decomposed into transverse-electric (TE) and -magnetic (TM) modes, where transverse is defined with respect to $\mathbf{k}$. In the air and YIG regions, the electric E_z^{TE} and magnetic H_z^{TM} vector components of TE and TM bulk modes satisfy the source-free scalar Helmholtz equation

$$\left(\partial_y^2 - q_x^2 + \left\{k_{\mathrm{TE}}^2, k_{\mathrm{TM}}^2\right\}\right)\left\{E_z^{\mathrm{TE}}, H_z^{\mathrm{TM}}\right\} = 0 \ , \tag{4.3}$$

where the bulk wavenumbers $k_{\mathrm{TE}} = k_{\mathrm{TM}} = k_0\sqrt{\varepsilon_{\mathrm{r}}\mu_{\mathrm{r}}}$ in air, and $k_{\mathrm{TE}} = k_0\sqrt{\varepsilon\mu_{\mathrm{eff}}}$ and $k_{\mathrm{TM}} = k_0\sqrt{\varepsilon\mu_{\parallel}}$ in YIG; parameters ε_{r} and μ_{r} are the relative permittivity and permeability of air, $\mu_{\mathrm{eff}} = \mu_\perp - \mu_\times^2/\mu_\perp$ is the effective relative permeability experienced by the TE modes in YIG, and k_0 is the free space wavenumber (all other parameters are defined in Sec. 4.2.1). The magnetic $\left(H_x^{\mathrm{TE}}, H_y^{\mathrm{TE}}\right)$ and electric $\left(E_x^{\mathrm{TM}}, E_y^{\mathrm{TM}}\right)$ vector components of TE

and TM bulk modes are then recoverable from Maxwell's equations upon solving Eq. (4.3) for E_z^{TE} and H_z^{TM}.

Of particular interest are the topologically nontrivial TE bulk modes of YIG which experience an effective permeability μ_{eff} dependent on the external magnetic bias. Over the frequency range $\omega \in [\omega_l, \omega_u]$, where $\omega_u = \omega_0 + \omega_s$ and $\omega_l = \sqrt{\omega_0 \omega_u}$, the response may be characterized as an imperfect magnetic conductor with $\mathrm{Re}\{\mu_{\mathrm{eff}}\} < 0$, which corresponds to the nontrivial bandgap that forms in the dispersion. As a result, the YIG has a finite skin depth $\delta = 1/\mathrm{Im}\{k_{\mathrm{YIG}}\}$ in the bandgap, where k_{YIG} denotes the TE bulk wavenumber in YIG (in the following, k_{AIR} likewise denotes the TE bulk wavenumber in air). Figure 4-2(b) shows how the skin depth varies in the bandgap associated with a 500 mT bias. At the lower band edge ω_l, the YIG functions as a near perfect magnetic conductor with $\delta \sim 0$, and gradually transitions back to an insulator as frequency increases, with $\delta \to \infty$ as frequency approaches the upper band edge ω_u.

After obtaining the field profile of TE bulk modes in the air and YIG regions, the dispersion of TE guided modes supported by the slab (i.e., SMP and guided via total internal reflection) are obtained by enforcing continuity of E_z^{TE} and H_x^{TE} at each interface. It can be shown that the dispersion relation for TE modes guided by the slab via total internal reflection is [161, 162]

$$\begin{aligned} q_x^2 \mu_{\mathrm{r}}^2 \mu_{\times}^2 / \mu_{\perp}^2 = &\left[\kappa_{\mathrm{AIR}} \mu_{\mathrm{eff}} \coth\left(\kappa_{\mathrm{YIG}} h\right) + \kappa_{\mathrm{YIG}} \mu_{\mathrm{r}}\right] \\ &\times \left[\kappa_{\mathrm{AIR}} \mu_{\mathrm{eff}} \tanh\left(\kappa_{\mathrm{YIG}} h\right) + \kappa_{\mathrm{YIG}} \mu_{\mathrm{r}}\right] \ , \end{aligned} \tag{4.4}$$

where $\kappa_\nu^2 = q_x^2 - k_\nu^2$ for $\nu \in \{\mathrm{AIR}, \mathrm{YIG}\}$. Cutoff frequencies for n^{th} order modes that propagate above/below the bandgap are recovered when $q_x = k_{\mathrm{AIR}}$,

$$\omega_n^{\pm} = \sqrt{\frac{-B_n \pm \sqrt{B_n^2 - 4AC_n}}{2A}} \ : \ n \in \{0, 1, 2, \dots\} \ , \tag{4.5}$$

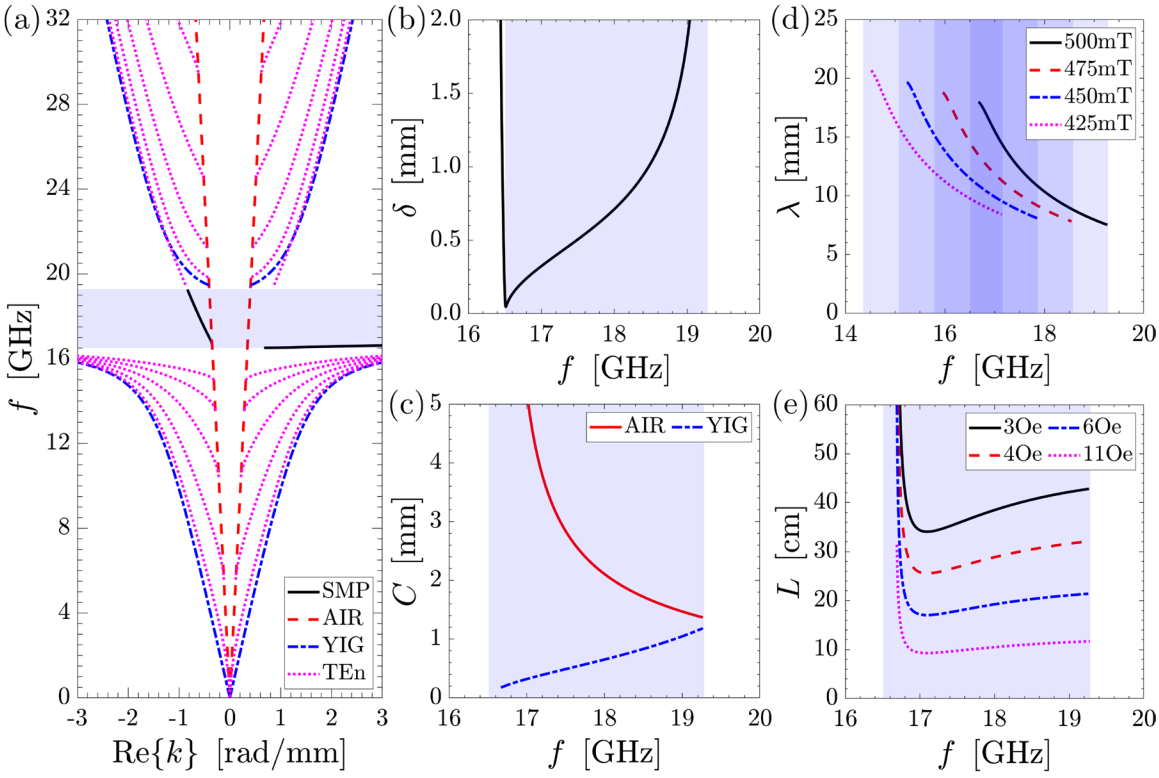

Figure 4-2: (a) Dispersion of TE bulk, upper-interface SMP, and n^{th} order guided modes ($n \in \{0, 1, 2, 3, 4\}$) for a 6mm thick YIG slab (i.e., $h = 3$mm) biased with 500mT in the Voigt configuration and interfaced with air. The shaded frequency band highlights the TE bulk bandgap. (b) Skin depth of YIG in the bandgap. (c) Confinement of the SMP in the air and YIG regions. (d) SMP wavelength for magnetic bias settings that decrease in magnitude from 500mT in steps of 25mT. The shaded bandgap regions correspond to each bias setting, with maximum overlap occurring over a narrow frequency band centered about ∼16.8GHz. (e) Propagation length L of the SMP, shown to decrease with increasing loss rate α (i.e., increasing effective linewidth ΔH_{eff}).

where

$$A = 4h^2 \left(\varepsilon - \mu_{\text{r}}\varepsilon_{\text{r}}\right) \ , \tag{4.6}$$

$$B_n = 4h^2 \left(\mu_{\text{r}}\varepsilon_{\text{r}}\omega_l^2 - \varepsilon\omega_u^2\right) - n^2\pi^2c^2 \ , \tag{4.7}$$

$$C_n = n^2\pi^2c^2\omega_l^2 \ . \tag{4.8}$$

In the thick slab limit $h \to \infty$, Eq. (4.4) factors into the dispersion relations of SMP modes

that propagate in the bandgap at the upper and lower interfaces of the slab [156, 161]

$$0 = (\kappa_{\mathrm{YIG}}\mu_{\mathrm{r}} + \kappa_{\mathrm{AIR}}\mu_{\mathrm{eff}} - q_x\mu_{\mathrm{r}}\mu_{\times}/\mu_{\perp}) \times (\kappa_{\mathrm{YIG}}\mu_{\mathrm{r}} + \kappa_{\mathrm{AIR}}\mu_{\mathrm{eff}} + q_x\mu_{\mathrm{r}}\mu_{\times}/\mu_{\perp}) \ . \tag{4.9}$$

Solutions for q_x that satisfy the n^{th} order guided, Eq. (4.4), and SMP, Eq. (4.9) mode dispersions are denoted k_{SMP} and k_{TEn} respectively, and must be obtained via numerical root search since there exists no closed form solutions. While the dispersion of n^{th} order guided modes is clearly reciprocal due to the q_x^2 dependence, it can be shown that each SMP mode is unidirectional at the upper/lower interfaces of the slab, propagating in the $\pm\hat{\mathbf{x}}$ direction for operating frequencies $\omega \in [\omega_l, \omega_u - \omega_s/2)$ and $\mp\hat{\mathbf{x}}$ direction for $\omega \in [\omega_u - \omega_s/2, \omega_u]$.

The dispersion of TE bulk, upper-interface SMP, and n^{th} order guided modes is shown in Fig. 4-2(a) for $h = 3$mm and $\mu_0 H_0 = 500$ mT. The SMP mode branch that propagates in the $-\hat{\mathbf{x}}$ direction for $\omega \in [\omega_u - \omega_s/2, \omega_u]$ attenuates differently on either side of the interface at rates κ_{AIR} and κ_{YIG} into the air and YIG regions. The higher these rates are, the more tightly confined the SMP is to the interface. Confinement $C = 1/\mathrm{Re}\{\kappa\}$ of the SMP is shown in Fig. 4-2(c). At the lower band edge $\omega_u - \omega_s/2$, the SMP is not well confined to the interface in the air region with $C \to \infty$, but tightly confined in the YIG region with $C \sim 0$. As frequency increases, confinement increases/decreases in the YIG/air regions. In Fig. 4-2(d), the SMP wavelength $\lambda = 2\pi/k_{\mathrm{SMP}}$ is shown for a few bias settings that decrease in magnitude from 500 mT in steps of 25 mT. As bias decreases, the spectral location of the bandgap red shifts. Over a narrow band centered about ∼16.8 GHz, the bandgap is common to all magnetic biases, and for a set frequency, each SMP mode exists within it having wavelengths that decrease with bias. The figure also suggests that if a nonuniform bias, slowly varying with respect to the SMP wavelength, were distributed across the slab, the bandgap would effectively broaden (i.e., the transmission of bulk radiation between two points in the spatial plane would be blocked over a broader frequency range), with a strong SMP excitation likely possible at some operating frequency within the broadened

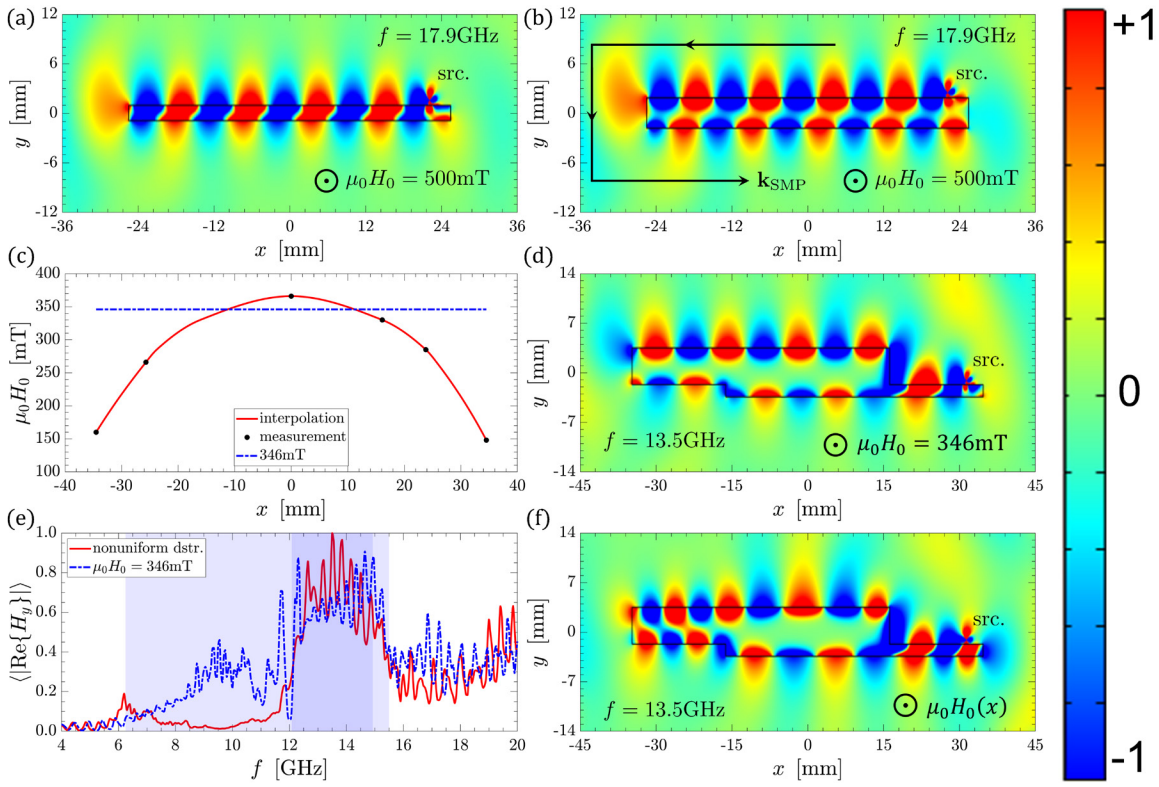

Figure 4-3: COMSOL generated normalized SMP field profile, excited using a near field magnetic dipole point source (src.) oriented perpendicular to the upper interface and positioned near the right edge of each biased YIG slab having dimensions (a) 50.6mm × 1.8mm and (b) 50.6mm × 3.6mm. The operating frequency is 17.9GHz, corresponding to the bandgap center. (c) Uniform and nonuniform magnetic bias distributions considered in FEM simulations to generate the SMP field profiles on the YIG slab structure outlined in panels (d) and (f) respectively. (e) A spatial average of the magnetic field magnitude normal to the uppermost interface, defined in Eq. (4.10) and normalized with respect to the maximum value associated with the nonuniform distribution. The dark shaded band centered about the selected operating frequency $f = 13.5$GHz corresponds to the bandgap center associated with the uniform bias distribution, while the light shaded band corresponds to the broadened bandgap associated with the nonuniform distribution. In each simulation, the computational domain is invariant with respect to the bias direction $\hat{\mathbf{z}}$.

bandgap due to SMP mode overlap. In fact, simulation and experiment later confirm this theory. Figure 4-2(e) shows the profound effect that loss has on the propagation length $L = 1/\left[2\mathrm{Im}\{k_{\mathrm{SMP}}\}\right]$. However, for this application, the bandgap is far enough from the resonant frequency ω_0 (i.e., off resonance, $\Delta H_{\mathrm{eff}} = 3$ Oe is used to define the loss rate α) and so, loss does not significantly damp the SMP mode.

4.2.3 SMP excitation

To excite the SMP mode, the easiest way is to use a near field source that induces a time harmonic magnetic dipole moment perpendicular to the air-YIG interface. For example, this type of excitation may be implemented experimentally using a small loop magnetic dipole antenna with the loop oriented in the plane of the interface. Figure 4-3(a),(b) shows field maps of the SMP excitation above 1.8 mm and 3.6 mm thick YIG slabs, using a magnetic dipole point source operating at the bandgap center frequency associated with a uniform 500 mT bias. To generate the field maps, finite element method (FEM) simulations are performed in COMSOL, where the computational domain in each case is invariant with respect to the bias direction $\hat{\mathbf{z}}$. Due to a nonzero confinement $C \sim 0.6$ mm in the YIG, as shown in Fig. 4-2(c), the magnetic field components of the SMP normal to the upper and lower interfaces begin to interfere considerably as thickness decreases from 3.6 mm, which forms a quasi-standing wave within the slab. In these simulations, an extremely fine adaptive physics based tetrahedral mesh, defined in the COMSOL software, was used. At the edges of the computational domain, a perfectly matched layer (PML) was applied to mimic an open and nonreflecting infinite domain.

4.2.4 Effects of nonuniformity in the external bias distribution

In Sec. 4.2.2, we speculated from Fig. 4-2(d) that if a nonuniform bias, slowly varying with respect to the SMP wavelength, were distributed across the YIG between two points in the spatial plane, the bandgap would effectively broaden since transmission of bulk radiation between the points would be blocked for operating frequencies within the broadened range. In addition, due to SMP mode overlap, we speculated that a strong SMP excitation would likely be possible for some operating frequency within the broadened bandgap. In what follows, we provide a simulation that confirms this theory.

Drawing a connection between the simulation described here and the measurement described in Sec. 4.3.2, we consider the YIG slab structure shown in Fig. 4-3(d),(f) which contains an abrupt change in the form of a step along the upper interface. The structure is

biased with (d) a uniform 346 mT, and (f) an interpolated nonuniform distribution obtained from measurement. The bias distributions in each case are shown in Fig. 4-3(c). In Fig. 4-3(e), a spatial average of the magnetic field magnitude normal to the uppermost interface defined by

$$\langle |\mathrm{Re}\{H_y\}| \rangle = \frac{1}{x_f - x_i} \int_{x_i}^{x_f} |\mathrm{Re}\{H_y(x, y_0)\}| \, dx \ , \tag{4.10}$$

with $x_i = -34.5$ mm, $x_f = 16.1$ mm, and $y_0 = 3.6$ mm, is shown for the uniform and nonuniform bias distributions, where each quantity is normalized with respect to the maximum value associated with the nonuniform distribution. The averaged field provides qualitative insight into how intense the field is at the uppermost interface over a broad range of frequencies. For the uniform and nonuniform distributions, the field peaks as a result of SMP propagation at the center of the dark shaded frequency band, which corresponds to the bandgap associated with the uniform distribution. Outside of this region where the SMP does not propagate, bulk radiation contributes to a nonzero field at the interface. However, for the nonuniform distribution, bulk radiation is suppressed significantly in the lightly shaded band corresponding to the broadened bandgap, relative to the case where the bias is uniform. Figure 4-3(d),(f) shows the SMP field profile for the uniform and nonuniform distributions respectively when the operating frequency is 13.5 GHz, corresponding to the bandgap center associated with the uniform bias. For the nonuniform distribution, SMP wavelength differs at various points along the interface in a way that is consistent with Fig. 4-2(d).

4.3 Experimental methods and measurement

To demonstrate the effectiveness of topological protection, we designed an experiment to measure transmission of the SMP between two small loop magnetic dipole antennas displaced a short distance above the upper interface between air and various YIG slab structures, including those considered for simulation in Secs. 4.2.3 and 4.2.4. Each structure is created by layering YIG plates having dimensions of 50.6 mm $\times$ 50.6 mm $\times$ 1.8 mm. Using

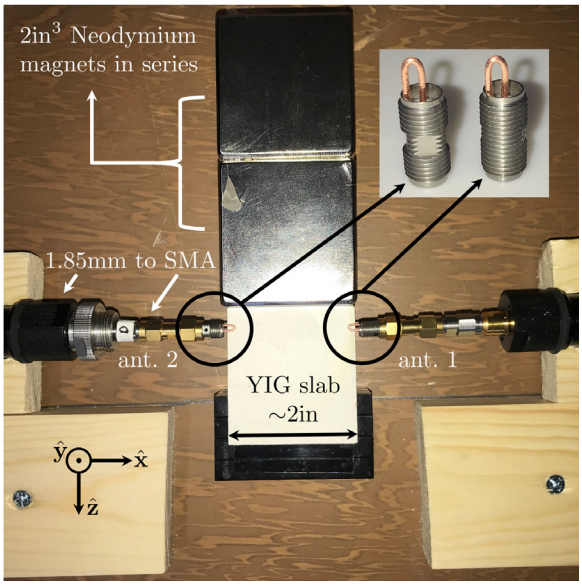

Figure 4-4: Top view of the apparatus used to conduct the experiment, where two Neodymium ferromagnets in series bias a YIG slab in the Voigt configuration, and two small loop magnetic dipole antennas (labeled ant. 1,2) mounted onto 1.85mm coaxial cables, displaced a small distance above the upper interface by an insulating cover (white), transmit and receive at operating frequencies between 4 and 22GHz. The inset in the top right corner shows a zoomed view of the antennas formed by connecting the inner SMA conductor to the outer via a piece of 19AWG copper wire with the enamel stripped off. A vector network analyzer (not shown) measures transmission.

a vector network analyzer, transmission is measured at operating frequencies in the range of 4 to 22 GHz.

A full top view of the apparatus used to conduct the experiment is shown in Fig. 4-4. Two 2 in^3 Neodymium magnets coated in Nickel, manufactured by K&J Magnetics, are connected in series to provide a magnetic bias distribution across the thin edge of each structure. Individually, the magnets provide a maximum surface field of ~575 mT. Additional perspective views of the apparatus are shown in Figs. 4-5(a),(c),(e).

4.3.1 Isolation Dependence on Slab Thickness

For the system under study, signal isolation in the bandgap is a measure of how efficiently the SMP is received by one antenna over the other. Since the SMP is unidirectional, an SMP launched by antenna 1 (ant. 1) takes the upper interface path, while an SMP launched by antenna 2 (ant. 2) takes the lower interface path. Due to the way the antennas are positioned, when the SMP is transmitted via the upper interface path, the flux is received

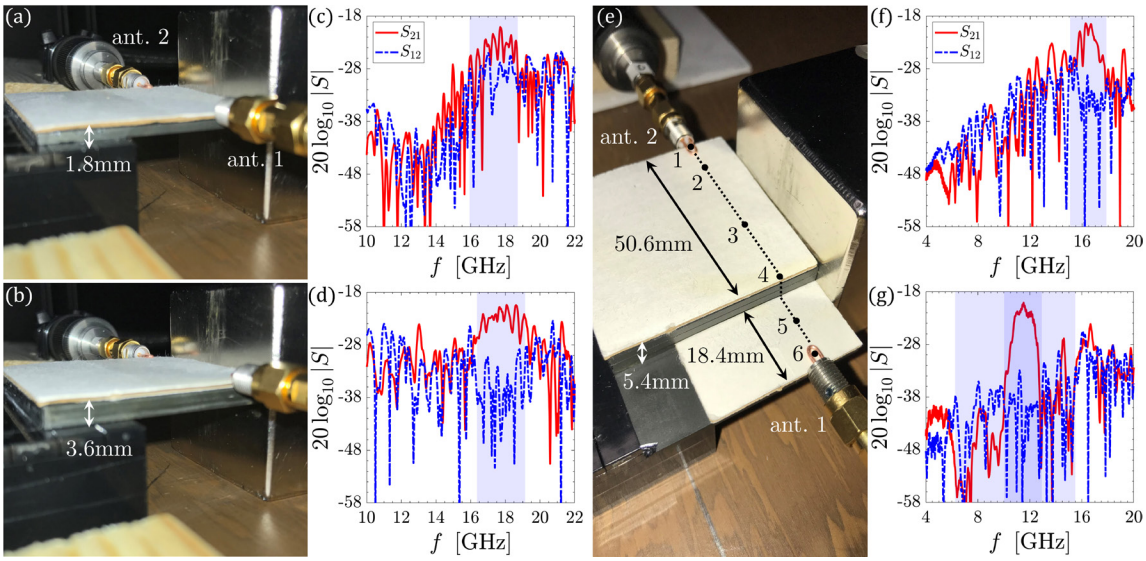

Figure 4-5: (a),(b) Perspective views of the apparatus for single and double stacked YIG plates having a combined thickness of 1.8mm and 3.6mm. In each case, the $\hat{\mathbf{z}}$ component of magnetic bias is measured using a gauss meter in the vicinity of 480mT and 495mT at a variety of points along the upper interface path between antennas. (c),(d) Measured transmission spectra for the 1.8mm and 3.6mm thick slabs respectively. Transmission is nonreciprocal, and peaks as a result of SMP propagation in the expected bandgap region associated with the measured bias. (e) Perspective view of the apparatus for the YIG slab structure shown in Fig. 4-3(d),(f), formed by stacking 4 YIG plates and sliding the bottom plate out 18.4mm. The entire structure is centered on the magnet which results in a near symmetric nonuniform bias distribution across the structure; see Fig. 4-3(c) for the interpolated distribution. Points labeled $\{1, 2, 3, 4, 5, 6\}$ correspond to locations along the upper interface where the magnetic field is measured in the vicinity of $\{160, 266, 366, 330, 285, 148\}$mT. The distance of each point from point 1 is $\{8.8, 34.5, 50.6, 58.3, 69\}$mm. (f) Measured S-parameters for a three layer structure, similar to those shown in (a) and (b) with the bias measured in the vicinity of 450mT. (g) Measured S-parameters for the slab structure shown in (e). In (f), the shaded frequency band corresponds to the bandgap associated with the measured bias. In (g), the lightly shaded band corresponds to the broadened bulk bandgap associated with the nonuniform bias distribution, and the dark shaded band centered about peak S_{21} corresponds to the bandgap associated with a uniform 275mT bias.

more efficiently because there would neither be diffraction at the edges nor scattering at the antenna feeds before being received. However, for a thin slab such as the one shown in Fig. 4-3(a), a nonzero confinement may result in the magnetic field of an SMP taking the lower interface path being detected at the upper interface by the receive antenna (i.e., ant. 1). In this case, path preference becomes less clear and would result in low isolation.

Figure 4-5(a),(b) shows a perspective view of the apparatus for 1.8 mm and 3.6 mm thick slabs constructed from one and two layered YIG plates. Using a MF100 Gauss meter by Extech Instruments, the $\hat{\mathbf{z}}$ component of magnetic bias (i.e., the bias component per-

pendicular to the line of sight between antennas) is measured in the vicinity of (a) 480 mT and (b) 495 mT, with slight deviations from these values at various points along the upper interface path. In Fig. 4-5(c),(d), the corresponding measured S-parameters are shown. Transmission of the SMP is nonreciprocal (i.e., $S_{21} \neq S_{12}$) with S_{21} peaking well within the expected bandgap region (shaded) associated with the measured bias. For this antenna configuration, we find a substantial increase in isolation when the slab thickness increases from 1.8 mm to 3.6 mm.

4.3.2 Topological Protection

The third slab structure under consideration is one having a step in the upper interface path, comparable to one SMP wavelength. Layering four YIG plates, the structure shown in Fig. 4-3(d),(f) is created by sliding the bottom plate out by 18.4 mm. This places its maximum dimension at 69 mm, slightly larger than the magnet dimension. As a result, the bias is substantially nonuniform across the structure relative to the previous two cases considered, but does not vary too significantly so as to dramatically alter the underlying physics. Figure 4-5(e) shows a perspective view of the apparatus, with the structure centered on the magnet. Points $\{1, 2, 3, 4, 5, 6\}$ correspond to locations along the upper interface path where the $\hat{\mathbf{z}}$ component of the bias is measured. The measured values and relative distances from point 1 are provided in the figure caption and shown in Fig. 4-3(e).

Figure 4-5(f),(g) shows the measured transmission for (f) a three layer slab, similar to the one and two layer slabs shown in Fig. 4-5(d),(f), with the $\hat{\mathbf{z}}$ component of the bias measured in the vicinity of 450 mT, and (g) the elongated four layered structure biased with a nonuniform field distribution. In (f), the shaded frequency band corresponds to the bandgap associated with the measured bias, and in (g), the lightly shaded band corresponds to the broadened bandgap associated with the nonuniform bias distribution, while the dark shaded band centered about peak S_{21} has the same bandwidth and location as the bandgap associated with a uniform 275 mT bias. In all of the four cases considered, SMP transmission peaks in the bandgap near the same level (i.e., $20 \log_{10} |S_{21}| \simeq -20$ dB), demonstrating that

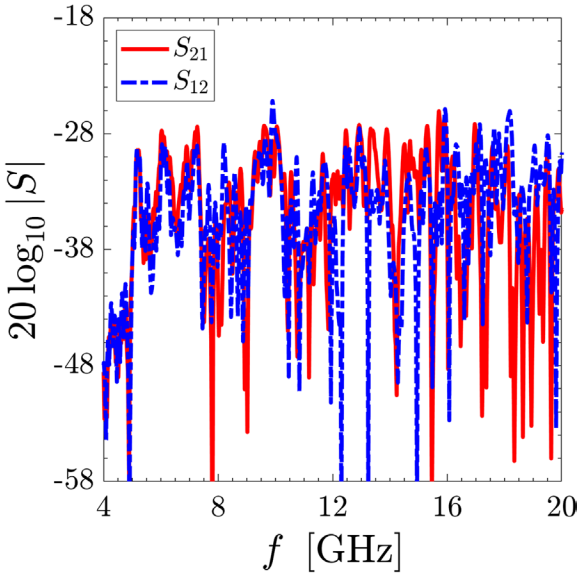

Figure 4-6: Measured S-parameters for the slab structure shown in Fig. 4-5(e) when the bias is removed, where slight deviations in S_{21} and S_{12} are attributed to a small remnant magnetization. At operating frequencies beyond ∼5GHz, a fair amount of transmission occurs due to bulk radiation that is guided by the structure via total internal reflection. When biased, transmission is suppressed significantly in the broadened bandgap as shown in Fig. 4-5(g).

the SMP is indeed topologically protected against reflection. For reference, a transmission measurement obtained in the absence of bias (i.e., with the magnet removed) for the four layer structure is shown in Fig. 4-6.

A peak in S_{21} is directly correlated with a peak in the magnetic flux associated with the SMP received by antenna 2. Likewise, the received flux may be correlated with a spatial average of the magnetic field magnitude normal to and distributed across the uppermost interface. In Fig. 4-3(e), it is shown that this spatial average obtained from simulation peaks within the broadened bandgap over a frequency band corresponding to the bandgap associated with a uniform 346 mT bias, and confirmed this peak was in fact due to SMP propagation by examining the field profile shown in 4-3(f). However, in experiment, we find that S_{21} peaks within a frequency band corresponding to the bandgap associated with a uniform 275 mT bias. The slight spectral shift of the SMP resonance observed in experiment is likely attributed to demagnetization (which we did not account for in our model), since the total bias field $\mathbf{H}_0$ is not strictly oriented in the Voigt configuration (i.e., in the

simulation, we only consider the bias component perpendicular to the line of sight between antennas). In addition, the broadened bandgap effectively blocks transmission of bulk mode radiation between two points in the spatial plane which is evident from both simulation and experiment.

4.4 Summary

In this chapter, we obtained experimental evidence of topologically protected unidirectional SMPs guided along the interface between air and various YIG slab structures biased with an external magnetic bias field in the Voigt configuration. The SMPs are transmitted and received via two small loop magnetic dipole antennas placed a distance across from each other near the interface. We showed that for a fixed antenna position, isolation in the bandgap increases with thickness as a result of the lower interface path becoming less preferred than the upper interface path. In addition, we showed that the SMP is topologically protected against reflection when encountering an abrupt change in the interface as peak transmission of the SMP remained largely unaffected. Furthermore, we showed in simulation and experiment that a fair degree of nonuniformity in the bias distributed across the structure has the net effect of broadening the bulk bandgap without compromising the SMP resonance.

Chapter 5

Conclusion

In this dissertation, we investigated the dispersive properties of two types of highly nonreciprocal (unidirectional) surface waves, surface plasmon polaritons (SPPs) and surface magnon polaritons (SMPs), guided by the interface between free-space and a variety of 2D and 3D gyrotropic continua. Our research builds on previous work done in the areas in nonreciprocal electromagnetics and topological photonics in the following ways: (1) in Chap. 2, we developed new analytic formalism to to model near-field excitations of SPPs on a magnetized plasma slab (i.e., a plasma slab biased with an external magnetic bias field), (2) in Chap. 3, we developed new formalism to predict the spectral location of bandgaps in the quasi-transverse-magnetic SPP dispersion for 2D materials, and investigated a non-traditional way of achieving a gyrotropic response (i.e., without an external magnetic bias field) in graphene, and (3) in Chap. 4 we experimentally verify the unidirectional nature of a recently theorized topologically protected, unidirectional SMP mode. This chapter serves as a cumulative summary of the key findings presented in each chapter of the dissertation.

In Chap. 2, we solved the dispersion relation for SPP modes supported by the interface between free-space and a 3D magnetized plasma using a numerical root. In addition, we identified a common bulk bandgap, common to all propagation angles made with respect to the external magnetic bias direction, in which unidirectional, hyperbolic like SPP modes are found to propagate. Importantly, the reflection and transmission tensor coefficients

were also obtained for a finite thickness slab immersed in free-space, which were used in the evaluation of the scattered fields due to a localized near-field electric current density. Evaluation of the inverse Fourier transform integral in the definition of the scattered fields was compared with the field pattern obtained in COMSOL using the finite-element method, where we found good agreement between the two methods.

In Chap. 3, conditions on the spectral location of bandgaps in the dispersion of quasi-transverse-magnetic (QTM) SPP modes for anisotropic 2D materials are obtained. For two examples of anisotropic materials (i.e., gyrotropic graphene and hyperbolic black phosphorus), we demonstrated the effectiveness of the proposed formalism. In addition, we investigated the nonreciprocal effect of exchange splitting in a monolayer chromium triiodide (CrI_3)-graphene van der Waals heterostructure using density-functional theory where effective exchange fields of hundreds of Tesla were predicted. These enormous fields served as an effective magnetic bias for the graphene layer. Differences between the exchange field and external magnetic bias field cases are compared contrasted. While the graphene-CrI_3 heterostructure was found to support a unidirectional edge SPP, it did so only for separations smaller than the equilibrium separation. In addition, we found that the SPP did not propagate well relative to edge SPPs that propagate on graphene in an external magnetic bias field, which is largely attributed to material loss.

In Chap. 4, we obtained experimental evidence of a topologically protected, unidirectional SMP guided along the interface between free-space (air) and various YIG slab structures, biased with an external magnetic bias field in the Voigt configuration. We also investigated the effect that a nonuniform bias distribution along the interface has on the SMP. Importantly, we found that the experimental results aligned well with our simulated and numerical results.

Bibliography

[1] Junxi Zhang, Lide Zhang, and Wei Xu. Surface plasmon polaritons: physics and applications. *Journal of Physics D: Applied Physics*, 45(11):113001, feb 2012.

[2] Tapan K. Sarkar, Mohammad N. Abdallah, Magdalena Salazar-Palma, and Walid M. Dyab. Surface plasmons-polaritons, surface waves, and zenneck waves: Clarification of the terms and a description of the concepts and their evolution. *IEEE Antennas and Propagation Magazine*, 59(3):77–93, 2017.

[3] Jamison Sloan, Nicholas Rivera, John D. Joannopoulos, Ido Kaminer, and Marin Soljačić. Controlling spins with surface magnon polaritons. *Phys. Rev. B*, 100:235453, Dec 2019.

[4] D. N. Basov, M. M. Fogler, and F. J. García de Abajo. Polaritons in van der waals materials. *Science*, 354(6309):aag1992, 2016.

[5] Tony Low, Andrey Chaves, Joshua Caldwell, Anshuman Kumar, Nicholas Fang, Phaedon Avouris, Tony Heinz, Francisco Guinea, Luis Martin-Moreno, and Frank Koppens. Polaritons in layered two-dimensional materials. *Nature Materials*, 16, 11 2016.

[6] Yun You, P. A. D. Gonçalves, Linfang Shen, Martijn Wubs, Xiaohua Deng, and Sanshui Xiao. Magnetoplasmons in monolayer black phosphorus structures. *Opt. Lett.*, 44(3):554–557, Feb 2019.

[7] G. Ni, Alexander McLeod, Z. Sun, Lei Wang, L. Xiong, Kirk Post, Sai Sunku, B.-Y Jiang, J. Hone, C. Dean, Michael Fogler, and D. Basov. Fundamental limits to graphene plasmonics. *Nature*, 557, 05 2018.

[8] Tetsuyuki Ochiai. Non-reciprocity and topology in optics: one-way road for light via surface magnon polariton. *Science and Technology of Advanced Materials*, 16(1):014401, 2015.

[9] Xiao Lin, Nicholas Rivera, Josué J López, Ido Kaminer, Hongsheng Chen, and Marin Soljačić. Tailoring the energy distribution and loss of 2d plasmons. *New Journal of Physics*, 18(10):105007, oct 2016.

[10] Jacob B. Khurgin. Relative merits of phononics vs. plasmonics: the energy balance approach. *Nanophotonics*, 7(1):305–316, 2018.

[11] Jacob Khurgin. How to deal with the loss in plasmonics and metamaterials. *Nature nanotechnology*, 10:2–6, 01 2015.

[12] R.E. Camley. Nonreciprocal surface waves. *Surface Science Reports*, 7(3):103–187, 1987.

[13] Zheng Wang, Y. D. Chong, John D. Joannopoulos, and Marin Soljačić. Reflection-free one-way edge modes in a gyromagnetic photonic crystal. *Phys. Rev. Lett.*, 100:013905, Jan 2008.

[14] Zongfu Yu, Georgios Veronis, Zheng Wang, and Shanhui Fan. One-way electromagnetic waveguide formed at the interface between a plasmonic metal under a static magnetic field and a photonic crystal. *Phys. Rev. Lett.*, 100:023902, Jan 2008.

[15] Biao Yang, Mark Lawrence, Wenlong Gao, Qinghua Guo, and Shuang Zhang. One-way helical electromagnetic wave propagation supported by magnetized plasma. *Scientific Reports*, 6, 10 2014.

[16] Faezeh Fesharaki, Cevdet Akyel, and Kaiyan Wu. Broadband substrate integrated waveguide edge-guided mode isolator. *Electronics Letters*, 49:269–271, 02 2013.

[17] Farhan A. Ghaffar, Joey R. Bray, Mohammed Vaseem, Langis Roy, and Atif Shamim. Theory and design of tunable full-mode and half-mode ferrite waveguide isolators. *IEEE Transactions on Magnetics*, 55(8):1–8, 2019.

[18] Christopher K. Seewald and Joey R. Bray. Ferrite-filled antisymmetrically biased rectangular waveguide isolator using magnetostatic surface wave modes. *IEEE Transactions on Microwave Theory and Techniques*, 58(6):1493–1501, 2010.

[19] Kejie Fang, Zongfu Yu, Victor Liu, and Shanhui Fan. Ultracompact nonreciprocal optical isolator based on guided resonance in a magneto-optical photonic crystal slab. *Opt. Lett.*, 36(21):4254–4256, Nov 2011.

[20] M. J. Sun, M. W. Muller, and W. S. C. Chang. Thin-film waveguide gyrators: a theoretical analysis. *Appl. Opt.*, 16(11):2986–2993, Nov 1977.

[21] Seyyed Ali Hassani Gangaraj and George W. Hanson. Topologically protected unidirectional surface states in biased ferrites: Duality and application to directional couplers. *IEEE Antennas and Wireless Propagation Letters*, 16:449–452, 2017.

[22] S. Ali Hassani Gangaraj and Francesco Monticone. Coupled topological surface modes in gyrotropic structures: Green's function analysis. *IEEE Antennas and Wireless Propagation Letters*, 17(11):1993–1997, 2018.

[23] S. Pakniyat, A. M. Holmes, G. W. Hanson, S. A. H. Gangaraj, M. Antezza, M. G. Silveirinha, S. Jam, and F. Monticone. Non-reciprocal, robust surface plasmon polaritons on gyrotropic interfaces. *IEEE Transactions on Antennas and Propagation*, 68(5):3718–3729, 2020.

[24] Alexander M. Holmes and George W. Hanson. Conditions for photonic bandgaps in two-dimensional materials. *Journal of Applied Physics*, 129(1):015302, 2021.

[25] Alexander M. Holmes, Samaneh Pakniyat, S. Ali Hassani Gangaraj, Francesco Monticone, Michael Weinert, and George W. Hanson. Exchange splitting and exchange-induced nonreciprocal photonic behavior of graphene in Cri_3-graphene van der waals heterostructures. *Phys. Rev. B*, 102:075435, Aug 2020.

[26] Alexander M. Holmes, Mohsen Sabbaghi, and George W. Hanson. Experimental realization of topologically protected unidirectional surface magnon polaritons on ceramic yig ferrites. *Phys. Rev. B*, 104:214433, Dec 2021.

[27] E.J. Rothwell and M.J. Cloud. *Electromagnetics*. Electrical Engineering Textbook Series. CRC Press, 2018.

[28] George Hanson and Alexander Yakovlev. Operator theory for electromagnetics. an introduction. 01 2002.

[29] A.D. Yaghjian. Electric dyadic green's functions in the source region. *Proceedings of the IEEE*, 68(2):248–263, 1980.

[30] M. S. Kushwaha and P. Halevi. Magnetoplasmons in thin films in the voigt configuration. *Phys. Rev. B*, 36:5960–5967, Oct 1987.

[31] S. R. Seshadri. Excitation of surface waves on a perfectly conducting screen covered with anisotropic plasma. *IRE Transactions on Microwave Theory and Techniques*, 10(6):573–578, 1962.

[32] D.M. Bolle and S.H. Talisa. Fundamental considerations in miuimeter and near-millimeter component design employing magnetoplasmons. *IEEE Transactions on Microwave Theory and Techniques*, 29(9):916–923, 1981.

[33] J. J. Brion, R. F. Wallis, A. Hartstein, and E. Burstein. Theory of surface magnetoplasmons in semiconductors. *Phys. Rev. Lett.*, 28:1455–1458, May 1972.

[34] Alexander Schuchinsky and X. Yan. *Migration and Collision of Magnetoplasmon Modes in Magnetised Planar Semiconductor-Dielectric Layered Structures*, pages 255–266. Springer, 2009. ISBN: 1874–6500.

[35] Manvir S. Kushwaha. Plasmons and magnetoplasmons in semiconductor heterostructures. *Surface Science Reports*, 41(1):1–416, 2001.

[36] Arthur R. Davoyan and Nader Engheta. Theory of wave propagation in magnetized near-zero-epsilon metamaterials: Evidence for one-way photonic states and magnetically switched transparency and opacity. *Phys. Rev. Lett.*, 111:257401, Dec 2013.

[37] Tomoki Ozawa, Hannah M. Price, Alberto Amo, Nathan Goldman, Mohammad Hafezi, Ling Lu, Mikael C. Rechtsman, David Schuster, Jonathan Simon, Oded Zilberberg, and Iacopo Carusotto. Topological photonics. *Rev. Mod. Phys.*, 91:015006, Mar 2019.

[38] Ling Lu, John Joannopoulos, and Marin Soljačić. Topological photonics. *Nature Photonics*, 8, 08 2014.

[39] Mikael Rechtsman, Julia Zeuner, Yonatan Plotnik, Yaakov Lumer, Daniel Podolsky, Felix Dreisow, Stefan Nolte, Mordechai Segev, and Alexander Szameit. Photonic floquet topological insulators. *Nature*, 496:196–200, 04 2013.

[40] Mário G. Silveirinha. Chern invariants for continuous media. *Phys. Rev. B*, 92:125153, Sep 2015.

[41] F. D. M. Haldane and S. Raghu. Possible realization of directional optical waveguides in photonic crystals with broken time-reversal symmetry. *Phys. Rev. Lett.*, 100:013904, Jan 2008.

[42] S. Raghu and F. D. M. Haldane. Analogs of quantum-hall-effect edge states in photonic crystals. *Phys. Rev. A*, 78:033834, Sep 2008.

[43] S. Ali Hassani Gangaraj, Mário G. Silveirinha, and George W. Hanson. Berry phase, berry connection, and chern number for a continuum bianisotropic material from a classical electromagnetics perspective. *IEEE Journal on Multiscale and Multiphysics Computational Techniques*, 2:3–17, 2017.

[44] Scott A. Skirlo, Ling Lu, and Marin Soljačić. Multimode one-way waveguides of large chern numbers. *Phys. Rev. Lett.*, 113:113904, Sep 2014.

[45] Ali Hassani Gangaraj, Andrei Nemilentsau, and George Hanson. Corrigendum: The effects of three-dimensional defects on one-way surface plasmon propagation for photonic topological insulators comprised of continuum media. *Scientific Reports*, 7, 07 2017.

[46] S. Ali Hassani Gangaraj, George W. Hanson, and Mauro Antezza. Robust entanglement with three-dimensional nonreciprocal photonic topological insulators. *Phys. Rev. A*, 95:063807, Jun 2017.

[47] Mário G. Silveirinha, S. Ali Hassani Gangaraj, George W. Hanson, and Mauro Antezza. Fluctuation-induced forces on an atom near a photonic topological material. *Phys. Rev. A*, 97:022509, Feb 2018.

[48] S. Ali Hassani Gangaraj, George W. Hanson, Mauro Antezza, and Mário G. Silveirinha. Spontaneous lateral atomic recoil force close to a photonic topological material. *Phys. Rev. B*, 97:201108, May 2018.

[49] S. Ali Hassani Gangaraj, George W. Hanson, Mário G. Silveirinha, Kunal Shastri, Mauro Antezza, and Francesco Monticone. Unidirectional and diffractionless surface plasmon polaritons on three-dimensional nonreciprocal plasmonic platforms. *Phys. Rev. B*, 99:245414, Jun 2019.

[50] Y. Mazor and Ben Z. Steinberg. Metaweaves: Sector-way nonreciprocal metasurfaces. *Phys. Rev. Lett.*, 112:153901, Apr 2014.

[51] A. Leviyev, B. Stein, A. Christofi, T. Galfsky, H. Krishnamoorthy, I. L. Kuskovsky, V. Menon, and A. B. Khanikaev. Nonreciprocity and one-way topological transitions in hyperbolic metamaterials. *APL Photonics*, 2(7):076103, 2017.

[52] E. D. Palik, R. Kaplan, R. W. Gammon, H. Kaplan, R. F. Wallis, and J. J. Quinn. Coupled surface magnetoplasmon-optic-phonon polariton modes on insb. *Phys. Rev. B*, 13:2497–2506, Mar 1976.

[53] Siddharth Buddhiraju, Yu Shi, Alex Song, Casey Wojcik, Momchil Minkov, Ian Williamson, Avik Dutt, and Shanhui Fan. Absence of unidirectionally propagating surface plasmon-polaritons at nonreciprocal metal-dielectric interfaces. *Nature Communications*, 11, 02 2020.

[54] S. Ali Hassani Gangaraj and Francesco Monticone. Do truly unidirectional surface plasmon-polaritons exist? *Optica*, 6(9):1158–1165, Sep 2019.

[55] H.C. Chen. *Theory of Electromagnetic Waves: A Coordinate-free Approach*. Electrical Engineering Series. McGraw-Hill Book Company, 1983.

[56] Wenlong Gao, Biao Yang, Mark Lawrence, Fengzhou Fang, Benjamin Béri, and Shuang Zhang. Plasmon weyl degeneracies in magnetized plasma. *arxiv*, 7, 11 2015.

[57] Mário G. Silveirinha. Optical instabilities and spontaneous light emission by polarizable moving matter. *Phys. Rev. X*, 4:031013, Jul 2014.

[58] K. S. Novoselov, A. K. Geim, S. V. Morozov, D. Jiang, Y. Zhang, S. V. Dubonos, I. V. Grigorieva, and A. A. Firsov. Electric field effect in atomically thin carbon films. *Science*, 306(5696):666–669, 2004.

[59] K. Novoselov, A.K. Geim, S. Morozov, Dingde Jiang, Mikhail Katsnelson, Irina Grigorieva, S.V. Dubonos, and Anatoly Firsov. Two-dimensional gas of massless dirac fermions in graphene. *Nature*, 438:197–200, 12 2005.

[60] Qing Hua Wang, Kourosh Kalantar-Zadeh, Andras Kis, Jonathan N. Coleman, and Michael S. Strano. Electronics and optoelectronics of two-dimensional transition metal dichalcogenides. *Nature Nanotechnology*, 7(11):699–712, nov 2012.

[61] Minoru Osada and Takayoshi Sasaki. Two-dimensional dielectric nanosheets: Novel nanoelectronics from nanocrystal building blocks. *Advanced Materials*, 24(2):210–228, 2012.

[62] Anthony Ayari, Enrique Cobas, Ololade Ogundadegbe, and Michael S. Fuhrer. Realization and electrical characterization of ultrathin crystals of layered transition-metal dichalcogenides. *Journal of Applied Physics*, 101(1):014507, 2007.

[63] Zubin Jacob. Nanophotonics: Hyperbolic phonon-polaritons. *Nature materials*, 13:1081–3, 11 2014.

[64] Wenyang Qu, Feilin Gou, and Changhong Ke. Thermal-induced irreversible straining of ultrathin boron nitride nanosheets. *Applied Physics Letters*, 114(5):051901, 2019.

[65] D. Pacilé, J. C. Meyer, Ç. Ö. Girit, and A. Zettl. The two-dimensional phase of boron nitride: Few-atomic-layer sheets and suspended membranes. *Applied Physics Letters*, 92(13):133107, 2008.

[66] Hodjat Hajian, Ivan D. Rukhlenko, George W. Hanson, Tony Low, Bayram Butun, and Ekmel Ozbay. Tunable plasmon-phonon polaritons in anisotropic 2d materials on hexagonal boron nitride. *Nanophotonics*, (0):20200080, 2020.

[67] Tony Low, Rafael Roldán, Han Wang, Fengnian Xia, Phaedon Avouris, Luis Martín Moreno, and Francisco Guinea. Plasmons and screening in monolayer and multilayer black phosphorus. *Phys. Rev. Lett.*, 113:106802, Sep 2014.

[68] Tony Low, A. S. Rodin, A. Carvalho, Yongjin Jiang, Han Wang, Fengnian Xia, and A. H. Castro Neto. Tunable optical properties of multilayer black phosphorus thin films. *Phys. Rev. B*, 90:075434, Aug 2014.

[69] Alexandra Carvalho, Min Wang, Xi Zhu, Aleksandr Rodin, Haibin Su, and Antonio Castro Neto. Phosphorene: From theory to applications. *Nature Reviews Materials*, 1:16061, 08 2016.

[70] Michelle Sherrott, William Whitney, Deep Jariwala, Souvik Biswas, Cora Went, Joeson Wong, George Rossman, and Harry Atwater. Anisotropic quantum well electrooptics in few-layer black phosphorus. *Nano Letters*, 19, 12 2018.

[71] Zizhuo Liu and Koray Aydin. Localized surface plasmons in nanostructured monolayer black phosphorus. *Nano letters*, 16, 05 2016.

[72] Sina Abedini Dereshgi, Zizhuo Liu, and Koray Aydin. Anisotropic localized surface plasmons in borophene. *Opt. Express*, 28(11):16725–16739, May.

[73] Gonzalo Álvarez Pérez, Thomas G. Folland, Ion Errea, Javier Taboada-Gutiérrez, Jiahua Duan, Javier Martín-Sánchez, Ana I. F. Tresguerres-Mata, Joseph R. Matson, Andrei Bylinkin, Mingze He, Weiliang Ma, Qiaoliang Bao, José Ignacio Martín, Joshua D. Caldwell, Alexey Y. Nikitin, and Pablo Alonso-González. Infrared permittivity of the biaxial van der waals semiconductor a-moo3 from near- and far-field correlative studies. *Advanced Materials*, 32(29):1908176, 2020.

[74] A.K. Geim and Irina Grigorieva. Van der waals heterostructures. *Nature*, 499:419–25, 07 2013.

[75] L. Ponomarenko, A. Geim, Alexander Zhukov, Rashid Jalil, S. Morozov, K. Novoselov, V. Cheianov, Vladimir Falko, K Watanabe, Takashi Taniguchi, and Roman Gorbachev. Tunable metal-insulator transition in double-layer graphene heterostructures. *Nature Physics*, 7, 07 2011.

[76] Liam Britnell, Roman Gorbachev, Rashid Jalil, B Belle, Fredrik Schedin, Artem Mishchenko, Thanasis Georgiou, Mikhail Katsnelson, Laurence Eaves, S Morozov, Nuno Peres, Jon Leist, A Geim, K Novoselov, and L Ponomarenko. Field-effect tunneling transistor based on vertical graphene heterostructures. *Science (New York, N.Y.)*, 335:947–50, 02 2012.

[77] Thanasis Georgiou, Rashid Jalil, Branson Belle, Liam Britnell, Roman Gorbachev, Sergey Morozov, Yong-Jin Kim, Ali Gholinia, Sarah Haigh, Oleg Makarovsky, Laurence Eaves, Leonid Ponomarenko, Andre Geim, Kostya Novoselov, and Artem Mishchenko. Vertical field-effect transistor based on graphene-ws 2 heterostructures for flexible and transparent electronics. *Nature nanotechnology*, 8, 12 2012.

[78] Sandeep Inampudi, Mina Nazari, Ali Forouzmand, and Hossein Mosallaei. Manipulation of surface plasmon polariton propagation on isotropic and anisotropic two-dimensional materials coupled to boron nitride heterostructures. *Journal of Applied Physics*, 119:025301, 01 2016.

[79] K. Novoselov, Artem Mishchenko, A. Carvalho, and Antonio Castro Neto. 2d materials and van der waals heterostructures. *Science*, 353:aac9439–aac9439, 07 2016.

[80] Vladimir Lenets, Oleh Yermakov, Andrey Sayanskiy, Juan Baena, Enrica Martini, Stanislav Glybovski, and Stefano Maci. Surface waves on self-complementary metasurfaces: intrinsic hyperbolicity, dual-directional canalization and te-tm polarization degeneracy, 2020.

[81] Nanfang yu and Federico Capasso. Flat optics with designer metasurfaces. *Nature materials*, 13:139–50, 01 2014.

[82] Alexander Kildishev, Alexandra Boltasseva, and Vladimir Shalaev. Planar photonics with metasurfaces. *Science (New York, N.Y.)*, 339:1232009, 03 2013.

[83] Trevon Badloe, Jungho Mun, and Junsuk Rho. Metasurfaces-based absorption and reflection control: Perfect absorbers and reflectors. *Journal of Nanomaterials*, 2017:1–18, 11 2017.

[84] J. Gomez-Diaz, Mykhailo Tymchenko, and A. Alù. Hyperbolic metasurfaces: Surface plasmons, light-matter interactions, and physical implementation using graphene strips. *Optical Materials Express*, 5:2313, 10 2015.

[85] Kaveh Khaliji, Arya Fallahi, Luis Martin-Moreno, and Tony Low. Tunable plasmon-enhanced birefringence in ribbon array of anisotropic two-dimensional materials. *Physical Review B*, 95:201401, 01 2017.

[86] Dafei Jin, Thomas Christensen, Marin Soljačić, Nicholas Fang, Ling Lu, and Xiang Zhang. Infrared topological plasmons in graphene. *Physical Review Letters*, 118, 02 2017.

[87] Anshuman Kumar, Andrei Nemilentsau, Kin Hung Fung, George Hanson, Nicholas Fang, and Tony Low. Chiral plasmon in gapped dirac systems. *Physical Review B*, 93:041413(R), 01 2016.

[88] Aires Ferreira, Nuno Peres, and Antonio Castro Neto. Confined magneto-optical waves in graphene. *Physical Review B*, 85, 02 2012.

[89] George Hanson. Dyadic green's functions for an anisotropic, non-local model of biased graphene. *Antennas and Propagation, IEEE Transactions on*, 56:747 – 757, 04 2008.

[90] jean-marie Poumirol, Peter Liu, Tetiana Slipchenko, A. Nikitin, Luis Martin-Moreno, Jérôme Faist, and Alexey Kuzmenko. Electrically controlled terahertz magneto-optical phenomena in continuous and patterned graphene. *Nature Communications*, 8, 03 2017.

[91] S. A. Hassani Gangaraj, T. Low, A. Nemilentsau, and G. W. Hanson. Directive surface plasmons on tunable two-dimensional hyperbolic metasurfaces and black phosphorus: Green's function and complex plane analysis. *IEEE Transactions on Antennas and Propagation*, 65(3):1174–1186, 2017.

[92] Xiao-Yong He. Comparison of graphene-based transverse magnetic and electric surface plasmon modes. *IEEE Journal of Selected Topics in Quantum Electronics*, 20:4600106, 01 2014.

[93] George W. Hanson. Dyadic green's functions and guided surface waves for a surface conductivity model of graphene. *Journal of Applied Physics*, 103(6):064302, 2008.

[94] Valery Gusynin, Sergei Sharapov, and J.P. Carbotte. Magneto-optical conductivity in graphene. *Journal of Physics: Condensed Matter*, 19, 06 2007.

[95] Andrei Nemilentsau, Tony Low, and George Hanson. Anisotropic 2d materials for tunable hyperbolic plasmonics. *Phys. Rev. Lett.*, 116:066804, Feb 2016.

[96] K. S. Novoselov, A. K. Geim, S. V. Morozov, D. Jiang, Y. Zhang, S. V. Dubonos, I. V. Grigorieva, and A. A. Firsov. Electric field effect in atomically thin carbon films. *Science*, 306(5696):666–669, 2004.

[97] S. Das Sarma, Shaffique Adam, E. H. Hwang, and Enrico Rossi. Electronic transport in two-dimensional graphene. *Rev. Mod. Phys.*, 83:407–470, May 2011.

[98] Michael A. McGuire, Hemant Dixit, Valentino R. Cooper, and Brian C. Sales. Coupling of crystal structure and magnetism in the layered, ferromagnetic insulator cri3. *Chemistry of Materials*, 27(2):612–620, 2015.

[99] Bevin Huang, Genevieve Clark, Efrén Navarro-Moratalla, Dahlia Klein, Ran Cheng, Kyle Seyler, Ding Zhong, Emma Schmidgall, Michael McGuire, David Cobden, Wang Yao, Xiao di, Pablo Jarillo-Herrero, and Xiaodong Xu. Layer-dependent ferromagnetism in a van der waals crystal down to the monolayer limit. *Nature*, 546, 03 2017.

[100] Junyi Liu, Qiang Sun, Yoshiyuki Kawazoe, and Puru Jena. Exfoliating biocompatible ferromagnetic cr-trihalide monolayers. *Phys. Chem. Chem. Phys.*, 18:8777–8784, 2016.

[101] Wei-Bing Zhang, Qian Qu, Peng Zhu, and Chi-Hang Lam. Robust intrinsic ferromagnetism and half semiconductivity in stable two-dimensional single-layer chromium trihalides. *J. Mater. Chem. C*, 3:12457–12468, 2015.

[102] Bevin Huang, Genevieve Clark, Efrén Navarro-Moratalla, Dahlia Klein, Ran Cheng, Kyle Seyler, Ding Zhong, Emma Schmidgall, Michael McGuire, David Cobden, Wang Yao, Xiao di, Pablo Jarillo-Herrero, and Xiaodong Xu. Layer-dependent ferromagnetism in a van der waals crystal down to the monolayer limit. *Nature*, 546, 03 2017.

[103] Bevin Huang, Genevieve Clark, Dahlia Klein, David MacNeill, Efrén Navarro-Moratalla, Kyle Seyler, Nathan Wilson, Michael McGuire, David Cobden, Xiao di, Wang Yao, Pablo Jarillo-Herrero, and Xiaodong Xu. Electrical control of 2d magnetism in bilayer cri3. *Nature Nanotechnology*, 13, 07 2018.

[104] Shengwei Jiang, Lizhong Li, Zefang Wang, Kin Mak, and Jie Shan. Controlling magnetism in 2d cri3 by electrostatic doping. *Nature Nanotechnology*, 13, 07 2018.

[105] Dante J. O'Hara, Tiancong Zhu, Amanda H. Trout, Adam S. Ahmed, Yunqiu Kelly Luo, Choong Hee Lee, Mark R. Brenner, Siddharth Rajan, Jay A. Gupta, David W. McComb, and Roland K. Kawakami. Room temperature intrinsic ferromagnetism in epitaxial manganese selenide films in the monolayer limit. *Nano Letters*, 18(5):3125–3131, 2018. PMID: 29608316.

[106] Min Kan, Subash Adhikari, and Qiang Sun. Ferromagnetism in mnx2 (x = s, se) monolayers. *Phys. Chem. Chem. Phys.*, 16:4990–4994, 2014.

[107] Xingxing Li and Jinlong Yang. Crxte3 (x = si, ge) nanosheets: two dimensional intrinsic ferromagnetic semiconductors. *J. Mater. Chem. C*, 2:7071–7076, 2014.

[108] Cheng Gong, Lin Li, Zhenglu Li, Huiwen Ji, Alex Stern, Yang Xia, Ting Cao, Wei Bao, Chenzhe Wang, Yuan Wang, Z. Qiu, R. Cava, Steven Louie, Jing Xia, and Xiang Zhang. Discovery of intrinsic ferromagnetism in 2d van der waals crystals. 03 2017.

[109] Klaus Zollner, Paulo Faria Junior, and Jaroslav Fabian. Proximity exchange effects in mose 2 and wse 2 heterostructures with cri 3 : Twist angle, layer, and gate dependence. *Physical Review B*, 100, 08 2019.

[110] Jiayong Zhang, Bao Zhao, Tong Zhou, Yang Xue, Chunlan Ma, and Zhongqin Yang. Strong magnetization and chern insulators in compressed graphene/cri_3 van der waals heterostructures. *Phys. Rev. B*, 97:085401, Feb 2018.

[111] N. Levy, S. A. Burke, K. L. Meaker, M. Panlasigui, A. Zettl, F. Guinea, A. H. Castro Neto, and M. F. Crommie. Strain-induced pseudo–magnetic fields greater than 300 tesla in graphene nanobubbles. *Science*, 329(5991):544–547, 2010.

[112] Jiayong Zhang, Bao Zhao, Yugui Yao, and Zhongqin Yang. Robust quantum anomalous hall effect in graphene-based van der waals heterostructures. *Phys. Rev. B*, 92:165418, Oct 2015.

[113] Peng Wei, Sunwoo Lee, Florian Lemaitre, Lucas Pinel, Davide Cutaia, Wujoon Cha, Ferhat Katmis, Yu Zhu, Donald Heiman, James Hone, Jagadeesh Moodera, and Ching-Tzu Chen. Strong interfacial exchange field in the graphene/eus heterostructure. *Nature materials*, 15, 03 2016.

[114] Zhenhua Qiao, Shengyuan Yang, Wanxiang Feng, Wang-Kong Tse, Jun Ding, Yugui Yao, Jian Wang, and Qian Niu. Quantum anomalous hall effect in graphene from rashba and exchange effects. *Physical Review B*, 82:161414, 09 2010.

[115] Meng Wu, Zhenglu Li, Ting Cao, and Steven Louie. Physical origin of giant excitonic and magneto-optical responses in two-dimensional ferromagnetic insulators. *Nature Communications*, 10, 05 2019.

[116] J. W. Davenport, R. E. Watson, and M. Weinert. Linear augmented-slater-type-orbital method for electronic-structure calculations. v. spin-orbit splitting in cu_3au. *Phys. Rev. B*, 37:9985–9992, Jun 1988.

[117] Mingxing Chen and M. Weinert. Layer k-projection and unfolding electronic bands at interfaces. *Phys. Rev. B*, 98:245421, Dec 2018.

[118] P Nigge, Amy Qu, Étienne Lantagne-Hurtubise, E Mårsell, Stefan Link, G. Tom, M. Zonno, M. Michiardi, M. Schneider, Sergey Zhdanovich, G. Levy, Ulrich Starke, Christopher Gutiérrez, D. A. Bonn, Sarah A Burke, Marcel Franz, and Andrea Damascelli. Room temperature strain-induced landau levels in graphene on a wafer-scale platform. *Science Advances*, 5, 2019.

[119] V P Gusynin, S G Sharapov, and J P Carbotte. Magneto-optical conductivity in graphene. *Journal of Physics: Condensed Matter*, 19(2):026222, dec 2006.

[120] George W. Hanson. Quasi-transverse electromagnetic modes supported by a graphene parallel-plate waveguide. *Journal of Applied Physics*, 104(8):084314, 2008.

[121] R.E. Camley. Nonreciprocal surface waves. *Surface Science Reports*, 7(3):103–187, 1987.

[122] D. B. Mast, A. J. Dahm, and A. L. Fetter. Observation of bulk and edge magnetoplasmons in a two-dimensional electron fluid. *Phys. Rev. Lett.*, 54:1706–1709, Apr 1985.

[123] Weihua Wang, Peter Apell, and Jari Kinaret. Edge plasmons in graphene nanostructures. *Phys. Rev. B*, 84:085423, Aug 2011.

[124] Mário G. Silveirinha. Chern invariants for continuous media. *Phys. Rev. B*, 92:125153, Sep 2015.

[125] S. Ali Hassani Gangaraj, Mário G. Silveirinha, and George W. Hanson. Berry phase, berry connection, and chern number for a continuum bianisotropic material from a classical electromagnetics perspective. *IEEE Journal on Multiscale and Multiphysics Computational Techniques*, 2:3–17, 2017.

[126] Seyyed Ali Hassani Gangaraj, Andrei M. Nemilentsau, and George W. Hanson. The effects of three-dimensional defects on one-way surface plasmon propagation for photonic topological insulators comprised of continuum media. *Scientific Reports*, 6, 2016.

[127] Akihiro Okamoto, Ryuichi Shindou, and Shuichi Murakami. Berry curvature for coupled waves of magnons and electromagnetic waves. *Phys. Rev. B*, 102:064419, Aug 2020.

[128] S. Ali Hassani Gangaraj and Francesco Monticone. Physical violations of the bulk-edge correspondence in topological electromagnetics. *Phys. Rev. Lett.*, 124:153901, Apr 2020.

[129] S. Ali Hassani Gangaraj, George W. Hanson, Mário G. Silveirinha, Kunal Shastri, Mauro Antezza, and Francesco Monticone. Unidirectional and diffractionless surface plasmon polaritons on three-dimensional nonreciprocal plasmonic platforms. *Phys. Rev. B*, 99:245414, Jun 2019.

[130] Samaneh Pakniyat, Alexander M. Holmes, George W. Hanson, S. Ali Hassani Gangaraj, Mauro Antezza, Mário G. Silveirinha, Shahrokh Jam, and Francesco Monticone. Non-reciprocal, robust surface plasmon polaritons on gyrotropic interfaces. *IEEE Transactions on Antennas and Propagation*, 68(5):3718–3729, 2020.

[131] S. Pakniyat, Y. Liang, Y. Xiang, C. Cen, J. Chen, and G. W. Hanson. Indium antimonide—constraints on practicality as a magneto-optical platform for topological surface plasmon polaritons. *Journal of Applied Physics*, 128(18):183101, 2020.

[132] Yi Liang, Samaneh Pakniyat, Yinxiao Xiang, Jun Chen, Fan Shi, George W. Hanson, and Cheng Cen. Tunable unidirectional surface plasmon polaritons at the interface between gyrotropic and isotropic conductors. *Optica*, 8(7):952–959, Jul 2021.

[133] George W. Hanson, Seyyed Ali Hassani Gangaraj, and Andrei M. Nemilentsau. *Unidirectional, Defect-Immune, and Topologically Protected Electromagnetic Surface Waves*, pages 569–604. Springer International Publishing, Cham, 2018.

[134] Seyyed Ali Hassani Gangaraj and George W. Hanson. Momentum-space topological effects of nonreciprocity. *IEEE Antennas and Wireless Propagation Letters*, 17(11):1988–1992, 2018.

[135] Kunal Shastri, Mohamed Ismail Abdelrahman, and Francesco Monticone. Nonreciprocal and topological plasmonics. *Photonics*, 8(4), 2021.

[136] Francesco Monticone. A truly one-way lane for surface plasmon polaritons. *Nature Photonics*, 14:461–465, 08 2020.

[137] Yasuhiro Hatsugai. Chern number and edge states in the integer quantum hall effect. *Phys. Rev. Lett.*, 71:3697–3700, Nov 1993.

[138] Scott A. Skirlo, Ling Lu, and Marin Soljačić. Multimode one-way waveguides of large chern numbers. *Phys. Rev. Lett.*, 113:113904, Sep 2014.

[139] Wenlong Gao, Mark Lawrence, Biao Yang, Fu Liu, Fengzhou Fang, Benjamin Béri, Jensen Li, and Shuang Zhang. Topological photonic phase in chiral hyperbolic metamaterials. *Phys. Rev. Lett.*, 114:037402, Jan 2015.

[140] F. D. M. Haldane and S. Raghu. Possible realization of directional optical waveguides in photonic crystals with broken time-reversal symmetry. *Phys. Rev. Lett.*, 100:013904, Jan 2008.

[141] S. Raghu and F. D. M. Haldane. Analogs of quantum-hall-effect edge states in photonic crystals. *Phys. Rev. A*, 78:033834, Sep 2008.

[142] Ling Lu, John Joannopoulos, and Marin Soljačić. Topological photonics. *Nature Photonics*, 8, 08 2014.

[143] Mário G. Silveirinha. Bulk-edge correspondence for topological photonic continua. *Phys. Rev. B*, 94:205105, Nov 2016.

[144] Mário G. Silveirinha. Proof of the bulk-edge correspondence through a link between topological photonics and fluctuation-electrodynamics. *Phys. Rev. X*, 9:011037, Feb 2019.

[145] C. Tauber, P. Delplace, and A. Venaille. Anomalous bulk-edge correspondence in continuous media. *Phys. Rev. Research*, 2:013147, Feb 2020.

[146] Mohammad Hafezi, Eugene Demler, Mikhail Lukin, and Jacob Taylor. Robust optical delay lines via topological protection. *Nature Physics*, 7, 02 2011.

[147] S. U. Piatrusha, E. S. Tikhonov, Z. D. Kvon, N. N. Mikhailov, S. A. Dvoretsky, and V. S. Khrapai. Topological protection brought to light by the time-reversal symmetry breaking. *Phys. Rev. Lett.*, 123:056801, Jul 2019.

[148] Zeki Hayran, Ali Hassani Gangaraj, and Francesco Monticone. Topologically protected broadband rerouting of propagating waves around complex objects. *Nanophotonics*, 8:1371–1378, 05 2019.

[149] S Ali Hassani Gangaraj and Francesco Monticone. Topologically-protected one-way leaky waves in nonreciprocal plasmonic structures. *Journal of Physics: Condensed Matter*, 30(10):104002, feb 2018.

[150] B. R. Vishvakarma and Devi Chadha. The surface wave concept in circulator design. *International Journal of Electronics*, 47(1):89–95, 1979.

[151] Zheng Wang, Yidong Chong, John Joannopoulos, and Marin Soljacić. Observation of unidirectional backscattering-immune topological electromagnetic states. *Nature*, 461:772–5, 10 2009.

[152] Yin Poo, Rui-xin Wu, Zhifang Lin, Yan Yang, and C. T. Chan. Experimental realization of self-guiding unidirectional electromagnetic edge states. *Phys. Rev. Lett.*, 106:093903, Mar 2011.

[153] Wen-Jie Chen, Shao-Ji Jiang, Xiao-Dong Chen, Jian-Wen Dong, and Che Chan. Experimental realization of photonic topological insulator in a uniaxial metacrystal waveguide. *Nature communications*, 5, 01 2014.

[154] Scott A. Skirlo, Ling Lu, Yuichi Igarashi, Qinghui Yan, John Joannopoulos, and Marin Soljačić. Experimental observation of large chern numbers in photonic crystals. *Phys. Rev. Lett.*, 115:253901, Dec 2015.

[155] Li He, Zachariah Addison, Jicheng Jin, Eugene Mele, Steven Johnson, and Bo Zhen. Floquet chern insulators of light. *Nature Communications*, 10:1–6, 09 2019.

[156] A Hartstein, E Burstein, A A Maradudin, R Brewer, and R F Wallis. Surface polaritons on semi-infinite gyromagnetic media. *Journal of Physics C: Solid State Physics*, 6(7):1266–1276, apr 1973.

[157] D.M. Pozar. *Microwave Engineering, 4th Edition*. Wiley, 2011.

[158] L. Landau and E. Lifshitz. On the theory of the dispersion of magnetic permeability in ferromagnetic bodies. *Phys. Z. Sowjetunion*, 8, 01 1992.

[159] Vinod V K Thalakkatukalathil. *Electromagnetic modeling and characterization of anisotropic ferrite materials for microwave Isolators/Circulators*. Theses, Université de Bretagne occidentale - Brest, December 2017.

[160] Hsin Yu Yao, Wei-Chen Chang, Li-Wen Chang, and Tsun-Hsu Chang. Theoretical and experimental investigation of ferrite-loaded waveguide for ferrimagnetism characterization. *Progress In Electromagnetics Research C*, 90:195–208, 01 2019.

[161] T.J. Gerson and J.S. Nadan. Surface electromagnetic modes of a ferrite slab. *IEEE Transactions on Microwave Theory and Techniques*, 22(8):757–763, 1974.

[162] E. Cojocaru. Modes in dielectric or ferrite gyrotropic slab and circular waveguides, longitudinally magnetized, with open and completely or partially filled wall. *J. Opt. Soc. Am. B*, 27(10):1965–1977, Oct 2010.

[163] Alexander L. Fetter. Edge magnetoplasmons in a bounded two-dimensional electron fluid. *Phys. Rev. B*, 32:7676–7684, Dec 1985.

[164] Weihua Wang, Jari M. Kinaret, and S. Peter Apell. Excitation of edge magnetoplasmons in semi-infinite graphene sheets: Temperature effects. *Phys. Rev. B*, 85:235444, Jun 2012.

Appendix

A.1 Scattered fields above and below a magneto-plasma slab

The incident field excited by an impressed electric dipole current source $\mathbf{J}_e^i = \mathbf{J}_0 \delta(\mathbf{r} - \mathbf{r}_0)$ suspended a distance d above the first interface in the air/freespace region, is given by

$$\mathbf{E}(\mathbf{r}) = \left(\nabla\nabla + \bar{\mathbf{I}} k_0\right) \cdot \pi(\mathbf{r}) \tag{A.1}$$

where (see Sec. 1.2 for additional details)

$$\pi(\mathbf{r}) = g(\mathbf{r}, \mathbf{r}_0) \frac{\mathbf{J}_0}{-i\omega\varepsilon_0} \tag{A.2}$$

denotes the principal Hertzian potential due to the dipole source, defined in terms of the scalar Green's function $g(\mathbf{r}, \mathbf{r}_0) = e^{ik_0|\mathbf{r}-\mathbf{r}_0|}/4\pi|\mathbf{r} - \mathbf{r}_0|$ where $\mathbf{r}_0 = (0, 0, d)$. Following [47], the scattered fields may be written in the Fourier transform domain with respect to k_x and k_y,

$$\mathbf{E}^r(\mathbf{r}) = \frac{1}{4\pi^2} \int d\mathbf{q} e^{i\mathbf{q}\cdot(\mathbf{r}-\mathbf{r}_0)} \frac{e^{-\gamma_0(d+z)}}{2\gamma_0} \bar{\mathbf{C}}^r(\mathbf{q}) \cdot \frac{\mathbf{J}_0}{-i\omega\varepsilon_0}\ , \tag{A.3}$$

$$\mathbf{E}^t(\mathbf{r}) = \frac{1}{4\pi^2} \int d\mathbf{q} e^{i\mathbf{q}\cdot(\mathbf{r}-\mathbf{r}_0)} \frac{e^{-\gamma_0(d-z)}}{2\gamma_0} \bar{\mathbf{C}}^t(\mathbf{q}) \cdot \frac{\mathbf{J}_0}{-i\omega\varepsilon_0}\ , \tag{A.4}$$

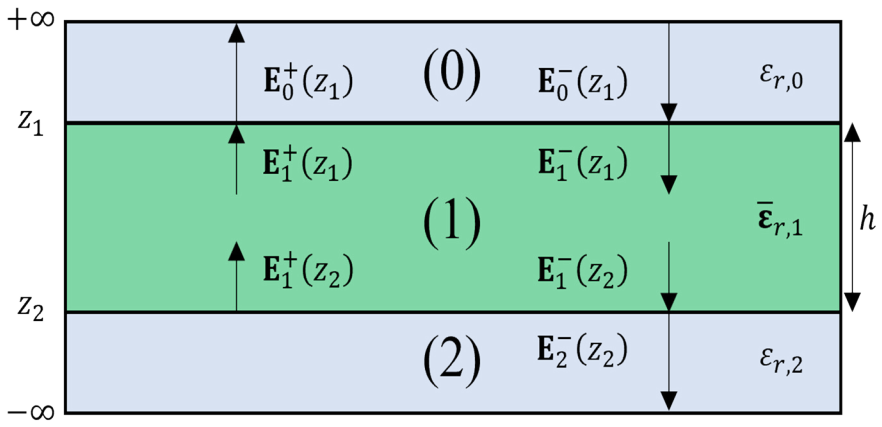

Figure A-1: Cross-sectional view of the slab shown in Fig. 2-1(a). The upper and lower interfaces are positioned at $z = z_1$ and $z = z_2$ respectively. Regions (0) and (2) are characterized by an isotropic relative (scalar) permittivity ϵ_r, while region (1) is characterized by a gyrotropic permittivity tensor $\bar{\epsilon}_r$ defined in Eqs. (2.1)-(2.2). The Fourier coefficients associated with the incident and scattered fields are shown in each region, propagating in the $\pm z$ directions.

where

$$\bar{\mathbf{C}}^r(\mathbf{q}) = \left(\bar{\mathbf{I}}_{\parallel} - \frac{\hat{\mathbf{z}}\mathbf{q}}{i\gamma_0}\right) \cdot \bar{\mathbf{R}} \cdot \left(k_0^2 \bar{\mathbf{I}}_s - \mathbf{q}\mathbf{q} + i\gamma_0 \mathbf{q}\hat{\mathbf{z}}\right) \ , \tag{A.5}$$

$$\bar{\mathbf{C}}^t(\mathbf{q}) = \left(\bar{\mathbf{I}}_{\parallel} + \frac{\hat{\mathbf{z}}\mathbf{q}}{i\gamma_0}\right) \cdot \bar{\mathbf{T}} \cdot \left(k_0^2 \bar{\mathbf{I}}_s - \mathbf{q}\mathbf{q} + i\gamma_0 \mathbf{q}\hat{\mathbf{z}}\right) \ , \tag{A.6}$$

such that $\bar{\mathbf{I}}_{\parallel} = \hat{\mathbf{x}}\hat{\mathbf{x}} + \hat{\mathbf{y}}\hat{\mathbf{y}}$ and $\gamma_0 = \sqrt{k_x^2 + k_y^2 - k_0^2}$.

In what follows, we derive the plane wave reflection and transmission coefficients, $\bar{\mathbf{R}}(\omega, \mathbf{k}_s)$ and $\bar{\mathbf{T}}(\omega, \mathbf{k}_s)$, which relate the tangential field components of the electric field reflected and transmitted from a gyrotropic slab of finite thickness, as shown in Fig. A-1. As in [47], it is important to define a convenient, orthogonal coordinate system in which to expand the amplitude vector of a plane wave propagating in the gyrotropic medium. The set of orthogonal unit vectors which span this coordinate system is given by $\left\{\hat{\mathbf{k}}_{t,j}^{\pm}, \hat{\mathbf{y}}, \hat{\mathbf{k}}_{t,j}^{\pm} \times \hat{\mathbf{y}}\right\}$, where $\hat{\mathbf{k}}_{t,j}^{\pm} = \hat{\mathbf{x}}k_x \pm \hat{\mathbf{z}}i\gamma_j$ for $j \in \{1, 2\}$. The fields above and below the interface are expanded in terms of the Cartesian basis $\{\hat{\mathbf{x}}, \hat{\mathbf{y}}, \hat{\mathbf{z}}\}$. The relationship between the tangential electric and

magnetic fields in the structure is

$$\begin{pmatrix} \omega\mu_0 H_y^{\pm} \\ \omega\mu_0 H_x^{\pm} \end{pmatrix} = \left\{ \bar{\mathbf{Y}}^{\pm}, \bar{\mathbf{Y}}_g^{\pm} \right\} \cdot \begin{pmatrix} E_x^{\pm} \\ E_y^{\pm} \end{pmatrix} , \tag{A.7}$$

where $\bar{\mathbf{Y}}^{\pm}$ relates the electric and magnetic fields in the dielectric regions above and below the slab, and $\bar{\mathbf{Y}}_g^{\pm}$ relates the electric and magnetic fields within the slab. These tensors are given by

$$\bar{\mathbf{Y}}^{\pm} = \frac{\pm 1}{i\gamma_0} \begin{pmatrix} k_x^2 - \gamma_0^2 & k_x k_y \\ -k_x k_y & \gamma_0^2 - k_y^2 \end{pmatrix} , \tag{A.8}$$

$$\bar{\mathbf{Y}}_g^{\pm} = \begin{pmatrix} -\delta_1 k_{t,1}^2 & -\delta_2 k_{t,2}^2 \\ k_y \phi_1^{\pm} & k_y \phi_2^{\pm} \end{pmatrix} \cdot \begin{pmatrix} \beta_1^{\pm} & \beta_2^{\pm} \\ k_y \theta_1 & k_y \theta_2 \end{pmatrix}^{-1} . \tag{A.9}$$

Matching the tangential components of the electric and magnetic fields at each interface, we obtain

$$\left(\bar{\mathbf{I}}_s + \bar{\mathbf{R}}_{01}\right) \cdot \mathbf{E}_0^- (z_1) = \bar{\mathbf{T}}_{01} \cdot \mathbf{E}_0^- (z_1) , \tag{A.10}$$

$$\left(\bar{\mathbf{I}}_s + \bar{\mathbf{R}}_{10}\right) \cdot \mathbf{E}_1^+ (z_1) = \bar{\mathbf{T}}_{10} \cdot \mathbf{E}_1^+ (z_1) , \tag{A.11}$$

$$\left(\bar{\mathbf{I}}_s + \bar{\mathbf{R}}_{12}\right) \cdot \mathbf{E}_1^- (z_2) = \bar{\mathbf{T}}_{12} \cdot \mathbf{E}_1^- (z_2) , \tag{A.12}$$

$$\left(\bar{\mathbf{Y}}^- + \bar{\mathbf{Y}}^+ \cdot \bar{\mathbf{R}}_{01}\right) \cdot \mathbf{E}_0^- (z_1) = \bar{\mathbf{Y}}_g^- \cdot \bar{\mathbf{T}}_{01} \cdot \mathbf{E}_0^- (z_1) , \tag{A.13}$$

$$\left(\bar{\mathbf{Y}}_g^+ + \bar{\mathbf{Y}}_g^- \cdot \bar{\mathbf{R}}_{10}\right) \cdot \mathbf{E}_1^+ (z_1) = \bar{\mathbf{Y}}^+ \cdot \bar{\mathbf{T}}_{10} \cdot \mathbf{E}_1^+ (z_1) , \tag{A.14}$$

$$\left(\bar{\mathbf{Y}}_g^- + \bar{\mathbf{Y}}_g^+ \cdot \bar{\mathbf{R}}_{12}\right) \cdot \mathbf{E}_1^- (z_2) = \bar{\mathbf{Y}}^- \cdot \bar{\mathbf{T}}_{12} \cdot \mathbf{E}_1^- (z_2) . \tag{A.15}$$

where

$$\bar{\mathbf{R}}_{nn'} = \left(\bar{\mathbf{Y}}^{m_1} - \bar{\mathbf{Y}}_g^{m_2}\right)^{-1} \cdot \left(\bar{\mathbf{Y}}_g^{m_3} - \bar{\mathbf{Y}}^{m_3}\right) , \tag{A.16}$$

such that

$$(m_1, m_2, m_3) = \begin{cases} (+,-,-) & (n,n') = (0,1) \\ (+,-,+) & (n,n') = (1,0) \\ (-,+,-) & (n,n') = (1,2) \end{cases} , \tag{A.17}$$

and from (A.10)-(A.15), it follows that $\bar{\mathbf{T}}_{nn'} = \bar{\mathbf{I}}_s + \bar{\mathbf{R}}_{nn'}$. Furthermore, it is important to note the relations,

$$\mathbf{E}_1^- (z_1) = \bar{\mathbf{T}}_{01} \cdot \mathbf{E}_0^- (z_1) + \bar{\mathbf{R}}_{10} \cdot \mathbf{E}_1^+ (z_1) \ , \tag{A.18}$$

$$\mathbf{E}_0^+ (z_1) = \bar{\mathbf{R}}_{01} \cdot \mathbf{E}_0^- (z_1) + \bar{\mathbf{T}}_{10} \cdot \mathbf{E}_1^+ (z_1) \ , \tag{A.19}$$

$$\mathbf{E}_1^+ (z_2) = \bar{\mathbf{R}}_{12} \cdot \mathbf{E}_1^- (z_2) \ , \tag{A.20}$$

$$\mathbf{E}_2^- (z_2) = \bar{\mathbf{T}}_{12} \cdot \mathbf{E}_1^- (z_2) \ , \tag{A.21}$$

where the electric field associated with a plane wave propagating a distance, $h = |z_2 - z_1|$, along the $\pm z$ direction within the gyrotropic slab, is given by

$$\mathbf{E}_1^+ (z_1) = \bar{\mathbf{P}}^+ \cdot \mathbf{E}_1^+ (z_2) \ , \tag{A.22}$$

$$\mathbf{E}_1^- (z_2) = \bar{\mathbf{P}}^- \cdot \mathbf{E}_1^- (z_1) \ , \tag{A.23}$$

where $\bar{\mathbf{P}}^{\pm}$ denotes the spacial propagator that effectively propagates the electric field a distance h through the slab and takes the form

$$\bar{\mathbf{P}}^{\pm} = \bar{\mathbf{U}}_{\pm} \cdot \bar{\mathbf{P}} \cdot \bar{\mathbf{U}}_{\pm}^{-1} \tag{A.24}$$

where

$$\bar{\mathbf{U}}_{\pm} = \begin{pmatrix} \beta_1^{\pm}/k_{t,1} & \beta_2^{\pm}/k_{t,2} \\ k_y\theta_1/k_{t,1} & k_y\theta_2/k_{t,2} \end{pmatrix} \ , \quad \bar{\mathbf{P}} = \begin{pmatrix} e^{-\gamma_1 h} & 0 \\ 0 & e^{-\gamma_2 h} \end{pmatrix} \ . \tag{A.25}$$

Using (A.22)-(A.23) in (A.18)-(A.21) leads to

$$\mathbf{E}_0^+(z_1) = \bar{\mathbf{R}} \cdot \mathbf{E}_0^-(z_1) \ , \tag{A.26}$$

$$\mathbf{E}_2^-(z_2) = \bar{\mathbf{T}} \cdot \mathbf{E}_0^-(z_1) \ , \tag{A.27}$$

where

$$\bar{\mathbf{R}} = \bar{\mathbf{R}}_{01} + \bar{\mathbf{T}}_{10} \cdot \bar{\mathbf{R}}'_{12} \cdot \left(\bar{\mathbf{I}}_s - \bar{\mathbf{R}}_{10} \cdot \bar{\mathbf{R}}'_{12}\right)^{-1} \cdot \bar{\mathbf{T}}_{01} \ , \tag{A.28}$$

$$\bar{\mathbf{T}} = \bar{\mathbf{T}}_{12} \cdot \bar{\mathbf{P}}^- \cdot \left(\bar{\mathbf{I}}_s - \bar{\mathbf{R}}_{10} \cdot \bar{\mathbf{R}}'_{12}\right)^{-1} \cdot \bar{\mathbf{T}}_{01} \ , \tag{A.29}$$

such that $\bar{\mathbf{R}}'_{12} = \bar{\mathbf{P}}^+ \cdot \bar{\mathbf{R}}_{12} \cdot \bar{\mathbf{P}}^-$. Finally, after some algebra, it can be shown that (A.16), (A.24), (A.28), and (A.29) may be written in quotient form as

$$\bar{\mathbf{R}}_{nn'} = \frac{1}{\Omega^{nn'}} \begin{pmatrix} \Pi_{11}^{nn'} & \Pi_{12}^{nn'}/k_y \\ k_y \Pi_{21}^{nn'} & \Pi_{22}^{nn'} \end{pmatrix} \ , \quad \bar{\mathbf{P}}^{\pm} = \frac{1}{\chi^{\pm}} \begin{pmatrix} \Delta_{11}^{\pm} & \Delta_{12}^{\pm}/k_y \\ k_y \Delta_{21}^{\pm} & \Delta_{22}^{\pm} \end{pmatrix} \ , \tag{A.30}$$

$$\bar{\mathbf{R}} = \frac{1}{\Lambda\Omega^{01}} \begin{pmatrix} \Xi_{11} & \Xi_{12}/k_y \\ k_y \Xi_{21} & \Xi_{22} \end{pmatrix} \ , \quad \mathbf{T} = \frac{\Omega^{10}\chi^+}{\Lambda\Omega^{01}} \begin{pmatrix} \Psi_{11} & \Psi_{12}/k_y \\ k_y \Psi_{21} & \Psi_{22} \end{pmatrix} \ , \tag{A.31}$$

where

$$\Omega^{nn'} = m_1 m_3 \gamma_0 \chi^{m_3} \left(Q_E^{m_2} - \varepsilon_r \chi^{m_2}\right) + m_3 \chi^{m3} \left[\left(k_y^2 - \gamma_0^2\right) Q_A + k_x k_y^2 Q_C^{m_2}\right] \tag{A.32}$$

$$- m_3 \chi^{m3} \left[\left(k_x^2 - \gamma_0^2\right) Q_D^{m_2} + k_x Q_B^{m_2}\right] \ , \tag{A.33}$$

$$\Pi_{11}^{nn'} = \gamma_0 \left[\varepsilon_r \chi^{m_2} \chi^{m_3} + m_1 m_3 k_0^2 \left(Q_A Q_D^{m_2} - Q_C^{m_3} Q_B^{m_2}\right)\right] \tag{A.34}$$

$$- m_3 \chi^{m_2} \left[\left(k_y^2 - \gamma_0^2\right) Q_A + k_x k_y^2 Q_C^{m_3}\right] + m_1 \chi^{m_3} \left[\left(k_x^2 - \gamma_0^2\right) Q_D^{m_2} + k_x Q_B^{m_2}\right] \ , \tag{A.35}$$

$$\Pi_{12}^{nn'} = m_1 m_3 \gamma_0 k_0^2 \left(Q_D^{m_2} Q_B^{m_3} - Q_D^{m_3} Q_B^{m_2}\right) \tag{A.36}$$

$$+ k_x k_y^2 \left(m_1 \chi^{m_3} Q_D^{m_2} - m_3 \chi^{m_2} Q_D^{m_3}\right) + \left(k_y^2 - \gamma_0^2\right) \left(m_1 \chi^{m_3} Q_B^{m_2} - m_3 \chi^{m_2} Q_B^{m_3}\right) \ , \tag{A.37}$$

$$\Pi_{21}^{nn'} = m_1 m_3 \gamma_0 k_0^2 \left(Q_A Q_C^{m_3} - Q_A Q_C^{m_2}\right) \tag{A.38}$$

$$- k_x \left(m_1 \chi^{m_3} Q_A - m_3 \chi^{m_2} Q_A\right) - \left(k_x^2 - \gamma_0^2\right) \left(m_1 \chi^{m_3} Q_C^{m_2} - m_3 \chi^{m_2} Q_C^{m_3}\right) \ , \tag{A.39}$$

$$\Pi_{22}^{nn'} = \gamma_0 \left[\varepsilon_r \chi^{m_2} \chi^{m_3} + m_1 m_3 k_0^2 \left(Q_A Q_D^{m_3} - Q_C^{m_2} Q_B^{m_3}\right)\right] \tag{A.40}$$

$$- m_1 \chi^{m_3} \left[\left(k_y^2 - \gamma_0^2\right) Q_A + k_x k_y^2 Q_C^{m_2}\right] + m_3 \chi^{m_2} \left[\left(k_x^2 - \gamma_0^2\right) Q_D^{m_3} + k_x Q_B^{m_3}\right] \ , \tag{A.41}$$

and

$$\Delta_{11}^{\pm} = k_{t,1}^2 \xi_1 \varpi_2 \alpha_2^{\pm} e^{-\gamma_{z,2} h} - k_{t,2}^2 \xi_2 \varpi_1 \alpha_1^{\pm} e^{-\gamma_{z,1} h} \ , \tag{A.42}$$

$$\Delta_{12}^{\pm} = \varpi_1 \varpi_2 \alpha_1^{\pm} \alpha_2^{\pm} \left(e^{-\gamma_{z,2} h} - e^{-\gamma_{z,1} h}\right) \ , \tag{A.43}$$

$$\Delta_{21} = k_{t,1}^2 k_{t,2}^2 \xi_1 \xi_2 \left(e^{-\gamma_{z,1} h} - e^{-\gamma_{z,2} h}\right) \ , \tag{A.44}$$

$$\Delta_{22}^{\pm} = k_{t,1}^2 \xi_1 \varpi_2 \alpha_2^{\pm} e^{-\gamma_{z,1} h} - k_{t,2}^2 \xi_2 \varpi_1 \alpha_1^{\pm} e^{-\gamma_{z,2} h} \ , \tag{A.45}$$

and

$$\Xi_{11} = \Lambda \Pi_{11}^{01} + \Pi_{12}^{10} \left(\Upsilon_{21} \Sigma_{11} + \Upsilon_{22} \Sigma_{21}\right) + \left(\Omega^{10} + \Pi_{11}^{10}\right) \left(\Upsilon_{11} \Sigma_{11} + \Upsilon_{12} \Sigma_{21}\right) \ , \tag{A.46}$$

$$\Xi_{12} = \Lambda \Pi_{12}^{01} + \Pi_{12}^{10} \left(\Upsilon_{21} \Sigma_{12} + \Upsilon_{22} \Sigma_{22}\right) + \left(\Omega^{10} + \Pi_{11}^{10}\right) \left(\Upsilon_{11} \Sigma_{12} + \Upsilon_{12} \Sigma_{22}\right) \ , \tag{A.47}$$

$$\Xi_{21} = \Lambda \Pi_{21}^{01} + \Pi_{21}^{10} \left(\Upsilon_{11} \Sigma_{11} + \Upsilon_{12} \Sigma_{21}\right) + \left(\Omega^{10} + \Pi_{22}^{10}\right) \left(\Upsilon_{21} \Sigma_{11} + \Upsilon_{22} \Sigma_{21}\right) \ , \tag{A.48}$$

$$\Xi_{22} = \Lambda \Pi_{22}^{01} + \Pi_{21}^{10} \left(\Upsilon_{11} \Sigma_{12} + \Upsilon_{12} \Sigma_{22}\right) + \left(\Omega^{10} + \Pi_{22}^{10}\right) \left(\Upsilon_{21} \Sigma_{12} + \Upsilon_{22} \Sigma_{22}\right) \ , \tag{A.49}$$

and

$$\Psi_{11} = \Pi_{12}^{12}\left(\Delta_{21}\Sigma_{11} + \Delta_{22}^{-}\Sigma_{21}\right) + \left(\Omega^{12} + \Pi_{11}^{12}\right)\left(\Delta_{11}^{-}\Sigma_{11} + \Delta_{12}^{-}\Sigma_{21}\right) \ , \tag{A.50}$$

$$\Psi_{12} = \Pi_{12}^{12}\left(\Delta_{21}\Sigma_{12} + \Delta_{22}^{-}\Sigma_{22}\right) + \left(\Omega^{12} + \Pi_{11}^{12}\right)\left(\Delta_{11}^{-}\Sigma_{12} + \Delta_{12}^{-}\Sigma_{22}\right) \ , \tag{A.51}$$

$$\Psi_{21} = \Pi_{21}^{12}\left(\Delta_{11}^{-}\Sigma_{11} + \Delta_{12}^{-}\Sigma_{21}\right) + \left(\Omega^{12} + \Pi_{22}^{12}\right)\left(\Delta_{21}\Sigma_{11} + \Delta_{22}^{-}\Sigma_{21}\right) \ , \tag{A.52}$$

$$\Psi_{22} = \Pi_{21}^{12}\left(\Delta_{11}^{-}\Sigma_{12} + \Delta_{12}^{-}\Sigma_{22}\right) + \left(\Omega^{12} + \Pi_{22}^{12}\right)\left(\Delta_{21}\Sigma_{12} + \Delta_{22}^{-}\Sigma_{22}\right) \ , \tag{A.53}$$

and

$$\Lambda = \left(\Omega^{10}\Omega^{12}\chi^{+}\chi^{-} - \Theta_{11}\right)\left(\Omega^{10}\Omega^{12}\chi^{+}\chi^{-} - \Theta_{22}\right) - \Theta_{12}\Theta_{21} \ , \tag{A.54}$$

such that

$$\Upsilon_{11} = \Delta_{11}^{+}\left(\Pi_{11}^{12}\Delta_{11}^{-} + \Pi_{12}^{12}\Delta_{21}\right) + \Delta_{12}^{+}\left(\Pi_{21}^{12}\Delta_{11}^{-} + \Pi_{22}^{12}\Delta_{21}\right) \ , \tag{A.55}$$

$$\Upsilon_{12} = \Delta_{11}^{+}\left(\Pi_{11}^{12}\Delta_{12}^{-} + \Pi_{12}^{12}\Delta_{22}^{-}\right) + \Delta_{12}^{+}\left(\Pi_{21}^{12}\Delta_{12}^{-} + \Pi_{22}^{12}\Delta_{22}^{-}\right) \ , \tag{A.56}$$

$$\Upsilon_{21} = \Delta_{21}\left(\Pi_{11}^{12}\Delta_{11}^{-} + \Pi_{12}^{12}\Delta_{21}\right) + \Delta_{22}^{+}\left(\Pi_{21}^{12}\Delta_{11}^{-} + \Pi_{22}^{12}\Delta_{21}\right) \ , \tag{A.57}$$

$$\Upsilon_{22} = \Delta_{21}\left(\Pi_{11}^{12}\Delta_{12}^{-} + \Pi_{12}^{12}\Delta_{22}^{-}\right) + \Delta_{22}^{+}\left(\Pi_{21}^{12}\Delta_{12}^{-} + \Pi_{22}^{12}\Delta_{22}^{-}\right) \ , \tag{A.58}$$

and

$$\Theta_{11} = \Pi_{11}^{10}\Upsilon_{11} + \Pi_{12}^{10}\Upsilon_{21} \ , \tag{A.59}$$

$$\Theta_{12} = \Pi_{11}^{10}\Upsilon_{12} + \Pi_{12}^{10}\Upsilon_{22} \ , \tag{A.60}$$

$$\Theta_{21} = \Pi_{21}^{10}\Upsilon_{11} + \Pi_{22}^{10}\Upsilon_{21} \ , \tag{A.61}$$

$$\Theta_{22} = \Pi_{21}^{10}\Upsilon_{12} + \Pi_{22}^{10}\Upsilon_{22} \ , \tag{A.62}$$

and

$$\Sigma_{11} = \left(\Omega^{10}\Phi - \Theta_{22}\right)\left(\Omega^{01} + \Pi_{11}^{01}\right) + \Theta_{12}\Pi_{21}^{01} \ , \tag{A.63}$$

$$\Sigma_{12} = \left(\Omega^{10}\Phi - \Theta_{22}\right)\Pi_{12}^{01} + \Theta_{12}\left(\Omega^{01} + \Pi_{22}^{01}\right) \ , \tag{A.64}$$

$$\Sigma_{21} = \left(\Omega^{10}\Phi - \Theta_{11}\right)\Pi_{21}^{01} + \Theta_{21}\left(\Omega^{01} + \Pi_{11}^{01}\right) \ , \tag{A.65}$$

$$\Sigma_{22} = \left(\Omega^{10}\Phi - \Theta_{11}\right)\left(\Omega^{01} + \Pi_{22}^{01}\right) + \Theta_{21}\Pi_{12}^{01} \ , \tag{A.66}$$

and

$$Q_A = \varepsilon_g k_{t,1}^2 k_{t,2}^2 \left(\varpi_1\xi_2 - \varpi_2\xi_1\right) \ , \tag{A.67}$$

$$Q_B^{\pm} = \varepsilon_g \varpi_1\varpi_2 \left(k_{t,1}^2\alpha_2^{\pm} - k_{t,2}^2\alpha_1^{\pm}\right) \ , \tag{A.68}$$

$$Q_C^{\pm} = k_{t,1}^2\zeta_2^{\pm}\xi_1 - k_{t,2}^2\zeta_1^{\pm}\xi_2 \ , \tag{A.69}$$

$$Q_D^{\pm} = \zeta_2^{\pm}\alpha_1^{\pm}\varpi_1 - \zeta_1^{\pm}\alpha_2^{\pm}\varpi_2 \ , \tag{A.70}$$

$$Q_E^{\pm} = \varepsilon_g k_0^2 \left(k_{t,1}^2\zeta_2^{\pm}\varpi_1 - k_{t,2}^2\zeta_1^{\pm}\varpi_2\right) \ , \tag{A.71}$$

and

$$\zeta_j^{\pm} = \varepsilon_g k_x \varpi_j \pm \varepsilon_a \xi_i \gamma_{z,j} \ , \tag{A.72}$$

$$\alpha_j^{\pm} = k_x\xi_j \pm \varepsilon_g k_0^2 \gamma_{z,j} \ , \tag{A.73}$$

$$\chi^{\pm} = k_{t,1}^2\xi_1\varpi_2\alpha_2^{\pm} - k_{t,2}^2\xi_2\varpi_1\alpha_1^{\pm} \ , \tag{A.74}$$

and

$$\begin{gathered}
\beta_j^{\pm} = k_x \mp i\gamma_j\delta_j \ , \quad \phi_j^{\pm} = \delta_j k_x \mp i\gamma_j\left(\theta_j - 1\right) \ , \\
\delta_j = ik_0^2\varepsilon_g/\xi_j \ , \quad \theta_j = -k_{t,j}^2/\varpi_j \ , \quad \gamma_0 = \sqrt{k_x^2 + k_y^2 - k_0^2} \ , \\
\xi_j = k_0^2\varepsilon_t - k_{b,j}^2 \ , \quad \varpi_j = k_0^2\varepsilon_a - k_{t,j}^2 \ , \\
k_{t,j}^2 = k_x^2 - \gamma_j^2 \ , \quad k_{b,j}^2 = k_{t,j}^2 + k_y^2 \ .
\end{gathered} \tag{A.75}$$

Matlab code for the reflection and transmission coefficients is available on Code Ocean, DOI: 10.24433/CO.7785417.v1.

A.2 Dispersion of bulk SPP modes for a 2D plasma

In the following, we obtain the natural modes of the 2D/quasi-2D structure shown in Fig. 3-2(a). These modes are defined as a field configuration that exists in the absence of sources and satisfies the appropriate boundary conditions.

Above and below the interface, in the isotropic dielectric regions, Maxwell's equations in the absence of sources combine to form the wave equation for the electric and magnetic fields (i.e., the vector Helmholtz equation)

$$\nabla^2\boldsymbol{\Psi} + \omega^2\mu\varepsilon\boldsymbol{\Psi} = \nabla\nabla\cdot\boldsymbol{\Psi} \tag{A.76}$$

for $\boldsymbol{\Psi} \in \{\mathbf{E}, \mathbf{H}\}$ where $\nabla\cdot\boldsymbol{\Psi} = \mathbf{0}$. The general solutions to (A.76) in the spatial transform domain with respect to x, y are $\boldsymbol{\Psi}^m(\mathbf{q}, z) = \boldsymbol{\Psi}_0^m(\mathbf{q})\exp(ik_z^m z)$, where $\mathbf{q} = \hat{\mathbf{x}}q_x + \hat{\mathbf{y}}q_y$ is the in-plane wavevector preserved across the interface, $\boldsymbol{\Psi}_0^m \in \{\mathbf{E}_0^m, \mathbf{H}_0^m\}$ is the polarization, and $k_z^m = m\sqrt{k^2 - q^2}$ with $k^2 = \omega^2\mu\varepsilon$ and $m \in \{\pm\}$ used to indicate forward/backward propagation with respect to $\hat{\mathbf{z}}$.

Expanding $\mathbf{E}_0^m$ in a coordinate system spanned by the unit vectors $\{\hat{\mathbf{z}}, \hat{\mathbf{q}}, \hat{\mathbf{z}}\times\hat{\mathbf{q}}\}$, we have

$$\mathbf{E}_0^m = E_{\hat{\mathbf{q}}}^m\hat{\mathbf{q}} + E_{\hat{\mathbf{z}}}^m\hat{\mathbf{z}} + E_{\hat{\mathbf{z}}\times\hat{\mathbf{q}}}^m(\hat{\mathbf{z}}\times\hat{\mathbf{q}}) \ , \tag{A.77}$$

and choosing the tangential components $E_{\hat{\mathbf{q}}}^m$ and $E_{\hat{\mathbf{z}}\times\hat{\mathbf{q}}}^m$, it follows that $E_{\hat{\mathbf{z}}}^m = -qE_{\hat{\mathbf{q}}}^m/k_z^m$. The associated magnetic field polarization is obtained from Faraday's law as

$$\omega\mu\mathbf{H}_0^m = -k_z^m E_{\hat{\mathbf{z}}\times\hat{\mathbf{q}}}^m\hat{\mathbf{q}} + \frac{k^2}{k_z^m}E_{\hat{\mathbf{q}}}^m(\hat{\mathbf{z}}\times\hat{\mathbf{q}}) + qE_{\hat{\mathbf{z}}\times\hat{\mathbf{q}}}^m\hat{\mathbf{z}} \ . \tag{A.78}$$

From (A.77) and (A.78), it is straightforward to recover the relation $\hat{\mathbf{z}}\times\mathbf{H}_{0\|}^m = m\bar{\bar{\mathbf{Y}}}\cdot\mathbf{E}_{0\|}^m$,

where $\mathbf{E}_{0\|}^{m}, \mathbf{H}_{0\|}^{m}$ are the tangential components of the polarization and

$$\bar{\mathbf{Y}} = \frac{-1}{\omega\mu\sqrt{k^2 - q^2}} \begin{pmatrix} k^2 & 0 \\ 0 & k^2 - q^2 \end{pmatrix} . \tag{A.79}$$

Applying the typical outgoing wave conditions in the unbounded regions (i.e., $z \to \pm\infty$) and enforcing the boundary conditions at the interface leads to

$$\left(2\bar{\mathbf{Y}} - \bar{\sigma}\right) \cdot \mathbf{E}_{0\|}^{+} = \mathbf{0} , \tag{A.80}$$

for which non-trivial solutions are obtained when

$$\det\left(2\bar{\mathbf{Y}} - \bar{\sigma}\right) = 0 . \tag{A.81}$$

Valid solutions to (A.81) take the form of ω, q pairs which describe the natural, propagating SPP modes supported by the structure.

A.3 Dispersion of edge surface plasmon polariton modes for a 2D plasma

Consider the dielectric interface structure in Fig. 3-2(a). For a charge distribution assumed to be in Region I ($z < 0$), Poisson's equation relates the electrostatic potential to the net charge density as

$$\nabla^2 \begin{Bmatrix} \Phi_1(\mathbf{r}) \\ \Phi_2(\mathbf{r}) \end{Bmatrix} = \begin{Bmatrix} -\rho(\mathbf{r})/\varepsilon_1 \\ 0 \end{Bmatrix} , \tag{A.82}$$

subject to the electrostatic boundary conditions at the interface

$$\Phi_1(\mathbf{r})\big|_{z=0} = \Phi_2(\mathbf{r})\big|_{z=0} , \tag{A.83}$$

$$\varepsilon_1 \frac{\partial}{\partial z}\Phi_1(\mathbf{r})\bigg|_{z=0} = \varepsilon_2 \frac{\partial}{\partial z}\Phi_2(\mathbf{r})\bigg|_{z=0} . \tag{A.84}$$

straightforward to show that

$$G_1^H = A(\mathbf{q})\, e^{qz} \ , \quad G_2^H = B(\mathbf{q})\, e^{-qz} \ , \tag{A.89}$$

where $A(\mathbf{q})$ and $B(\mathbf{q})$ are determined by applying the boundary conditions (A.83)-(A.84) at the interface. For $z' \leq 0$, it follows that

$$G_1\left(\mathbf{q}, z, z'\right) = G_1^p\left(\mathbf{q}, z, z'\right) + A(\mathbf{q})\, e^{qz} \ , \tag{A.90}$$

$$G_2\left(\mathbf{q}, z, z'\right) = B(\mathbf{q})\, e^{-qz} \ , \tag{A.91}$$

where

$$A(\mathbf{q}) = \frac{1}{2\varepsilon_1}\frac{\varepsilon_1 - \varepsilon_2}{\varepsilon_1 + \varepsilon_2}\frac{e^{qz'}}{q} \ , \tag{A.92}$$

$$B(\mathbf{q}) = \frac{1}{\varepsilon_1 + \varepsilon_2}\frac{e^{qz'}}{q} \ . \tag{A.93}$$

In the limit $z' \to 0$, we obtain the Green's function for a source positioned at the interface,

$$G(\mathbf{q}, z, 0) = \frac{1}{2\bar{\varepsilon}}\frac{e^{-q|z|}}{q} \ , \tag{A.94}$$

where $\bar{\varepsilon} \equiv (\varepsilon_1 + \varepsilon_2)/2$. This Green's function accounts for the background structure that will host the graphene.

A.3.1 Charge Density on Semi-Infinite Graphene

In this section, we consider a 2D charge density on graphene localized at $z = 0$. The graphene exists for $x < 0$, invariant with respect to y. The charge density is given by

$$\rho(\mathbf{r}) = \rho_s(x)\, \delta(z)\, e^{ik_y y} \ , \tag{A.95}$$

where $\rho_s(x)$ denotes the surface charge density at the interface. Because the electrostatic potential is also invariant with respect to y, we write $\Phi(\mathbf{r}) = \Phi(x, z)\, e^{ik_y y}$. Application of

(A.86) leads to

$$\Phi\left(x,z\right)=\int_{-\infty}^{\infty}dx'G\left(x,x',z,0\right)\rho_{s}\left(x'\right)\ , \tag{A.96}$$

where

$$G\left(x,x',z,0\right)=\frac{1}{2\bar{\varepsilon}}\int_{-\infty}^{\infty}\frac{dk_{x}}{2\pi}\frac{e^{-q|z|}}{q}e^{ik_{x}(x-x')}=\frac{1}{2\pi\bar{\varepsilon}}K_{0}\left(\left|k_{y}\right|\sqrt{\left(x-x'\right)^{2}+z^{2}}\right)\ , \tag{A.97}$$

with $K_{0}\left(\cdot\right)$ denoting the zero-order modified Bessel function of the second kind. The absolute value $|k_y|$ arises from having $q=\sqrt{k_{x}^{2}+k_{y}^{2}}$.

The continuity equation relates the surface charge density to the surface current at the interface by $i\omega\rho_{s}\left(x\right)=\nabla\cdot\mathbf{J}_{s}\left(x\right)$ where $\mathbf{J}_{s}\left(x\right)=\Theta\left(-x\right)\bar{\sigma}\cdot-\nabla\Phi\left(x,z\right)|_{z=0}$. The components of the current expand to

$$J_{sx}\left(x\right)=-\Theta\left(-x\right)\left[ik_{y}\sigma_{xy}+\sigma_{xx}\frac{d}{dx}\right]\Phi\left(x,0\right)\ , \tag{A.98}$$

$$J_{sy}\left(x\right)=-\Theta\left(-x\right)\left[ik_{y}\sigma_{yy}+\sigma_{yx}\frac{d}{dx}\right]\Phi\left(x,0\right)\ , \tag{A.99}$$

which are used in the continuity equation to obtain $\rho_{s}\left(x\right)\equiv\delta\left(-x\right)\rho_{e}\left(x\right)+\Theta\left(-x\right)\rho_{b}\left(x\right)$, where $\rho_{e}\left(x\right)\equiv\hat{D}_{e}\left(x\right)\Phi\left(x,0\right)$ and $\rho_{b}\left(x\right)\equiv\hat{D}_{b}\left(x\right)\Phi\left(x,0\right)$ such that

$$\hat{D}_{e}\left(x\right)\equiv k_{y}\chi_{xy}+\eta_{xx}\frac{d}{dx}\ , \tag{A.100}$$

$$\hat{D}_{b}\left(x\right)\equiv k_{y}^{2}\eta_{yy}-k_{y}\left(\chi_{xy}+\chi_{yx}\right)\frac{d}{dx}-\eta_{xx}\frac{d^{2}}{dx^{2}}\ , \tag{A.101}$$

where we define $\eta_{\alpha\alpha}\equiv\sigma_{\alpha\alpha}/i\omega$ and $\chi_{\alpha\beta}\equiv\sigma_{\alpha\beta}/\omega$ for $\alpha,\beta\in\{x,y\}$. Substituting ρ_e and ρ_b defined in terms of Eqs. (A.100)-(A.101) into (A.86), we obtain

$$\Phi\left(x,z\right)=\int_{-\infty}^{\infty}G\left(x,x',z,0\right)\rho_{s}\left(x'\right) \tag{A.102}$$

$$=G\left(x,0,z,0\right)\rho_{e}\left(0\right)+\int_{-\infty}^{0}dx'G\left(x,x',z,0\right)\rho_{b}\left(x'\right)\ , \tag{A.103}$$

where $\rho_{e}\left(0\right)$ and $\rho_{b}\left(x\right)$ should be interpreted as the charge density at the edge ($x=0$) and

in the bulk region ($x < 0$), respectively. Setting $z = 0$, we obtain an integro-differential equation for the potential in the plane of the interface,

$$\phi(x) = g(x,0)\,\rho_e(0) + \int_{-\infty}^{0} dx' g\left(x,x'\right)\rho_b\left(x'\right) \ , \tag{A.104}$$

where $\phi(x) \equiv \Phi(x,0)$ and $g(x,x') \equiv G(x,x',0,0)$.

We now expand the potential in terms of Laguerre polynomials,

$$\phi(x) = e^{|k_y|x}\sum_{n=0}^{\infty} c_n L_n\left(-2\,|k_y|\,x\right) \ , \tag{A.105}$$

for which we have the orthogonality condition

$$\int_{-\infty}^{0} e^{2|k_y|x} L_m\left(-2\,|k_y|\,x\right) L_n\left(-2\,|k_y|\,x\right) dx = \frac{\delta_{nm}}{2\,|k_y|} \ . \tag{A.106}$$

Exploiting orthogonality by multiplying both sides sides of (A.104) by $e^{|k_y|x} L_m\left(-2\,|k_y|\,x\right)$ and integrating over x from 0 to ∞ leads to the dispersion relation

$$\frac{c_m}{2\,|k_y|} = \sum_{n=0}^{\infty} c_n A_{mn} \ , \tag{A.107}$$

where

$$A_{mn} \equiv J_{mn} + \eta_{xx}\left(2n+1\right) I_m + \mathrm{sgn}\left(q_y\right)\chi_{xy} I_m \ , \tag{A.108}$$

with

$$I_m \equiv |k_y| \int_{-\infty}^{0} dx e^{|k_y|x} L_m\left(-2\,|k_y|\,x\right) g(x,0) \ , \tag{A.109}$$

$$J_{mn} \equiv \int_{-\infty}^{0}\int_{-\infty}^{0} dx dx' G\left(x,x'\right)\hat{D}_b\left(x'\right) e^{|k_y|(x+x')} L_m\left(-2\,|k_y|\,x\right) L_n\left(-2\,|k_y|\,x'\right) \ . \tag{A.110}$$

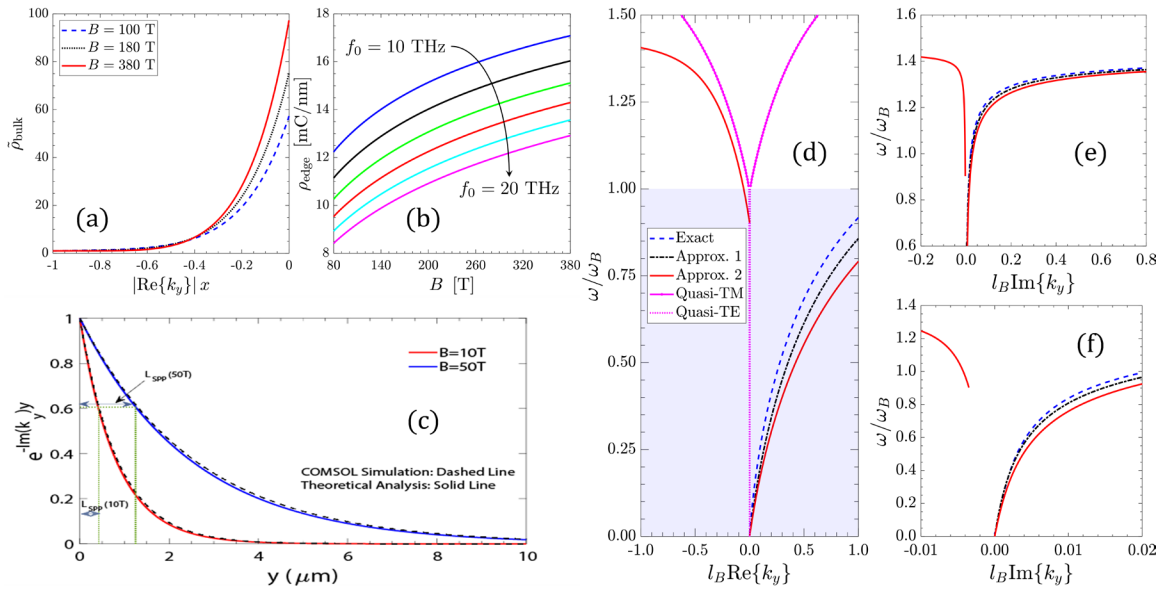

Figure A-3: (a) Bulk and (b) edge charge density for graphene in an external magnetic field. $\tilde{\rho}_{\text{bulk}}$ is the bulk charge density normalized by ρ_{bulk} at $k_x x = -1$, and $\tilde{\rho}_{\text{edge}}$ is the edge charge density normalized by ρ_{edge} at $B = 10\text{T}$ and $\mu = -0.3\text{eV}$. (c) Decay of edge plasmon in comparison with the perturbative solution obtained by introducing loss in Eq. (A.130), and full solution of Maxwell's equations obtained via FEM simulations in COMSOL for graphene in an external magnetic field. The operating frequency is 14THz and $\mu_c = 0.05\text{eV}$. (d)-(f) Real and imaginary parts of the bulk (pink) and edge SPP wave numbers for graphene biased with an external magnetic field. The shaded region in (d) indicates the bulk quasi-TM bandgap, with ω_B denoting the radial frequency corresponding to the first Landau level energy. Approx. 1 is obtained using Eq. (A.128) and Approx. 2 is obtained using Eq. (A.129) for $B = 100\text{T}$ and $\mu = -0.3\text{eV}$, with $l_B = \sqrt{\hbar/eB}$ denoting the magnetic length. In all cases, $T = 40\text{K}$ and $\Gamma = 2 \times 10^{12}\text{s}^{-1}$.

Making the change of variable $y \equiv |k_y|\, x$, reduces (A.109)-(A.110) to

$$I_m = \int_{-\infty}^{0} dy G\left(y, 0\right) e^{y} L_m\left(-2y\right) \ , \tag{A.111}$$

$$J_{mn} = \int_{-\infty}^{0}\int_{-\infty}^{0} dy dy' G\left(y, y'\right) \hat{D}_b\left(y'\right) e^{(y+y')} L_m\left(-2y\right) L_n\left(-2y'\right) \ . \tag{A.112}$$

where

$$G\left(y, y'\right) = \frac{1}{2\pi\bar{\varepsilon}} K_0\left(\left|y - y'\right|\right) \ , \tag{A.113}$$

$$\hat{D}_b\left(y'\right) = \eta_{yy} - \text{sgn}\left(q_y\right)\left(\chi_{xy} + \chi_{yx}\right)\frac{d}{dy} - \eta_{xx}\frac{d^2}{dy^2} \ . \tag{A.114}$$

Note that $\sigma_{xx} = \sigma_{yy}$ and $\sigma_{xy} = -\sigma_{yx}$, which significantly reduces (A.112) to

$$J_{mn} = -\eta_{xx} \int_{-\infty}^{0} \int_{-\infty}^{0} dy dy' G\left(y, y'\right) e^{(y+y')} L_m\left(-2y\right) \frac{d^2}{dy'^2} L_{n+1}\left(-2y'\right) \ , \tag{A.115}$$

which is straight forward to derive obtain using the recursive formulas

$$e^{-y'} \frac{d}{dy'} e^{y'} L_n\left(-2y'\right) = \frac{d}{dy'} L_{n+1}\left(-2y'\right) - L_n\left(-2y'\right) \ , \tag{A.116}$$

$$e^{-y'} \frac{d^2}{dy'^2} e^{y'} L_n\left(-2y'\right) = \frac{d^2}{dy'^2} L_{n+1}\left(-2y'\right) + L_n\left(-2y'\right) \ . \tag{A.117}$$

Truncating the expansion to $N+1$ terms allows us to cast (A.107) as a standard eigenvalue equation

$$\begin{bmatrix} A_{00} & A_{01} & \cdots & A_{0N} \\ A_{10} & A_{11} & \cdots & A_{1N} \\ \vdots & \vdots & \ddots & \vdots \\ A_{N0} & A_{N1} & \cdots & A_{NN} \end{bmatrix} \begin{bmatrix} c_0 \\ c_1 \\ \vdots \\ c_N \end{bmatrix} = \lambda \begin{bmatrix} c_0 \\ c_1 \\ \vdots \\ c_N \end{bmatrix} \ , \tag{A.118}$$

where $\lambda \equiv 1/2\,|k_y|$.

A.3.2 Surface Charge Density

Once the eigenvalue equation is solved for $\{c_n\}$, one can obtain numerical solutions for the potential and the surface charge density. Using the expressions for ρ_e and ρ_b together with Eq. (A.105), it can be shown that

$$\rho_e\left(y\right) = |k_y|\, e^y \sum_{n=0}^{\infty} c_n \left[\left(\mathrm{sgn}\left(k_y\right)\chi_{xy} - \eta_{xx}\right) L_n\left(-2y\right) + \eta_{xx} \frac{d}{dy} L_{n+1}\left(-2y\right)\right] \ , \tag{A.119}$$

$$\begin{aligned} \rho_b\left(y\right) = k_y^2 e^y \sum_{n=0}^{\infty} c_n \{ & \left[\eta_{yy} - \eta_{xx} + \mathrm{sgn}\left(q_y\right)\left(\chi_{xy} + \chi_{yx}\right)\right] L_n\left(-2y\right) \\ & -\mathrm{sgn}\left(q_y\right)\left(\chi_{xy} + \chi_{yx}\right) \frac{d}{dy} L_{n+1}\left(-2y\right) - \eta_{xx} \frac{d^2}{dy^2} L_{n+1}\left(-2y\right) \Big\} \ . \end{aligned} \tag{A.120}$$

Then, using $L_n(0) = 1$ and $L'_n(0) = -n$, we obtain

$$\rho_e(0) \equiv |k_y| \sum_{n=0}^{\infty} c_n \left[\mathrm{sgn}(k_y) \chi_{xy} + (2n+1) \eta_{xx} \right] \ . \tag{A.121}$$

Assuming $\sigma_{xx} = \sigma_{yy}$ and $\sigma_{xy} = -\sigma_{yx}$,

$$\rho_b(y) = -\eta_{xx} k_y^2 e^y \sum_{n=0}^{\infty} c_n \frac{d^2}{dy^2} L_{n+1}(-2y) \ . \tag{A.122}$$

Figures A-3(a),(b) shows bulk and edge charge density at several values of external magnetic bias.

A.3.3 Approximating the Dispersion Relation

To a good approximation, the edge dispersion within the first TM band gap is obtained by considering only the $n = 0$ term in the expansion (A.105). With the assumption that $\sigma_{xx} = \sigma_{yy}$ and $\sigma_{xy} = -\sigma_{yx}$, we find $J_{00} = 0$, leading to

$$|k_y| = \left[2 I_0 \left(\eta_{xx} \pm \chi_{xy} \right) \right]^{-1} \ , \tag{A.123}$$

where

$$I_0 = |k_y| \int_{-\infty}^{0} dx e^{|k_y| x} g(x, 0) \ , \tag{A.124}$$

such that

$$g(x, 0) = \frac{1}{2\bar{\varepsilon}} \int_{-\infty}^{\infty} \frac{dk_x}{2\pi} \frac{1}{q} e^{i k_x x} \ , \tag{A.125}$$

which we approximate by expanding $q = \sqrt{k_x^2 + k_y^2}$ about $k_x = 0$,

$$\sqrt{k_x^2 + k_y^2} \simeq |k_y| + \frac{k_x^2}{2|k_y|} \ . \tag{A.126}$$

This leads to the closed form approximate solution of (A.125)

$$g(x, 0) \simeq g_0(x, 0) \equiv \frac{1}{2\bar{\varepsilon}\sqrt{2}} e^{-\sqrt{2}|k_y||x|} \ , \tag{A.127}$$

which we use in (A.130), simplifying the dispersion relation to

$$|k_y| = \bar{\varepsilon}\frac{1+\sqrt{2}}{\eta_{xx} \pm \chi_{xy}} \ . \tag{A.128}$$

We find this result better approximates the exact edge mode dispersion than that used in previous works [163], [164],

$$|k_y| = \bar{\varepsilon}\frac{3\eta_{xx} - \mathrm{sgn}\,(k_y)\,2\sqrt{2}\chi_{xy}}{\eta_{xx}^2 - \chi_{xy}^2} \ . \tag{A.129}$$

A.3.4 Material Loss

In statics, there is no concept of loss. However, our interest is in the quasi-static regime, such that we can perturb the system slightly by introducing a non-zero scattering rate Γ in the conductivity. Then, we can make the replacement

$$|k_y| \to k_y = \begin{cases} +\mathrm{Re}\,(k_y) + i\mathrm{Im}\,(k_y) & \mathrm{Re}\,(k_y)\,, \mathrm{Im}\,(k_y) > 0 \\ -\mathrm{Re}\,(k_y) - i\mathrm{Im}\,(k_y) & \mathrm{Re}\,(k_y)\,, \mathrm{Im}\,(k_y) < 0 \end{cases} \tag{A.130}$$

which ensures that the wave decays in the case of both forward and backward propagation. This results in complex-valued wavenumbers for the edge dispersion from both the exact method (A.118) and from the approximate value (A.128). As a check, we compared decay rates of the edge SPP generated using this perturbative approach and the result found via COMSOL. Figure A-3(c) shows good agreement between the two methods for graphene in an external magnetic field.

Figure A-3(d) shows the bulk and edge dispersion for graphene in an external magnetic bias field. The edge modes are computed using the exact quasi-static analysis, Eq. (A.118), and a comparison between the exact and approximate edge dispersion solutions is also shown in A-3(e),(f). Although the results were computed assuming $B = 100$ T, due to the normalization the dispersion diagrams are essentially independent of B for $|B| > 1$ T.